Universidade de Évora - Escola de Ciências e Tecnologia

Mestrado em Engenharia da Energia Solar

Dissertação

Modeling and performance analysis of a solar HVAC system with an absorption chiller

Maria de Oliveira Fernandes

Orientador(es) | Paulo Canhoto

Évora 2026

Universidade de Évora - Escola de Ciências e Tecnologia

Mestrado em Engenharia da Energia Solar

Dissertação

Modeling and performance analysis of a solar HVAC system with an absorption chiller

Maria de Oliveira Fernandes

Orientador(es) | Paulo Canhoto

Évora 2026

A dissertação foi objeto de apreciação e discussão pública pelo seguinte júri nomeado pelo Diretor da Escola de Ciências e Tecnologia:

Presidente	|	Frederico José Grilo (Universidade de Évora)
Vogais	|	Judit García-Ferrero (Universidade de Salamanca) Paulo Canhoto (Universidade de Évora) (Orientador)

Évora 2026

Abstract

In the present work, the model of a domestic solar heating and cooling system was developed and studied for a typical meteorological year in Évora, Portugal. The proposed system is composed of evacuated tubes solar collectors, an absorption heat pump and two thermal storage systems at different temperature levels. A base case was studied for periods of high cooling and heating demands and a parametric analysis was then conducted in order to optimise the system design. An annual solar fraction of 0.72 was obtained, which corresponds to a system with 5 solar collectors, a heat pump able to deliver 1.86 kW of cooling power, 300 kg of high temperature storage and 200 kg of low temperature storage. The system shows promise for the summer period but struggled to cover heating demand during the winter, indicating that solar cooling is far more relevant than solar heating.

Modelação e análise do desempenho de um sistema de climatização solar com bomba de calor por absorção

Resumo

No presente trabalho foi desenvolvido um modelo de um sistema doméstico de climatização solar, e estudado o seu desempenho durante um ano meteorológico típico correspondente a Évora, Portugal. O sistema é composto por coletores de tubo de vácuo, uma bomba de calor por absorção e dois sistemas de armazenamento de energia térmica a níveis de temperatura diferentes. Foi estudado um caso base para períodos com elevadas necessidades de arrefecimento e aquecimento e realizada uma análise paramétrica para otimizar o sistema. Obteve-se uma fração solar anual de 0.72 para um sistema composto por 5 coletores, uma bomba de calor com capacidade de 1.86 kW de arrefecimento, 300 kg de armazenamento térmico a alta temperatura e 200 kg a baixa temperatura. O sistema apresenta resultados promissores para o verão, mas não supriu a necessidade de aquecimento durante o inverno, indicando uma elevada relevância do arrefecimento solar face ao aquecimento solar.

Contents

List of Figures

List of Tables

Nomenclature

A	Area (m^2)
AST	Apparent solar time (min)
AU, UA	Thermal conductance (coefficient (W K^{-1})
c	Specific heat capacity at constant pressure (J kg^{-1} K^{-1})
CDD	Cooling degree-days (K)
COP	Coefficient of performance of the heat pump (-)
D	Diameter (m)
e	Effectiveness (-)
F_R	Heat removal factor (-)
G_0	Extraterrestrial irradiance on a horizontal plane (W m^{-2})
G_{sc}	Solar constant = 1366 (W m^{-2})
Gr	Grashof number (-)
g	Gravitational acceleration (m s^{-2})
H	Height (m)
HDD	Heating degree-days (K)
h	Hour angle (°) or heat transfer coefficient (W m^{-2} K^{-1}) or specific enthalpy (J kg^{-1})
h_{fg}	Latent heat of phase transition (J kg^{-1})
I	Irradiance (W m^{-2})
k	Thermal conductivity (W m^{-1} K^{-1})
k_i	Clearness index (-)
k_θ	Incidence angle modifier (-)
L	Length (m) or latitude (°)
$\mathcal{L}$	Characteristic length (m)
LC	Longitude correction (min)
LL	Local longitude (°)
LST	Local standard time (min)
M	Mass (kg)

$\dot{m}$	Mass flow rate (kg/s)
Nu	Nusselt number (-)
Pr	Prandtl number (-)
P	Pressure (Pa)
Q	Heat transfer (Wh)
$\dot{Q}$	Heat transfer rate (W)
R	Thermal resistance (K W^{-1})
Ra	Rayleigh number (-)
Re	Reynolds number (-)
Ri	Richardson number (-)
r	Radius (m)
S	Absorbed irradiance (W m^{-2})
T	Temperature (K)
V	Volume (m^3)
v	Velocity (m s^{-1})
$\dot{W}$	Power (W)
Z_{sc}	Solar collector azimuth (°)

Greek symbols

α	Absorptivity (-)
β	Coefficient of thermal expansion (K^{-1})
β_{sc}	Tilt angle (°)
Δx	Thickness (m)
ΔT	Temperature difference (K)
Δt	Time period (h)
δ	Solar declination (°)
ε	Emissivity (-)
η	Efficiency of the solar collectors (-)

θ Incidence angle (°)

μ Dynamic viscosity (Pa s)

ρ Surface albedo (-) or density (kg m^{-3})

σ Stefan-Boltzmann constant = 5.67×10^{-8}(W m^{-2} K^{-4})

τ Transmissivity (-)

$(\tau\alpha)$ Optical efficiency of the solar collector (-)

ν Kinematic viscosity (m^2 s^{-1})

ϕ Solar zenith (°)

Subscripts

a Ambient

abs Absorber

ap Aperture

b Boiling

BN Beam/direct irradiance on a plane always normal to sun rays

C Convection

$Cond$ Conduction

c Cold or condensation or condenser

$cool$ Cooling

DH Diffuse irradiance on the horizontal plane

DHW, dhw Domestic hot water

e Evaporator

f Fluid or fin

g Glass or generator

GH Global irradiance on the horizontal plane

h Hot

he Heat exchanger

hp Heat pipe or heat pump

hts, ht High temperature storage

i Inner or inlet

L Loss

l Liquid

lts, lt Low temperature storage

m Manifold

o Outer or outlet

p Circulation pump

SC, sc Solar collectors

t Tank

U Useful

v Vapor

Acronyms

CDD Cooling degree-days

COP Coefficient of performance of the heat pump

DHW Domestic hot water

ETC Evacuated tubes collector

$EFPC$ Evacuated flat plate collector

FPC Flat plate collector

HDD Heating degree-days

HTS High temperature storage

$HVAC$ Heating, ventilation, and air conditioning

IEA International Energy Agency

LCA Life-cycle assessment

$LCCA$ Life-cycle cost analysis

$LCOC$ Levelized cost of cooling

LHS Latent heat storage

LTS Low temperature storage

NTU Number of transfer units

PCM Phase change materials

PTC Parabolic trough collector

SHC Solar heating and cooling

$SPACS$ Solar powered absorption cooling system

TES Thermal energy storage

1. Introduction

1.1. Current energy status

In recent years, renewable energy power plants have experienced record-breaking growth. This comes as an attempt to attenuate the climate crisis, as temperatures keep rising and events like wildfires, flooding and droughts become more frequent and intense around the world (REN21, 2025).

Additionally, the rise of geopolitical tensions and trade disruptions has led to countries seeking to improve their energetic autonomy, by which renewable sources may represent not only an aid to the climate crisis, but also a means to ensure economic and national security (REN21, 2025) (IEA, 2025).

Solar photovoltaic has led the renewable growth, given its mature technology and supply chains, and ever decreasing costs and scalability, while the use of battery storage has accompanied this trend, in order to maintain grid stability (REN21, 2025).

Figure 1 illustrates the recorded and expected evolution of various energy sources between 2019 and 2030:

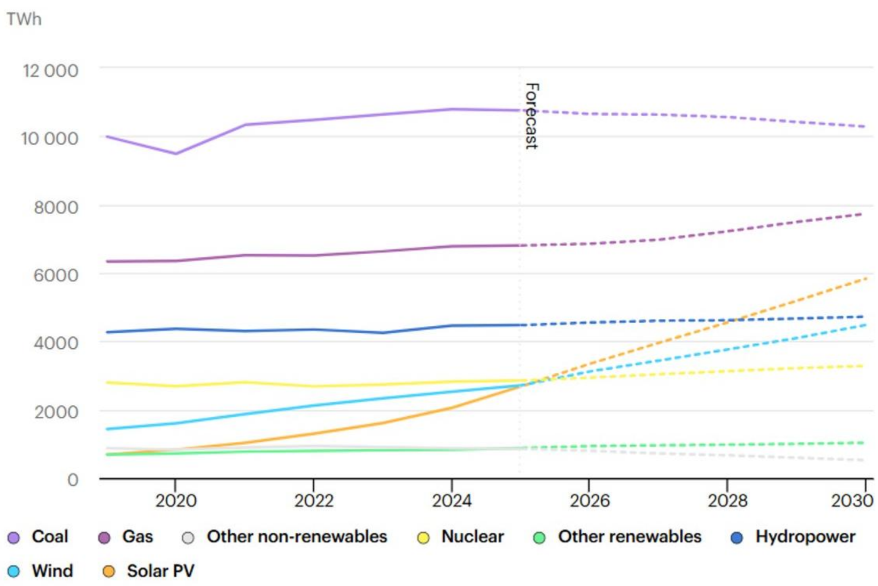

Figure 1: Global electricity generation by source (IEA, 2026).

In the case of Portugal, in 2025 renewable sources delivered about 71% of consumed electricity, with hydropower and wind each producing approximately 28%, solar 9% and biomass 6% (REN, s.d.). For this reason, Portugal is considered a “pioneer in Europe’s energy transition”. Recent growth is mostly due to a rapid implementation of large-scale and rooftop photovoltaic installations (Pires, 2025).

However, electricity only accounts for approximately 20% of the total final energy consumption, with 50% corresponding to heating and cooling, and 30% to transportation (IRENA, s.d.). The share of renewable energy sources in each sector in 2022 (latest available data) can be seen in Figure 2:

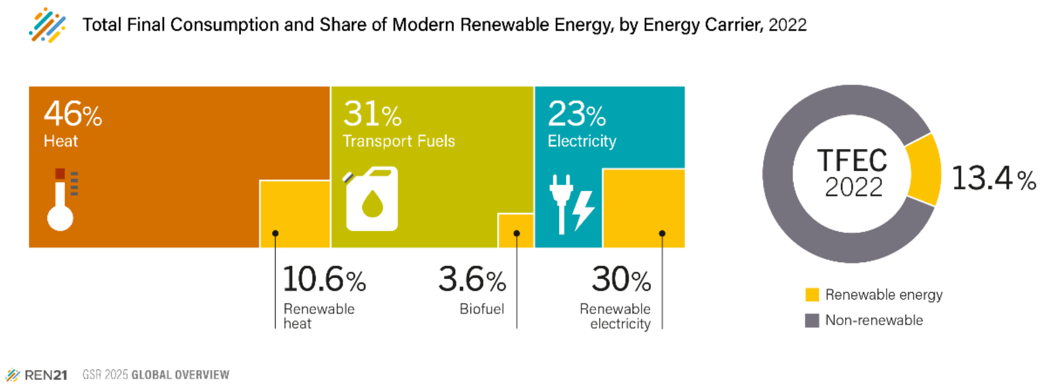

Figure 2: Total final consumption and share of renewable energy (REN21, 2025)

From Figure 2 we may conclude that the implementation of renewables is significantly more advanced in electricity than heat or transportation, resulting in an average renewable share of only 8% in these two sectors combined.

Energy demand is also increasing as a result of higher cooling needs, technological innovations and industrial expansion, as data centres and artificial intelligence (AI) applications multiply (REN21, 2025) (IEA, 2026). Cooling and air conditioning currently correspond to 20% of the consumed electric energy worldwide (Ramlee, et al., 2026). Cooling demand in particular is expected to increase significantly by 2050, due to the rise of temperatures (UNEP, 2025), while in the United Arab Emirates, where ambient temperatures reach above 50 °C, cooling already accounts for 70% of the consumed electricity (Rayes & Ghaith, 2025). Such systems are thus now referred to as an essential infrastructure such as water and energy, as heat waves become a dangerous problem (UNEP, 2025).

The currently faced challenges result in a current attempt to “electrify everything”, which is seen as a means to obtain affordable and clean energy. All this culminates in a rise of electricity demand in advanced economies, after a 15 year period of stagnation. Globally, electricity demand is expected to outpace economic growth through 2030 (IEA, 2026).

Therefore, despite the growth in renewable energy capacity, a 100% renewable scenario is still at least decades away (Foss, 2022). This, in addition to the large percentage of energy demand that corresponds to thermal energy, highlights the importance of heat as an energy source. Heat (and renewable heat, in particular) has not been given its due visibility and political support, and its growth is modest and insufficient to cover the rising demand (REN21, 2025).

In fact, in recent years new solar thermal installations and global installed capacity have been declining. Mexico was within the few countries to oppose this trend, reporting a 14% increase in installed capacity as a way to achieve improved energy security, as well as lower energy costs for industrial processes (REN21, 2025). Solar thermal energy has additional advantages, since these technologies mostly require basic raw materials, leading to the possibility of local manufacturing and economic development in a great variety of places (IEA, 2012).

In addition to the difficulty associated with obtaining enough energy for the production of electricity, impacts related to the electrification process are starting to be reported, such as issues related to grid stability. The high penetration of variable renewable energy sources (vRES) such as solar photovoltaic and wind in the electric grid leads to stability issues given the intermittency of such types of energy production, leading to the possibility of system collapse under significant disturbances. A battery storage system is shown to attenuate these variabilities and improve the system stability (Paiva & Castro, 2024).

However, the currently used lithium-ion batteries pose problems related to the material usage throughout their life cycles, namely the availability of lithium and cobalt, the latter being mostly sourced from the politically unstable Democratic Republic of the Congo. Improving the sustainability of such technologies will require expanding the geographic availability of the raw material sources and developing recycling methods for said materials, while ensuring a higher energy and / or a longer lifetime (Babbitt, 2020).

These limitations suggest that a general electrification is yet unsustainable, which reinforces the relevance of systems that can use thermal energy directly.

1.2. Heating and cooling systems

Technologies designed for the heating or cooling of indoor spaces are typically referred to as HVAC (heating, ventilation, and air conditioning), and assist with maintaining adequate humidity levels and air quality as well as comfortable temperatures. These include central heating systems used during the ancient Rome period for homes and public baths, and coal-fired boilers and large fans used in factories during the industrial revolution. The first modern air conditioning unit was invented in 1902 by Willis Carrier and was originally intended as a space dehumidifier, but happened to also cool the air while it operated (Mckoy, Tesiero, Acquaah, & Gokaraju, 2023).

The present work focuses on the absorption cooling method. Note that since absorption heat pumps are supplied by thermal energy, they are here assumed to be components of heating and cooling systems, despite the fact that they do not deliver heating by themselves.

Absorption heat pumps (or chillers) were introduced in 1858 by Ferdinand Carré (Rayes & Ghaith, 2025). They work in a similar manner to vapor compression units, which are composed of a compressor, a condenser, an expansion valve and an evaporator. In these systems, a refrigerant fluid in saturated vapor state enters a mechanical compressor, where the work done by it increases the pressure of the refrigerant, allowing it to transition into saturated liquid once it reaches the condenser. Next the fluid passes through an expansion valve, reducing its pressure, allowing it to transition back into vapor at the evaporator, at a lower temperature than that of the condenser. The fluid then returns to the compressor. The phase transition in the evaporator removes thermal energy from the cooled or refrigerated space, while the one in the condenser releases thermal energy (Moran, Shapiro, Boettner, & Bailey, 2018). A representation of such systems can be seen in Figure 3:

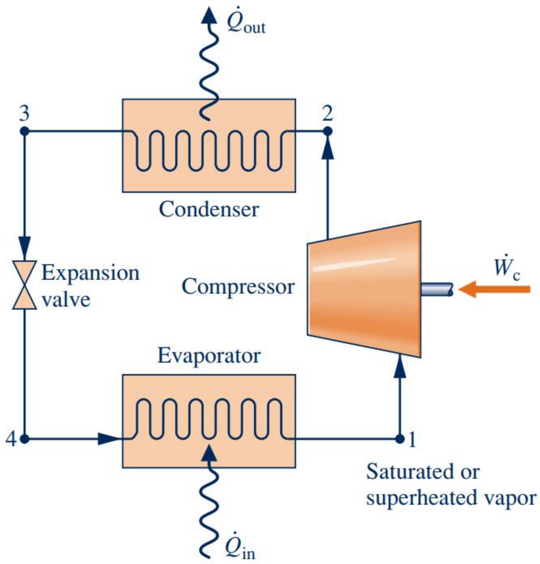

Figure 3: Components of a vapor compression refrigeration system (Moran, Shapiro, Boettner, & Bailey, 2018).

The difference between a conventional system and an absorption one lies in the nature of the compressor. In an absorption system, the compressor is thermochemical, and made of four components: an absorber, a generator, a circulation pump and a valve. In this case, the refrigerant fluid leaving the evaporator enters the absorber, where it is absorbed by another substance – the absorbent – forming a strong aqueous mixture. This mixture is then pumped to a higher pressure. Indeed, the pump does require a small amount of electricity to operate, however, this value is often neglected, since the required work is much smaller than what would be necessary to compress a vapor, because of Eq. (1), which relates the work required to operate a pump to the specific volume of the substance (Moran, Shapiro, Boettner, & Bailey, 2018):

$$\left(\frac{\dot{W}_p}{\dot{m}}\right) = -\int_1^2 v\, dp \tag{1}$$

The mixture then arrives to the generator, where the refrigerant vapor separates from the mixture in response to a heat input. The refrigerant vapor proceeds to the condenser, while the weak mixture resulting from the process travels through a valve back to the absorber (Moran, Shapiro, Boettner, & Bailey, 2018). This type of system is represented in Figure 4:

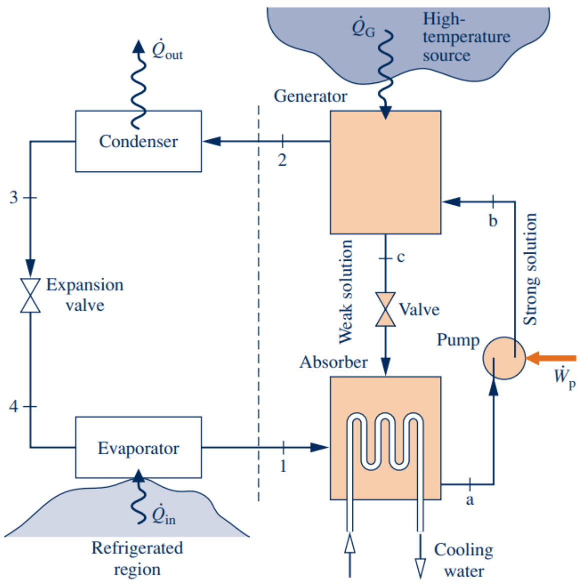

Figure 4: Components of an absorption heat pump (Moran, Shapiro, Boettner, & Bailey, 2018).

In an absorption chiller, heat is absorbed in the evaporator from the cooled / refrigerated zone, and in the generator from the heat supply, while heat is released in the condenser and in the absorber. The released heat might be used for low temperature heating applications. Note that the absorber's capacity to absorb the refrigerant vapor decreases with an increase in temperature (Moran, Shapiro, Boettner, & Bailey, 2018).

An important advantage of such systems is the flexibility of heat sources that may be used to supply the generator: it can either come from a renewable source like solar thermal, geothermal or biomass, but also with waste heat originated from industrial processes.

In addition to the main components listed above, a heat exchanger is usually added to the system, between the generator and the absorber, in such a way that the weak mixture coming out of the generator preheats the strong mixture that is entering it, hereby improving the efficiency of the process (Moran, Shapiro, Boettner, & Bailey, 2018).

Several different fluid pairs can be used in absorption cooling systems. The two most common are lithium bromide and water (Li-Br/H2O), where water serves as the refrigerant and lithium bromide as the absorbent, and water and ammonia (NH3/H2O), where ammonia is the refrigerant, and water the absorbent. Systems that use lithium bromide and water are limited by water's freezing temperature, so these are not adequate for food refrigeration applications. In water and ammonia systems, on the other hand, since ammonia is the refrigerant, negative temperatures can be reached in the evaporator, and the system can be used for food refrigeration. However, a rectifier must be placed between the generator and the condenser to stop any water from entering the refrigerant circuit, as it can lead to ice formation (Moran, Shapiro, Boettner, & Bailey, 2018). The resultant modified system can be seen in Figure 5:

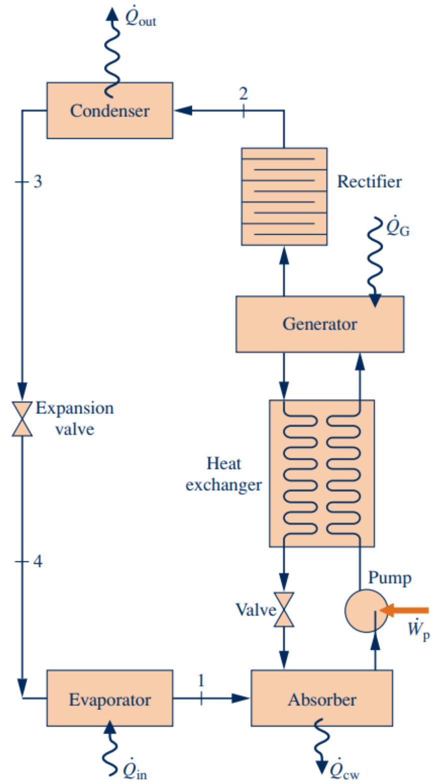

Figure 5: Modified ammonia-water absorption system (Moran, Shapiro, Boettner, & Bailey, 2018).

The water and ammonia mixture has the main disadvantage of ammonia being toxic and flammable (Leonzio, 2017).

The performance of an absorption heat pump is measured through the coefficient of performance (COP), which is defined as the ratio between the heat transferred in the evaporator (cooling load) and the energy required to operate the system (Moran, Shapiro, Boettner, & Bailey, 2018).

Absorption chillers may be categorized into half, single or multiple-effect (double or triple) as a function of their configuration and temperature input requirement (Leonzio, 2017). The previously described system corresponds to a single-effect absorption heat pump, where typical COP values reached are between 0.6 and 0.8, with heat source temperatures between 70 °C and 95 °C (Rayes & Ghaith, 2025).

In a half-effect system, only a fraction of the refrigerant vapor that exits the generator will travel through the refrigeration circuit, while the remainder returns to the absorber. These systems require a lower generator temperature but also achieve significantly lower COP values (Leonzio, 2017).

Multiple-effect systems on the other hand use 2 or 3 generators and heat sources at higher temperatures, enabling much higher coefficient of performance values. If supplied through thermal solar collectors, technologies such as parabolic trough collectors must be used to reach the required temperatures (Leonzio, 2017). The highest COP values are achieved in triple-effect systems, since they use 3 generators at successively decreasing temperatures. They have high initial investments and operating expenses as a result of the high temperature requirement (around 200 °C) (Rayes & Ghaith, 2025).

1.3. Solar heating and cooling

Solar heating and cooling (SHC) technologies are particularly interesting solutions to the currently faced challenges, given their low operation costs, as well as flexibility in terms of applications and back-up heat sources. Coupling solar energy with cooling technology in particular enables a high coincidence between availability of resource and demand. Solar thermal cooling has thus the ability to reduce the load on the electric grid (IEA, 2012).

Solar cooling systems can be electrically or thermally driven. Electrically driven cooling systems combine photovoltaic panels with conventional vapor compression units. If not connected to the grid, the system should include battery storage to be able to meet demands during low solar availability periods. Photovoltaic panels as well as the storage must be carefully dimensioned in order to ensure a reliable and efficient performance (Ramlee, et al., 2026).

Solar thermally driven cooling systems use thermal solar collectors and thermally driven chillers, such as absorption or adsorption chillers. Most systems include thermal storage and auxiliary systems (Ramlee, et al., 2026).

Figure 6 includes the main solar cooling systems and how they may be categorized:

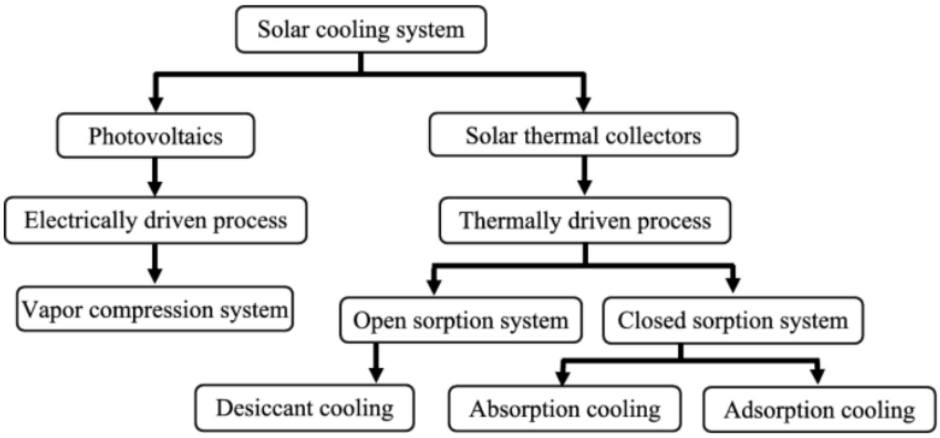

Figure 6: Classification of most common solar cooling systems (Ramlee, et al., 2026).

Among the thermally driven solar cooling systems, absorption can reach the highest COP values and is therefore the most viable technology so far, especially for large-scale projects. Adsorption systems have the advantage of requiring lower heat source temperatures, however their operation is more intermittent, and the performance is less efficient. Both adsorption and desiccant systems can reach COP values between 0.5 and 0.6, while absorption systems are able of reaching between 0.8-1.5 (Ramlee, et al., 2026).

Solar-powered absorption cooling systems (SPACS) in particular go back to 1962 (Rayes & Ghaith, 2025), and consist of absorption heat pump units supplied by solar thermal collectors. The most common solar collector technologies include flat plat collectors (FPC), evacuated tube collectors (ETC), and parabolic trough collectors (PTC) (Ramlee, et al., 2026). The entire system can be evaluated through the solar fraction, which is defined as the ratio between the solar sourced energy supplied by the system and the total required energy.

The intermittent nature of the solar resource makes it so thermal energy storage and auxiliary systems are required, which ensure the stability of a SPACS during low radiation periods and peak load conditions. A thermal energy storage system can attenuate the variation of the solar resource availability, hereby improving the continuity of the operation of solar cooling systems and increasing the overall efficiency (Rayes & Ghaith, 2025).

SPACS are already considered competitive in medium or large scaled applications, given their energetic efficiency and low environmental impacts (Leonzio, 2017). However, the large-scale deployment of solar cooling systems relies on whether researchers can solve a series of challenges related to technical and economic factors, such as improving their efficiency under variable environmental conditions. Their complexity and high initial costs result in low competitiveness when compared to conventional vapor compression systems (Rayes & Ghaith, 2025).

1.4. Objectives

The goal of this work is to develop a model of a solar climatization system composed of an evacuated tubes collector, an absorption heat pump, and thermal energy storage. The impact of some of the main design choices will be studied through a parametric analysis and an optimized version of the system will be proposed. The performance of the model will be evaluated using a typical meteorological year for the region of Évora, Portugal. The annual solar fraction will be calculated, which will allow to draw conclusions about the viability of the proposed system.

1.5. Outline

The current work is organised as follows: in Section 2 a state of the art of solar-powered absorption cooling systems is presented. Section 3 illustrates the proposed model and includes numerical implementation and model validation subsections, with a special focus given to the evacuated tubes model. In Section 4 the case study conditions will be presented, such as the location and environmental data source, the demand calculations, the dimensions of the system and the parametric analysis conditions. Section 5 includes the results of the study, focusing on the heat pump's operation, the detailed analysis of the base case scenario and the parametric analysis and annual solar fraction results. The respective discussion is in Section 6 and the conclusions can be seen in Section 7.

2. State of the art of SPACS

A growing amount of researchers have dedicated to the study and optimization of solar powered absorption cooling systems (SPACS), given the complexity that arises from trying to balance thermal performance, financial cost and operational stability of such systems (Rayes & Ghaith, 2025). The optimization includes increasing the coefficient of performance while decreasing the levelized cost of cooling (LCOC) and the auxiliary energy use, and can be achieved through data-driven models, deterministic methods and metaheuristic algorithms (Rayes & Ghaith, 2025). Despite the growing interest, the research into residential scale systems and experimental studies are limited (Altiokka & Arslan, 2023).

Solar absorption systems show the most promise within regions that combine a high solar resource availability (at least 1900 $kWh/m^2/year$) with expensive electricity prices and proper government incentives (Rayes & Ghaith, 2025).

2.1. System configuration

As stated previously, solar-powered absorption cooling systems include solar collectors, thermal energy storage and auxiliary systems, all of which discussed in greater detail in the following subsections.

2.1.1. Solar collectors

In the context of SPACS, the three most studied types are flat plate, evacuated tubes and compound parabolic (Rayes & Ghaith, 2025).

Flat plate collectors can deliver temperatures between 30 °C and 80 °C and have advantages related to their simplicity and affordability, but experience severe heat losses when operating at high temperatures (Rayes & Ghaith, 2025).

Evacuated tube collectors can reach temperatures between 50 °C and 150 °C with minimized thermal losses given the vacuum layer between their double-glass structure. Their heat transfer ability is improved through the use of heat pipes and selective inner coatings, making them more viable in cold environmental conditions. Their main disadvantage is the high cost and delicate nature of the glass tube (Rayes & Ghaith, 2025).

Parabolic trough collectors (PTC) consist of parabolic mirrors that concentrate solar radiation onto a receiver tube, reaching temperatures between 150 °C and 400 °C, making them adequate for multiple-effect absorption systems. Concentrating solar technology, however, requires precise alignment of the tracking system, leading to high initial and maintenance costs (Rayes & Ghaith, 2025).

Evacuated flat plate collectors (EFPC) should also be noted, which consist on FPCs with a vacuum insulation, reaching temperatures between 80 °C and 150 °C with cost additions between 25 and 30% when compared to a conventional FPC (Rayes & Ghaith, 2025).

The use of hybrid photovoltaic-solar thermal systems or collectors is interesting given the ability to provide both electrical energy for the circulation pumps, control units and auxiliary electric heaters, and thermal energy for the heat pump and any heating demands. Hybrid collectors are particularly pertinent in urban places, enabling electric and thermal energy production in a relatively small area (Rayes & Ghaith, 2025).

For solar powered absorption cooling, evacuated tubes collector is often considered the best choice for SPACS, given it represents a compromise between improved heat pump performance and financial investment (Altiokka & Arslan, 2023) (Rayes & Ghaith, 2025). While flat plate collectors achieved better economic viability, evacuated tube and compound parabolic collectors led to better COP values, especially for countries in Europe with limited solar availability. Parabolic through collectors have shown to have increased thermal losses due to the increased length of their pipeline (Rayes & Ghaith, 2025).

2.1.2. Absorption heat pumps

Material innovations and optimized heat exchanger designs have led to improved thermal efficiency in each component of the heat pump. Examples are using microchannel, twisted tube or corrugated plate exchangers instead of the traditional shell-and-tube, showing an improvement of 20% in the thermal efficiency of the generator. Meanwhile, in the absorber and condenser, the use of nano-coatings and corrosion-resistant materials has showed to enhance heat rejection (Rayes & Ghaith, 2025).

The use of nanofluids as the thermal transfer media between the thermal storage and the absorption heat pump increases the heat transfer of the system and allows it to reach higher temperatures and efficiencies, although researchers are still trying to solve problems related to the materials' durability and compatibility, and overall cost optimization. Nanoparticles such as aluminium oxide (Al_2O_3) or titanium dioxide (TiO_2) provide a high thermal conductivity and corrosion resistance, while water as a base fluid provides affordability. Titanium dioxide nanofluids have the added benefit of enabling higher heat transfers with small values of flow rates, hence decreasing the required pumping power. Although the use of nanofluids shows promise, their environmental effects are not yet well understood (Rayes & Ghaith, 2025).

Recently, absorption systems coupled with desalination technologies are able to deliver both cooling and drinking water, although at high initial investments (Rayes & Ghaith, 2025).

2.1.3. Thermal storage systems

An adequate thermal energy storage system is shown to be essential in reducing the impact of the solar resource intermittency, and both the configuration and the material selection affect the responsiveness and efficiency of the system. Studies show that tanks with a capacity greater than 1000 litters experience increased thermal losses and therefore produce diminishing results.

Innovations in TES include the use of aerogels as advanced insulation materials and phase change materials (PCMs) for latent heat storage. PCMs can reach volumetric storage density values between five to fourteen times that of water, with studies indicating that they might enable 10 hours of operation at 90 °C. Examples of promising PCMs are nanocomposite materials with Al_2O_3 or CuO, which exhibit high heat transfer rates but suffer from nanoparticle agglomeration and high production costs (Rayes & Ghaith, 2025).

2.1.4. Auxiliary heating systems

As auxiliary heating systems, heat pumps show great promise, since they provide operational resilience and lead to higher efficiencies with significantly less grid power usage and / or carbon emissions than their alternatives. Their main disadvantage is the high initial investment. Water-to-water heat pumps are preferable to air-to-water systems since they can use stable ground or water temperatures, which enables an improved performance, but at an increased cost (Rayes & Ghaith, 2025).

Auxiliary systems such as gas-fired boilers produce high enough temperatures for double-effect absorption cycles (Rayes & Ghaith, 2025).

Vapor-compression units powered by photovoltaic electricity in hybrid systems may serve as auxiliary systems, resulting in configurations with extended operation during peak load and that enable decarbonised off-grid applications, serving as a framework for net-zero-energy (Rayes & Ghaith, 2025).

It is of great importance to apply strategies that minimize the usage of auxiliary energy, which include the implementation of adequate system configuration and control, collector and storage sizing, and adjustment of the evaporator temperature. The control of the TES charging alone can reduce auxiliary energy usage to half. Variable-effect chillers can switch between single and double-effect modes, hereby minimizing auxiliary power consumption (Rayes & Ghaith, 2025).

2.2. Modelling studies

The development of solar powered absorption cooling systems (SPACS) relies heavily on simulation modelling, as this enables an assessment of a given project's efficiency and viability before high investments. Reliable annual simulations are essential given the systems' complex nature and requirement for large amounts of data. Annual simulations can be done with models built in software such as MATLAB/Simulink and TRNSYS which enable predictions of COP and solar fraction values as a function of solar availability and cooling demand fluctuations. The most common is TRNSYS given its modular design, although MATLAB/Simulink excels at dynamic modelling and control system development (Rayes & Ghaith, 2025).

Control algorithms like Model Predictive Control (MPC) can be implemented as a means to decrease auxiliary energy consumption without decreasing thermal comfort, with one study reporting a 60% decrease in gas consumption on cloudy days. However, challenges arise with the use of such systems, given the requirement for high computational expenses and precise weather information (Rayes & Ghaith, 2025).

2.3. Experimental studies

A gap currently exists between simulations and real-life systems that comes as a result of several challenges often underestimated or neglected by models, such as high costs, poor system control, thermal losses in the generator, poor heat rejection, scaling, fouling and crystallization. Long-term experimental studies are yet required to understand the full extent of these phenomena. That being said, a five-year test was already conducted by the Fraunhofer Institute, on a 35.2 kW LiBr-H_2O absorption system, reaching a COP of 0.81 and a solar fraction of 60% (Rayes & Ghaith, 2025).

One of the main challenges of real-life systems involves the heat rejection system, which removes heat from the condenser and absorber, requiring access to a heat sink (air, ground or water) to do so. This system's performance is critical to obtain a steady and efficient operation, since an increase in the condenser temperature signifies that a higher pressure is needed in this component, thus increasing the condenser/absorber pressure ratio and lowering the COP. A higher condenser temperature can decrease the COP by more than 30%. This highlights the need for efficient cooling systems and climate-based condenser management (Rayes & Ghaith, 2025).

The addition of cooling towers is recommended. Wet cooling towers have better thermal efficiency than dry cooling methods but require a continuous water supply and may result in scaling, drift problems or legionella outbreaks, and thus have a greater need for maintenance (Rayes & Ghaith, 2025).

Hot-arid regions that experience ambient temperatures above 45 °C suffer significantly from decreased absorption heat pump performance because of the increased condenser temperature, while simultaneously having a lower water availability to supply cooling towers. For such places, dry-cooling towers must be implemented, as well as dust-resistant collector optics (Rayes & Ghaith, 2025).

On the other hand, the high humidity in tropical regions leads to decreased cooling tower performance due to the formation of condensation on heat exchanger surfaces, while the regular presence of clouds diminishes the output of the solar system as well as the reliability of model predictions. In these cases, systems benefit from the addition of desiccant units for dehumidification purposes, and should have increased heat rejection capacity because of high wet-bulb temperatures (Rayes & Ghaith, 2025).

Hybrid cooling systems have the ability to switch between both dry and wet cooling methods in function of the climate, achieving high energy efficiency with significantly less water usage, but at the cost of a higher investment (an increase of around 30%) (Rayes & Ghaith, 2025).

Another critical factor in the efficiency of real-life SPACS is the thermal energy loss in piping networks, storage tanks and heat exchangers. This is particularly significant in parabolic trough collectors, which can register losses of over 6 kW. Insulation materials with thermal conductivity values below 0.037 W m^{-1} K^{-1} should be used to reduce these losses, as well as minimal piping lengths, bends and elevation changes (Rayes & Ghaith, 2025).

Issues such as scaling and fouling can be minimized through the use of self-cleaning surfaces, anti-fouling coatings and insulation materials, while crystallization can be avoided with real-time crystallization control (Rayes & Ghaith, 2025).

2.4. Performance

The heat pump's coefficient of performance varies greatly according to the number of effects (Leonzio, 2017). The maximum COP for a half effect absorption heat pump (with Li-Br/H2O) is reported to be around 0.38 (Leonzio, 2017), while requiring larger collector and heat exchanger areas relatively to an equivalent single effect heat pump (Gebreslassie, Medrano, & Boer, 2010).

The average COP ranges, heat input temperatures and applications for single, double and triple-effect can be found in Table 1:

Table 1: Main characteristics of single, double and triple effect absorption heat pumps (Rayes & Ghaith, 2025).

Type	COP range	Heat input temperature [°C]	Applications
Single-effect	0.6-0.8	70-95	Residential cooling
Double-effect	1.0-1.2	120-180	Commercial HVAC systems
Triple-effect	1.3-1.6	>200	Industrial refrigeration

The coefficient of performance is also heavily related to the temperature in each component, as well as the temperature difference between the hot and cold side of the heat pump (the condenser and evaporator, respectively). It displays a direct relationship with the increase of the temperature in the generator and in the evaporator, and an indirect relationship with the increase of the temperature in the condenser, in the absorber, and with the difference of temperature between the hot and cold sides (Lahoud, Brouche, Lahoud, & Hmadi, 2021).

The COP is also shown to be a function of the working fluid properties, as well as their flow rates. While higher flow rates increase the cooling power, they also increase the required pumping energy, so a system's ability to control the flow rate is essential to maintain a good performance throughout the whole year (Rayes & Ghaith, 2025).

An impressive COP value of 2.3 has been achieved by the Changle hotel system, which consists in a hybrid solar-gas system with intelligent switching between modes (Rayes & Ghaith, 2025).

In hot weather conditions, enhanced thermodynamic cycle designs show a significant improvement in performance. The performance of an absorption heat pump may be optimized for different input conditions through different configurations like parallel, series, or reverse flow, direct-fired, dual-pressure and triple-effect. Series flow is indicated for temperatures above 150 °C, while reverse flow for heat source temperatures between 120 and 150 °C, so these cycles are considered appropriate for systems with dual-source power, such as direct-fired absorption chillers, which may use natural gas. Studies show that triple-effect systems with parallel flow and integrated compressors can reach a COP of 2.13, showing promise for future applications (Rayes & Ghaith, 2025).

The solar fraction of SPACS is limited by their high investment, with 0.74 representing a typical value (Tsoutsos, Aloumpi, Gkouskos, & Karagiorgas, 2010). A simulation done with TRNSYS showed that an area of 12 m^2 of evacuated tube collectors with 2 m^3 of thermal storage would be enough to successfully cool a room of 14 m^2 without the use of any auxiliary systems (Asim, Dewsbury, & Kanan, 2016).

2.5. Economic viability

The International Energy Agency has showed that investments for solar powered absorption cooling systems may cost on average 2100 € per kW of cooling capacity for systems with a capacity under 10 kW, with this value reducing to 1000 € / kW for projects over 500 kW (Rayes & Ghaith, 2025). Other sources present ranges from 3000 to 4500 € / kW, with the absorption heat pump corresponding to approximately a third of the investment (Ramlee, et al., 2026).

Studies show that the financial success of SPACS is a function of the solar availability of the area, collector type, and system capacity and operational methods, with payback periods reported between 4 and 35 years (Rayes & Ghaith, 2025).

The UAE system achieved lifecycle costs 43% lower than those of conventional vapor compression systems, while operating with a COP of 0.79 and a solar fraction of 0.73 (Rayes & Ghaith, 2025).

Standardized studies such as life-cycle cost analysis (LCCA) must be developed in order to further validate obtained results. Life-cycle assessments (LCA) and life-cycle cost analysis of several system configurations in various climates are required (Rayes & Ghaith, 2025).

2.6. Final remarks and development prospects

The International Energy Agency (IEA) has played an important part in expanding the implementation of SPACS throughout the world, helping to improve their efficiency and cost-effectiveness, while projects like that of the Fraunhofer Institute in Germany or the CIESOL facility in Spain are already considered successful. However, absorption systems remain with a penetration of only 1% within the cooling market. This is due to technical barriers, economic challenges and insufficient government support. Some of the issues arise with the relatively high area needed for solar collectors, since this makes it harder to implement SPACS on urban areas. Additionally, the use of high-efficiency collectors, thermal storage and auxiliary systems result in higher initial investments than those of conventional vapor compression systems (Rayes & Ghaith, 2025).

Optimization studies commonly focus on COP and the solar fraction but neglect economic viability and environmental impacts. Despite the high initial investment, research shows that regions with a high availability of solar resource experience long-term environmental advantages and economic benefits (Rayes & Ghaith, 2025).

Additionally, the Fraunhofer ISE research has concluded that SPACS can reduce peak electricity use by 8%. Apart from the economic benefits that result from this, the increase in grid stability should also be noted, which is often neglected in economic studies (Rayes & Ghaith, 2025).

The determination of the competitiveness of such systems therefore requires not only the study of the thermal performance, but also of the economic viability, environmental impacts and ability to stabilize the grid (Rayes & Ghaith, 2025).

Action must be taken by government entities and regulatory agents in the form of measures such as subsidies, tax credits or carbon pricing, in order to make SPACS more appealing for companies and investors. National and local policymakers should base themselves in results shared by the IEA and research institutes to create regulatory frameworks (Rayes & Ghaith, 2025).

Additional long-term experimental studies are required in order to conclude about the real durability and maintenance requirements of SPACS. Important factors are namely the sorbent's lifespan, pump failure rates and issues like corrosion and crystallization. Such studies are necessary to relate the system's performance with real weather and demand variations, hereby validating (or not) the existing models. These tests should be done on several climate conditions to develop standardized system configurations as a function of environmental conditions, which is essential for expanding the implementation of SPACS (Rayes & Ghaith, 2025).

The obtainment of precise real-time weather data is also crucial for the implementation of sophisticated control systems, which have the ability of optimize flow rates, generator temperatures and auxiliary power usage given the current conditions (Rayes & Ghaith, 2025).

An expanded implementation of SPACS thus requires extensive field testing to understand the performance of such systems in real-life conditions and to develop standardized configurations. Policy incentives are also required, along with the development of hybrid systems to expand the viability and implementation of SPACS (Rayes & Ghaith, 2025).

3. System modelling

The proposed system is composed of evacuated tube solar collectors, an absorption heat pump and two thermal energy storage systems. Each component is treated as an individual subsystem and is therefore modelled independently from the remaining system. The complete system model is obtained by the integration of all the subsystems.

In this section, the overall system configuration, operation, and implementation are first presented. This is followed by subsections dedicated to each of the components, where the modelling method, numerical implementation and validation approach (when applicable) are described.

3.1. System configuration and operation control

The proposed system is composed of an evacuated tubes solar collector, an absorption heat pump and two thermal storage circuits, each at a different temperature level. Each thermal storage circuit is composed of a heat exchanger and a tank, as shown in Figure 7.

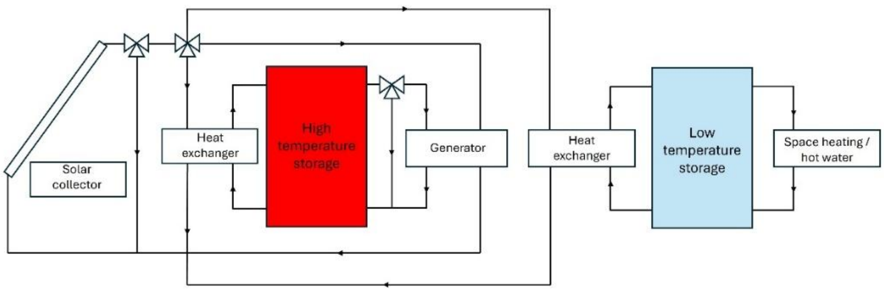

Figure 7: Configuration of the proposed system.

Note that in Figure 7, as well as in Figure 8, the absorption heat pump is represented only through its generator.

To account for stratification in the storage tanks, these components have been modelled as four separate tanks (two per storage circuit), each with a uniform temperature throughout. A representation of the modelled system can be found in Figure 8:

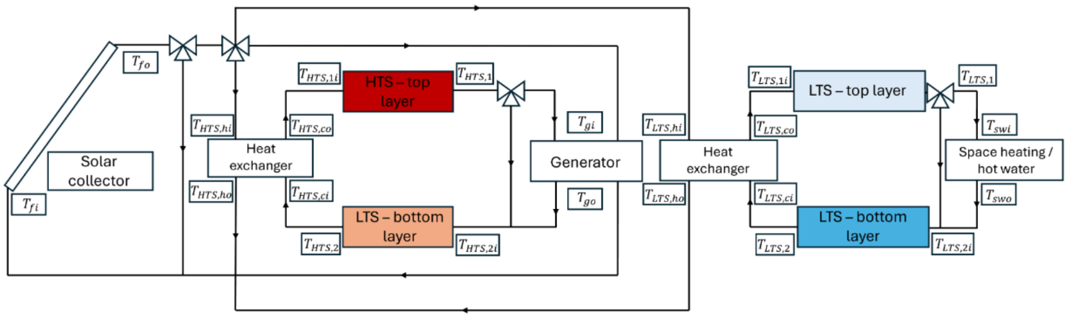

Figure 8: Model representation of the proposed system.

For each simulated time step, the ambient conditions are evaluated, enabling the system to make a series of decisions. The system produces thermal energy through the evacuated tubes solar collector and provides said heat to the absorption heat pump and to both the storage circuits. The absorption heat pump provides cooling and can be supplied by the high temperature storage in periods with low solar availability. The low temperature storage is used for heating applications (space heating and domestic hot water). Both the storage tanks have electric resistances as auxiliary energy systems, each placed in the warm layer (top tank) of the respective storage system. The system's operation is explained in more detail below, with emphasis on the operation conditions of each component, as well as the control of the solar collectors' output and the supply of the heat pump.

The collector's operation depends on environmental conditions and the current fluid inlet temperature, as illustrated in Figure 9:

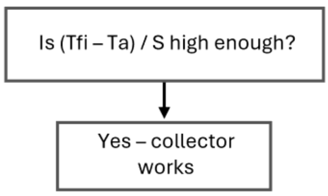

Figure 9: Solar collector control.

The thermal energy produced by the solar collectors is then distributed by the system's components according to the current conditions and demands. The collector prioritizes supplying thermal energy to the absorption heat pump and any excess energy is delivered to the storage systems. Note that the high temperature storage system only works during the cooling season (the months in which a cooling demand exists), during which the low temperature storage system is only charged when the high temperature storage is above a certain threshold. The collector's output control is illustrated in Figure 10:

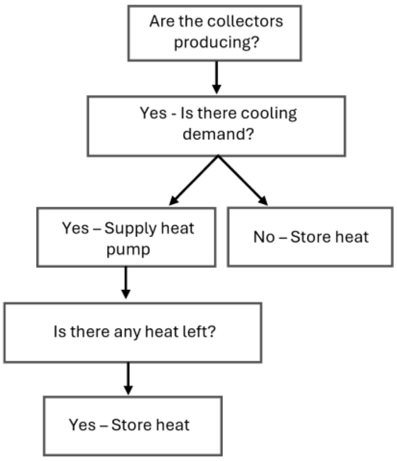

Figure 10: Solar collectors' output control.

The heat pump's operation depends on whether a cooling demand exists, as well as if there enough thermal energy being produced by the collector or stored in the high temperature storage system, such as illustrated in Figure 11:

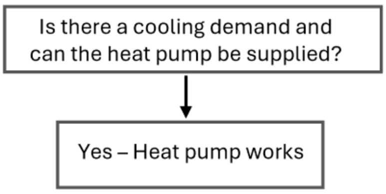

Figure 11: Heat pump control.

The heat pump can either be supplied directly by the collector or by the high temperature storage system, in function of the outlet temperature of the collector as well as the temperature in the high temperature storage system, according to Figure 12:

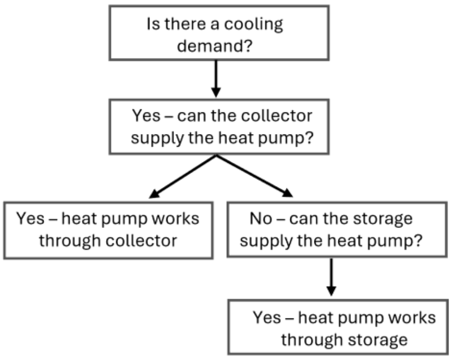

Figure 12: Heat pump supply control.

The operation of the thermal energy storage systems depends on whether there is a corresponding demand, as well as on the current temperature of the storage. Specifically, the high temperature storage works when there is a cooling demand but the heat pump cannot be supplied by the collector, and the low temperature storage works when there is a space heating or domestic hot water demand. Each storage system has minimum temperature thresholds that must be verified in order for the storage to discharge. This is illustrated in Figure 13:

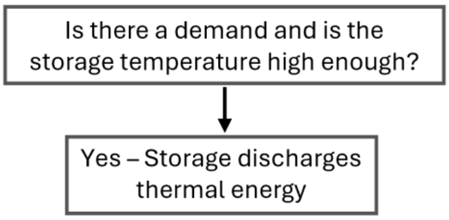

Figure 13: Thermal energy storage control.

The auxiliary systems work whenever the respective storage system's temperature drops below a certain value, considering once again that the high temperature storage system is only active during the cooling period. This is illustrated by Figure 14:

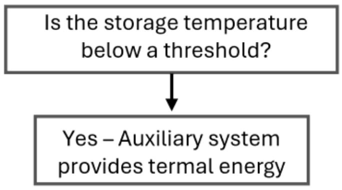

Figure 14: Auxiliary system control.

3.1.1. Numerical implementation

The system iterates through the intended time span using a time step of one minute, during which the conditions are assumed to remain constant.

In each time step, the solar collectors' operating condition is evaluated through the parameter $\frac{(T_{fi}-T_a)}{S}$, where T_{fi} represents the inlet temperature to the collectors, T_a the ambient temperature and S the irradiance absorbed by the collector. The solar collectors work if this value is below a defined threshold, derived from the collector's efficiency curve. Note that the absorbed irradiance was used instead of the incident irradiance because this method accounts for optical losses that would be underestimated by the standard efficiency curve. A maximum system temperature was adopted based on the pressure in the circuit, after which the collector stops producing thermal energy.

The functions corresponding to each component are then called in a sequential manner, starting by the solar collector, then the absorption heat pump, the high temperature storage and the low temperature storage. At the end of each simulated minute, the collectors' inlet temperature is updated and used as an initial condition for the subsequent step.

Note that since the heat pump's operating conditions were considered fixed, this component was coupled with the remaining system through a duty cycle approach, which allowed to control its output.

All fluid properties were obtained through the software REFPROP 9 and the model was implemented in MATLAB R2025a.

3.2. Solar collectors

The configuration of the evacuated tubes solar collector is represented by Figure 15 (transversal view of an evacuated tube), Figure 16 (longitudinal view of the manifold) and Figure 17 (transversal view of the manifold).

Since the evacuated tubes have been assumed to be of the heat pipe type, Figure 15 includes the following components: an outer glass tube (the glass cover), an inner glass tube with an absorptive coating (the absorber), a copper fin, and the evaporator tube:

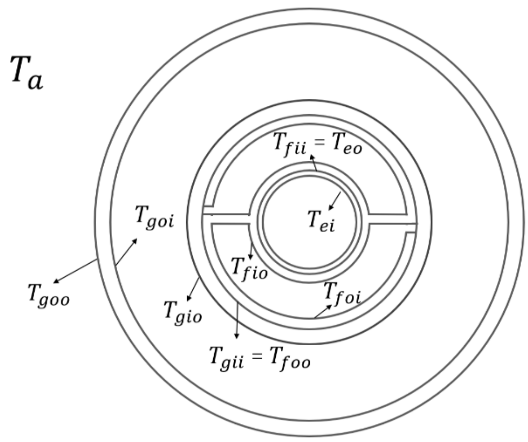

Figure 15: Evacuated tube transversal view.

While in Figure 16 and Figure 17, the following components are illustrated: the evaporator tube, both the condenser tubes (on the heat pipe side and on the manifold side), the manifold's main tube, the isolation and the outer casing:

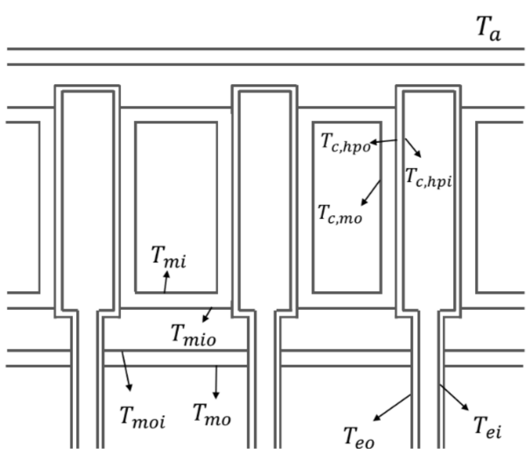

Figure 16: Manifold longitudinal view.

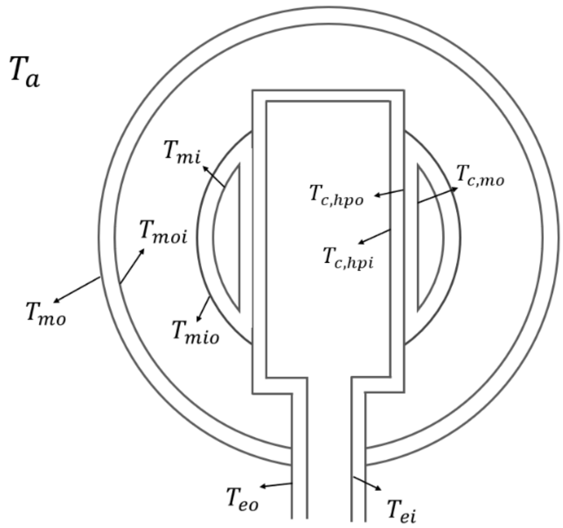

Figure 17: Manifold transversal view.

The collector may also be represented through a thermal resistance network, such as the one presented in Figure 18, which has been simplified in order to obtain the three main thermal resistances that occur: the resistance between the absorber and the environment (through the glass tube - $\dot{Q}_{gi-a}$), between the absorber and the working fluid (through the heat pipe - $\dot{Q}_{gi-f}$) and between the working fluid and the environment (through the manifold - $\dot{Q}_{f-a}$).

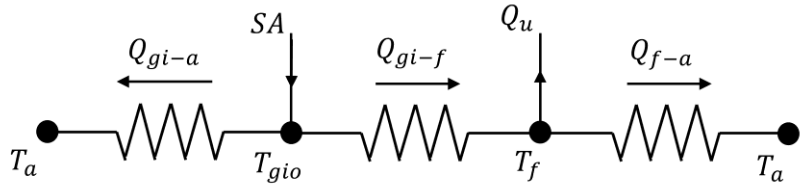

Figure 18: Simplified thermal resistance network of the solar collector.

The collector is modelled under steady-state assumptions using a system of equations based on the expressions presented in the current section.

Applying an energy balance to the whole system results in Eq. (2):

$$SA_{abs} = \dot{Q}_U + \dot{Q}_L \tag{2}$$

With S representing the absorbed irradiation (calculated in Section 3.2.1), A_{abs} the projected absorber area, $\dot{Q}_U$ the useful power produced by the collector, and $\dot{Q}_L$ the thermal losses of the system, which corresponds to the sum of $\dot{Q}_{gi-a}$ and $\dot{Q}_{f-a}$.

The absorber area is given by Eq. (3), accordingly to (ISO, 1999):

$$A_{abs} = ND_{gio}L_e \tag{3}$$

Where N represents the number of tubes of the collector, D_{gio} the outer diameter of the absorber, and L_e the length of the absorber tube. Note that it was considered that the outer and inner glass tubes, the fin and the evaporator tube all have the same length.

For each component of the system, the relationship between the heat transfer rate, the thermal resistance and the temperature difference can be written as seen in Eq. (4):

$$\dot{Q} = \frac{\Delta T}{R} \tag{4}$$

It is also necessary to apply an energy balance to the working fluid, resulting in Eq. (5):

$$\dot{Q}_U = \dot{m}c\left(T_{fo} - T_{fi}\right) \tag{5}$$

In which $\dot{m}$ represents the mass flow rate in the manifold, and T_{fo} and T_{fi}, respectively, the collector's outlet and inlet temperatures.

The efficiency of the solar collector may be given by Eq. (6):

$$\eta = \frac{\dot{Q}_U}{A_{ap}\, I_{sc}} \tag{6}$$

In which A_{ap} represents the aperture area and I_{sc} the incident radiation in the collector plane.

The aperture area, according to (ISO, 1999), is calculated through Eq. (7):

$$A_{ap} = ND_{goi}L_e \tag{7}$$

Where D_{goi} represents the inner diameter of the outer glass tube.

The incident radiation can be calculated using the isotropic diffuse model, expressed by Eq. (8), which has been adapted from (Duffie & Beckman, 2013) to account for the use of the direct normal irradiance:

$$I_{sc} = cos(\theta)\, I_{BN} + \left(\frac{1 + cos(\beta_{sc})}{2}\right) I_{DH} + \rho \left(\frac{1 - cos(\beta_{sc})}{2}\right) I_{GH} \qquad (8)$$

In which θ represents the incidence angle, calculated by Eq. (20) in the subsection 3.2.1, I_{BN} the direct irradiance in a plane that is normal to the sun rays, β_{sc} the inclination of the solar collector, I_{DH} the diffuse irradiance on the horizontal plane, ρ the reflectivity / albedo of the environment, and I_{GH} the global irradiance on the horizontal plane.

Eq. (2) may be rearranged and elaborated, and thus used to substitute $\dot{Q}_U$ in Eq. (6), resulting in Eq. (9). This method uses the same reference areas as (Beekers, 2021), while maintaining the standard useful power calculation with the heat removal factor (Duffie & Beckman, 2013):

$$\eta = \frac{A_{abs} F_R (\tau\alpha)}{A_{ap}} - \frac{A_{abs} F_R U_L \left(T_{fi} - T_a\right)}{A_{ap}\, I_{sc}} \qquad (9)$$

Where F_R represents the heat removal factor, $(\tau\alpha)$ the collector's optical efficiency, U_L the heat loss coefficient, and T_a the ambient temperature. The optical efficiency was assumed to be given by the product of the transmissivity of the glass cover and the absorptivity of the absorber.

When Eq. (9) is expressed in function of the group $\frac{(T_{fi}-T_a)}{I_{sc}}$, the resulting coefficients may then be used to verify the model's accuracy, since manufacturers commonly report these values.

3.2.1. Determination of the absorbed irradiance

The absorbed irradiance is given by the multiplication of each component in Eq. (8) by the normal incidence optical efficiency and by its corresponding angle modifier, resulting in Eq. (10):

$$S = (\tau\alpha)_n \left(cos(\theta)\, k_{\theta,BN}\, I_{BN} + \frac{1 + cos(\beta_{sc})}{2}\, k_{\theta,DH}\, I_{DH} + \rho\, \frac{1 - cos(\beta_{sc})}{2}\, k_{\theta,GH}\, I_{GH} \right) \tag{10}$$

With $(\tau\alpha)_n$ representing the optical efficiency for normal incidence, $k_{\theta,BN}$ the direct irradiance angle modifier, $k_{\theta,DH}$ the diffuse irradiance angle modifier and $k_{\theta,GH}$ the reflected irradiance angle modifier.

Given the geometry of an evacuated tube solar collector, it is necessary to decompose the incidence angle into its two components (transversal and longitudinal) to obtain the direct irradiance angle modifier.

The calculation of the incidence angle components is presented in Appendix A.

Once the transversal and longitudinal components of the incidence angle have been calculated, Table 2 is then interpolated and used to determine the transversal and longitudinal angle modifiers. The final angle modifier is given by Eq. (11) (Kalogirou, 2024):

$$k_\theta = k_{\theta,t}\, k_{\theta,l} \tag{11}$$

Where $k_{\theta,t}$ represents the transversal incidence angle modifier and $k_{\theta,l}$ the longitudinal incidence angle modifier.

To obtain the diffuse and reflected irradiance angle modifiers (θ_D and θ_R, respectively), the corresponding equivalent angles have been determined through Eq. (12) and Eq. (13) (Kalogirou, 2024):

$$\theta_D = 59.68 - 0.1388\, \beta_{sc} + 0.001497\, \beta_{sc}^2 \tag{12}$$

$$\theta_R = 90 - 0.5788\, \beta_{sc} + 0.002693\, \beta_{sc}^2 \tag{13}$$

These were assumed to represent the longitudinal components of each equivalent angle, while the transversal components were assumed to be 0°. The diffuse and reflected irradiance angle modifiers were then obtained analogously to the direct irradiance incidence angle.

To calculate the incidence angle, the declination angle was first determined through Eq. (14) (Kalogirou, 2024):

$$\delta = 23.45 \, sin\left(\frac{360}{365} \, (284 + N)\right) \tag{14}$$

With N representing the day of the year (between 1 and 365).

The hour angle is determined through Eq. (15) (Kalogirou, 2024):

$$h = (AST - 12) \, \frac{360}{24} \tag{15}$$

In which AST represents the apparent solar time, calculated by Eq. (16) (Kalogirou, 2024):

$$AST = LST + ET + CL \tag{16}$$

With LST representing the local standard time, ET the equation of time, and LC the longitude correction. ET is given, in minutes, by Eq. (17) (Kalogirou, 2024):

$$ET = 9.87 \, sin(2B) - 7.53 \, cos(B) - 1.5 \, sin(B) \tag{17}$$

With B calculated through Eq. (18) (Kalogirou, 2024):

$$B = (N - 81) \, \frac{360}{365} \tag{18}$$

The longitude correction is calculated through Eq. (19) (Kalogirou, 2024):

$$LC = 4 \, (SL - LL) \tag{19}$$

With SL representing the standard longitude (Greenwich at 0°) and LL the local longitude. The longitude correction must be negative for locations west of the standard longitude and positive for locations east of Greenwich.

The incidence angle was then obtained through Eq. (20) (Kalogirou, 2024):

$$\theta = cos\big(sin(\delta)\, sin(L)\, cos(\beta_{sc}) - sin(\delta)\, cos(L)\, sin(\beta_{sc})\cos(Z_{sc}) + \cos(\delta)\cos(L)\cos(\beta_{sc})\cos(h) + \cos(\delta)\sin(L)\sin(\beta_{sc})\cos(Z_{sc})\cos(h) + \cos(\delta)\sin(\beta_{sc})\sin(Z_{sc})\sin(h)\big)^{-1} \tag{20}$$

Where L represents the latitude and Z_{sc} represents the solar collector's azimuth angle.

3.2.1.1. Incidence angle modifiers

The transversal and longitudinal angle modifier values ($k_{\theta,t}$ and $k_{\theta,l}$, respectively) used in this work have been taken from (Horta, Zaragoza, & Alarcón-Padilla, 2014), where they are assumed to represent the typical behaviour of an evacuated tube collector. These can be seen in Table 2:

Table 2: Assumed incidence angle modifier values.

θ [°]	0	10	20	30	40	50	60	70	80	90
$k_{\theta,t}$	1.00	1.03	1.05	1.10	1.20	1.15	1.05	0.80	0.50	0.00
$k_{\theta,l}$	1.00	1.00	0.99	0.98	0.97	0.94	0.90	0.81	0.52	0.00

3.2.2. Determination of the thermal resistances

Each of the three main thermal resistances has been elaborated into all its components, which will be presented in the following subsections.

3.2.2.1. Absorber - environment

The thermal resistance between the absorber and the environment (R_{gi-a}) can be split into the radiative resistance between the inner and outer glass tubes, the conductive resistance through the glass cover and the convective and radiative resistances between the glass cover and the environment, as shown in Figure 19:

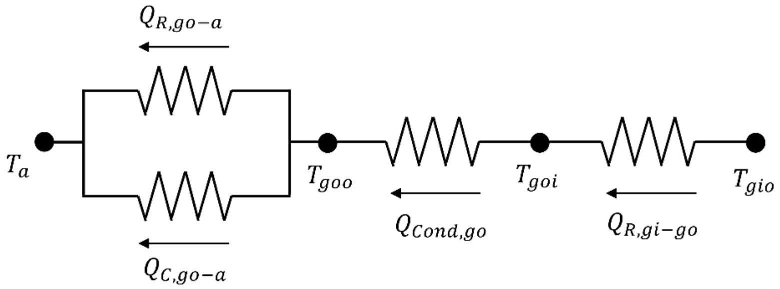

Figure 19: Thermal resistance network between the absorber and the environment.

Resulting in Eq. (21):

$$R_{gi-a} = \left(\frac{1}{R_{R,go-a}} + \frac{1}{R_{C,go-a}}\right)^{-1} + R_{Cond,go} + R_{R,gi-go} \tag{21}$$

The radiative thermal resistance between the two glass tubes ($R_{R,gi-go}$) is calculated through Eq. (22):

$$R = \frac{1}{A\,h} \tag{22}$$

Where A represents the area of which the heat transfer originates from, in this case the outer area of the absorber (A_{gio}), and h represents the heat transfer coefficient, in this case the radiative heat transfer coefficient between the two glass tubes ($h_{R,gi-go}$), given by Eq. (23) (Kalogirou, 2024):

$$h_R = \frac{\sigma\,(T_1^2 + T_2^2)\,(T_1 + T_2)}{\frac{1-\varepsilon_1}{\varepsilon_1} + \frac{1}{F_{12}} + \frac{A_1}{A_2}\left(\frac{1-\varepsilon_2}{\varepsilon_2}\right)} \tag{23}$$

In which σ represents the Stefan-Boltzmann constant, ε the emissivity of each surface, and F the view factor from surface 1 to surface 2. In this case, the subscript 1 refers to the outer surface of the absorber and subscript 2 refers to the inner surface of the glass cover, hence the view factor was considered to be 1.

The conductive thermal resistance across the glass cover ($R_{Cond,go}$) is given by Eq. (24):

$$R_{Cond} = \frac{\ln(\frac{r_o}{r_i})}{2\,\pi\,dx\,k} \tag{24}$$

Where r_o and r_i represent, respectively, the outer and inner radii of the material (in this case, the outer glass tube), dx the thickness of the material and k its thermal conductivity.

Both the radiative and convective thermal resistances between the glass cover and the environment ($R_{R,go-a}$ and $R_{C,go-a}$) are calculated through Eq. (22), where A corresponds to the outer area of the glass cover, and h represents the respective radiative thermal resistance or convective thermal resistance, accordingly.

The radiative heat transfer coefficient between the glass cover and the environment ($h_{R,go-a}$) is given by a simplified form of Eq. (23): due to the large order of magnitude of the sky area relatively to the tube area, the general expression is reduced to Eq. (25):

$$h_R = \sigma\,\varepsilon_1\left(T_1^2 + T_{sky}^2\right)\left(T_1 + T_{sky}\right) \tag{25}$$

Where the subscript 1 represents the outer surface of the glass cover, and T_{sky} corresponds to the sky temperature, calculated through Eq. (26) (Kalogirou, 2024):

$$T_{sky} = 0.0552\,T_a^{1.5} \tag{26}$$

While the convective heat transfer coefficient between the glass cover and the environment ($h_{C,go-a}$) is calculated through Eq. (27):

$$h_C = \frac{Nu\,k}{\mathcal{L}} \tag{27}$$

In which Nu represents the Nusselt number, k the fluid's thermal conductivity and $\mathcal{L}$ the characteristic length of the material, in this case the glass cover's outer diameter.

Since this heat transfer scenario corresponds to a cylinder subjected to external flow, the expression for calculating the Nusselt number depends on the nature of the convective process (whether it is forced or natural). If wind exists, convection is assumed to be forced and the Nusselt number is calculated through Eq. (28) for a cylinder in cross flow (Incropera, Dewitt, Bergman, & Lavine, 2007):

$$Nu_f = 0.3 + \frac{0.62\, Re^{1/2}\, Pr^{1/3}}{\left[1+\left(\frac{0.4}{Pr}\right)^{2/3}\right]^{1/4}} \left[1+\left(\frac{Re}{282000}\right)^{5/8}\right]^{4/5} \tag{28}$$

In which Re represents the Reynolds number, and Pr the Prandtl number. This equation is recommended for approximately $Re\, Pr \geq 0.2$, with all the properties evaluated at the film temperature.

The Reynolds number is given by Eq. (29):

$$Re = \frac{\rho\, v\, \mathcal{L}}{\mu} \tag{29}$$

With ρ representing the density of the fluid (in this case, air), v its velocity and μ its dynamic viscosity.

The Prandtl number is given by Eq. (30):

$$Pr = \frac{\mu\, c}{k} \tag{30}$$

With c representing the heat capacity at constant pressure of the fluid.

If wind does not exist, convection is assumed to be natural, and Eq. (31) for a cylinder in external free flow is used to calculate the Nusselt number (Incropera, Dewitt, Bergman, & Lavine, 2007):

$$Nu_n = \left(0.6 + \frac{0.387\, \sqrt[6]{Ra}}{\left(1+\left(\frac{0.559}{Pr}\right)^{9/16}\right)^{8/27}}\right)^2 \tag{31}$$

In which Ra represents the Rayleigh number. This relationship is valid for $Ra \leq 10^{12}$, with all the properties evaluated at the film temperature. The Rayleigh number is calculated through Eq. (32):

$$Ra = \frac{g\ \beta\ Pr\ \Delta T\ \mathcal{L}^3}{\nu^2} \tag{32}$$

With g representing the gravitational acceleration, β the coefficient of thermal expansion, ΔT the driving temperature difference (the surface temperature minus the bulk temperature of the fluid), and ν the kinematic viscosity.

In the present case, the bulk temperature corresponds to the ambient temperature. Otherwise, an approximation of the bulk temperature may be obtained through Eq. (33):

$$T_b = \frac{T_i + T_o}{2} \tag{33}$$

Where T_i represents the fluid's inlet temperature in the tube and T_o the fluid's outlet temperature in the tube.

While the kinematic viscosity is calculated through Eq. (34):

$$\nu = \frac{\mu}{\rho} \tag{34}$$

3.2.2.2. Absorber - fluid

The thermal resistance between the absorber and the fluid (R_{gi-f}) can be split into the resistances that correspond to the inner glass tube, the fin, the heat pipe and the condenser tube (on the manifold side).

The resistance of the fin can be further broken down into five components (the conductive resistances on the outer and inner fin sections, and conductive, convective and radiative resistances in the middle fin section), while the resistance of the heat pipe may be split into four components (conductive resistance in the evaporator and condenser tube – heat pipe side, the boiling resistance in the evaporator, and the condensation resistance in the condenser), and the manifold condenser tube into two (conductive and convective resistances). This results in the thermal resistance network illustrated in Figure 20:

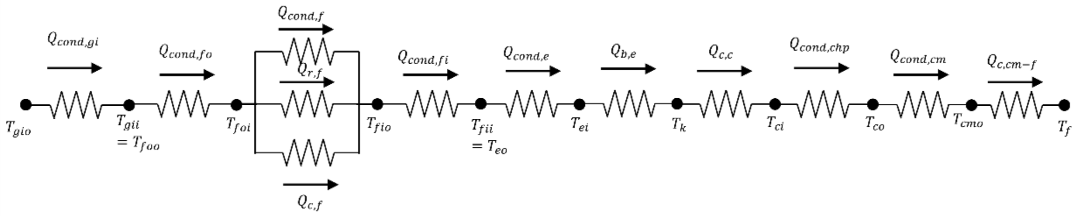

Figure 20: Thermal resistance network between the absorber and the fluid.

The equivalent thermal resistance is hence given by Eq. (35):

$$R_{gi-f} = R_{Cond,gi} + R_{Cond,fo} + \left(\frac{1}{R_{Cond,f}} + \frac{1}{R_{R,f}} + \frac{1}{R_{C,f}}\right)^{-1} + R_{Cond,fi} + R_{Cond,e} + R_{b,e} + R_{c,c} + R_{Cond,chp} + R_{Cond,cm} + R_{C,cm-f} \quad (35)$$

The conductive resistance through the inner glass tube ($R_{Cond,gi}$) is given by Eq. (24), using the inner glass' outer and inner radius, thickness and thermal conductivity.

The fin, as stated previously, has been modelled as five different thermal resistances: conduction through the outer section of the fin; conduction, radiation and convection in the middle section of the fin; and conduction through the inner section of the fin. The conductive resistances both in the outer and inner sections of the fin ($R_{Cond,fo}$ and $R_{Cond,fi}$) are given by Eq. (24), using the respective outer and inner radii, thickness and thermal conductivity.

In the middle section of the fin, the conductive resistance ($R_{Cond,f}$) is calculated through Eq. (36):

$$R_{Cond} = \frac{L}{A\,k} \quad (36)$$

Where L represents the length of the material (in this case the length between the inner and outer sections of the fin), A the area of the middle section of the fin and k its thermal conductivity. Note that this component must be accounted for twice (once for each parallelepiped), considering a parallel relationship between the two.

The radiative resistance in the middle section of the fin ($R_{R,f}$) is given by Eq. (22), using the inner area of the outer fin section and the coefficient of heat transfer given by Eq. (23), where the subscript 1 corresponds to the inner surface of the outer section of the fin, subscript 2 to the outer surface of the inner section of the fin, and the view factor is given by Eq. (37) for concentric infinite cylinders (Martínez, s.d.):

$$r = \frac{r_i}{r_o} \tag{37}$$

Where r_i corresponds to the outer radius of the inner fin section and r_o corresponds to the inner radius of the outer fin section.

The convective resistance in the middle section of the fin ($R_{C,f}$) is given by Eq. (24), where the outer radius is that of the inner surface of the outer section of the fin, the inner radius is that of the outer surface of the inner section of the fin, the thickness is the length of the tube and k, in this case, corresponds to an effective conductivity, calculated through Eq. (38) (Incropera, Dewitt, Bergman, & Lavine, 2007):

$$k_{ef} = 0.386\, k \left(\frac{Pr}{0.861 + Pr}\right)^{\frac{1}{4}} Ra^{\frac{1}{4}} \tag{38}$$

With the Rayleigh number evaluated using the length scale obtained through Eq. (39) (Incropera, Dewitt, Bergman, & Lavine, 2007):

$$L_c = \frac{2\, log\left(\frac{r_o}{r_i}\right)^{\frac{4}{3}}}{\left(r_o^{-\frac{3}{5}} + r_i^{-\frac{3}{5}}\right)^{\frac{5}{3}}} \tag{39}$$

Where r_o and r_i correspond to the same radii as those used for Eq. (37).

The conductive resistance through the evaporator tube ($R_{Cond,e}$) is given by Eq. (24), where r_o corresponds to the outer evaporator radius, r_i to the inner evaporator radius, dx to the tube's length and k to the evaporator's thermal conductivity.

The boiling resistance in the evaporator ($R_{b,e}$) and condensation resistance in the condenser ($R_{c,c}$) are calculated through the method used by Roetzel, Heggs, & Butterworth, which considers both the boiling pool resistance and the liquid film resistance. The boiling pool resistance is given by Eq. (40) (Roetzel, Heggs, & Butterworth, 1991):

$$R_{bp} = \frac{1}{c_b\, g^{0.2}\, \dot{Q}_{hp}^{0.4}\, (\pi\, D\, L)^{0.6}} \tag{40}$$

Where c_b represents the boiling figure-of-merit, $\dot{Q}_{hp}$ the heat transfer rate in the heat pipe, D the diameter and L the length of the pipe. The boiling figure-of-merit is obtained through Eq. (41) (Roetzel, Heggs, & Butterworth, 1991):

$$c_b = \frac{k_l^{0.3} \rho_l^{0.65} c_l^{0.7} P^{0.23}}{P_a^{0.23} \mu_l^{0.1} h_{fg}^{0.4} \rho_v^{0.25}} \quad (41)$$

Where P represents the fluid's pressure, P_a the atmospheric pressure, h_{fg} the fluid's enthalpy of vaporization, the subscript l represents liquid and the subscript v vapor. Note that the liquid properties and the latent heat should be evaluated at the saturation temperature, while the vapor density should be evaluated at the film temperature (Incropera, Dewitt, Bergman, & Lavine, 2007).

The liquid film resistance is given by Eq. (42) (Roetzel, Heggs, & Butterworth, 1991):

$$R_{lf} = 0.235 \frac{\dot{Q}_{hp}^{\frac{1}{3}}}{D^{\frac{4}{3}} g^{\frac{1}{3}} L c_c^{\frac{4}{3}}} \quad (42)$$

Where c_c represents the condensation figure-of-merit, calculated through Eq. (43) (Roetzel, Heggs, & Butterworth, 1991):

$$c_c = \left(\frac{h_{fg} k_l^3 \rho_l^2}{\mu_l} \right)^{0.25} \quad (43)$$

With the liquid properties evaluated at the film temperature, while the latent heat is evaluated at the saturation temperature (Incropera, Dewitt, Bergman, & Lavine, 2007).

The final expression for the boiling resistance depends on the values of the boiling pool and the liquid film resistances. If R_{lf} > R_{bp}, then $R_{b,e} = R_{bp}$. If this condition is not verified, then the boiling resistance is given by Eq. (44) (Roetzel, Heggs, & Butterworth, 1991):

$$R_{b,e} = F R_{bp} + (1 - F) R_{lf} \quad (44)$$

Where F represents the fill ratio, here assumed to be 0.35 (Mozumder, Akon, Chowdhury, & Banik, 2011). The boiling resistance in the evaporator should be calculated using the evaporator's inner diameter and length.

The condensation resistance in the condenser ($R_{c,c}$) is given by Eq. (42), using the condenser's inner diameter and length.

Both the resistances corresponding to the condenser tube (on the heat pipe and manifold side - $R_{Cond,chp}$ and $R_{Cond,cm}$, respectively) are given by Eq. (24). Since both components have the same material and length, their combined resistance may be calculated using the manifold side tube's outer radius and heat pipe side tube's inner radius, along with the condenser length and thermal conductivity.

The convective resistance between the condenser tube and the working fluid ($R_{C,cm-f}$) is given by Eq. (22), with the condenser tube's outer area and the coefficient calculated through Eq. (27), using the condenser's outer diameter as the characteristic length. Note that only the condenser's lateral area was considered as the heat transfer surface. In this case, the convective process may occur under natural, forced, or mixed regime. The prevailing regime is determined through the Richardson number: convection is assumed to be forced if this number is below 0.1, natural if it is above 10, and mixed for intermediate values (Karwa, 2020).

The Richardson number is calculated with Eq. (45):

$$Ri = \frac{Gr}{Re^2} \tag{45}$$

With Gr representing the Grashof number, calculated through Eq. (46):

$$Gr = \frac{Ra}{Pr} \tag{46}$$

The forced convection Nusselt number is here assumed to correspond to that of a uniformly heated cylinder subjected to cross flow between plates, given by Eq. (47) (Beekers, 2021):

$$Nu_f = \left(0.843 - 0.25\, e^{-2.65\, b^{\frac{5}{2}}}\right) Re^{\frac{1}{2}}\, Pr^{\frac{1}{3}} \tag{47}$$

With all the properties evaluated at the film temperature, Re and Pr calculated using the condenser's outer diameter as the characteristic length and b calculated by Eq. (48) (Beekers, 2021):

$$b = \frac{D_o}{D_i} \tag{48}$$

Where D_o corresponds to the outer diameter of the condenser tube (manifold side) and D_i to the inner diameter of the manifold's main tube.

The natural convection Nusselt number is once again given by Eq. (31), using the condenser's outer diameter as the characteristic length. Note that for water at temperatures below 3.98 °C, the coefficient of thermal expansion becomes negative due to density inversion. In this case (external natural convection from an immersed body) the buoyant force remains present (albeit with an opposite direction) (Vasseur & Robillard, 1978). Therefore, the Rayleigh number, and consequently the Nusselt number, were calculated with the coefficient of thermal expansion's absolute value.

The combined Nusselt number, which considers both the natural and forced convection, and is calculated through Eq. (49) (Incropera, Dewitt, Bergman, & Lavine, 2007):

$$Nu_c = \left(Nu_f^n + Nu_n^n\right)^{\frac{1}{n}} \tag{49}$$

Where n represents a constant dependent on the geometry of the surface. The value commonly used for cylinders is 4 (Incropera, Dewitt, Bergman, & Lavine, 2007).

3.2.2.3. Fluid - environment

The thermal resistance between the fluid (R_{f-a}) and the environment can be split into the convective resistance between the working fluid and the manifold's main tube, the conductive resistances that occur in the manifold (in the main tube, in the isolation layer and in the outer casing), and the radiative and convective resistances between the manifold's outer casing and the environment. This results in the thermal resistance network illustrated in Figure 21:

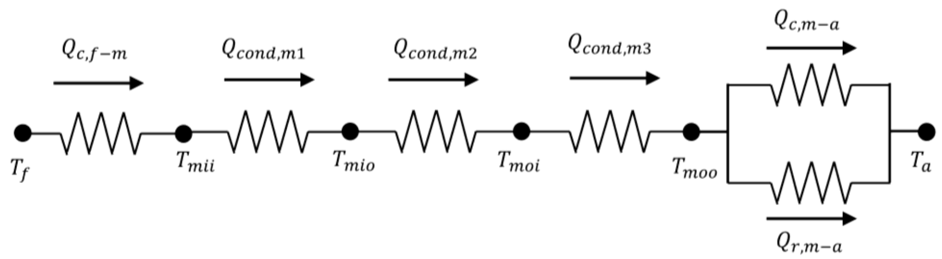

Figure 21: Thermal resistance network between the fluid and the environment.

The equivalent thermal resistance is thus given by Eq. (50):

$$R_{f-a} = R_{C,f-m} + R_{Cond,m1} + R_{Cond,m2} + R_{Cond,m3} + \left(\frac{1}{R_{R,m-a}} + \frac{1}{R_{C,m-a}}\right)^{-1} \tag{50}$$

The convective resistance between the fluid and the main tube ($R_{C,f-m}$) is given by Eq. (22), using the main tube's inner area and the coefficient calculated through Eq. (27) with the main tube's inner diameter as the characteristic length.

The method used to determine whether the convective process is natural, forced or mixed in Section 3.2.2.2 was used once again. The Nusselt number corresponding to natural convection in a horizontal cylindrical cavity is given by Eq. (51) (Ludovisi & Garza, 2013):

$$Nu_n = 1.15\, Ra^{0.22} \tag{51}$$

Where the characteristic length is the main tube's inner diameter. This equation is valid for $3 \times 10^4 \leq Ra \leq 10^{10}$ and $1 \leq Pr \leq 15$, with all properties evaluated at the mean fluid temperature. For $Ra < 3 \times 10^4$, a Nusselt number of $Nu_n = 10$ was assumed (Ludovisi & Garza, 2013).

The Nusselt number corresponding to forced convection in a circular tube depends on the flow regime. The flow is considered laminar if $Re \leq 2300$, in which case $Nu_f = 3.66$ (Incropera, Dewitt, Bergman, & Lavine, 2007). If $Re > 2300$, the flow is considered turbulent, and the Nusselt number is given by Eq. (52) (Incropera, Dewitt, Bergman, & Lavine, 2007):

$$Nu_f = \frac{\left(\frac{f}{8}\right)(\mathrm{Re} - 1000)\, Pr}{1 + 12.7\left(\frac{f}{8}\right)^{\frac{1}{2}}\left(Pr^{\frac{2}{3}} - 1\right)} \tag{52}$$

Where f represents the friction factor. This relationship has been confirmed for approximately $3000 \leq Re \leq 5 \times 10^6$, $0.5 \leq Pr \leq 2000$, and $\frac{L}{D} \geq 10$ (Incropera, Dewitt, Bergman, & Lavine, 2007). For $2300 < Re < 3000$, Eq. (52) was also used as an approximation.

The friction factor is given by Eq. (53):

$$f = (0.790 \ln \mathrm{Re} - 1.64)^{-2} \tag{53}$$

The three conductive resistances associated with the manifold tube ($R_{Cond,m1}$, $R_{Cond,m2}$ and $R_{Cond,m3}$) are all obtained through Eq. (24), each with its respective outer and inner radii, length and thermal conductivity.

The radiative and convective thermal resistances between the manifold and the environment are obtained analogously to $R_{R,go-a}$ and $R_{C,go-a}$, through Eq. (22), using the manifold's outer area, and from Eq. (25) through to Eq. (34), using the manifold's outer temperature as T_1 for the radiation heat transfer coefficient and the manifold's outer diameter as the characteristic length for the convection heat transfer coefficient.

3.2.3. Numerical implementation

The collector model code is made of two main functions and several auxiliary functions. The first main function is the base model, built for only one evacuated tube and corresponding manifold section. This function solves for the main heat transfer rates and temperatures in each tube using `fsolve` (a nonlinear equation solver that uses an interior-reflective Newton method). All the heat transfer coefficients as well as the absorbed irradiance are calculated through dedicated auxiliary functions.

The operation of the whole collector array is simulated in the second main function, where the tube function is iterated for each respective tube. The initial values required by `fsolve` are updated at every iteration based on the previously obtained results. The properties of the fluids are determined only once for each collector, since this proved to be the most time-consuming part of the model. This simplification did not affect the results in a significant manner.

3.2.4. Model validation

Given the complexity of the evacuated tubes collector model, its validation was considered necessary. The collector's performance was thus studied for a wide range of operating conditions, using the dimensions and properties presented in Section 4.4.1. A linear regression was then applied to the collector's efficiency in function of the group $\frac{(T_{fi}-T_a)}{I}$. From this study, the collector's heat loss / first order coefficient (a_1) and the zero-loss collector efficiency (η_0) were obtained. These values are presented in Table 3, along with values provided by a manufacturer:

Table 3: Solar collector study results.

	a_1 [W m^{-2} K^{-1}]	η_0 [%]
Model	1.310	72.1
Reference (Firebird, s.d.)	1.529	73.4

The referenced data sheet can be found in Section B of the appendices. Note that the reference values must be based on the same area used to calculate the efficiency (in this case, the aperture area). Considering the values on Table 3, the obtained efficiency coefficients a_1 and η_0 were deemed realistic and it was concluded that the collector model is sufficiently accurate. The resulting efficiency plot can be seen in Figure 22:

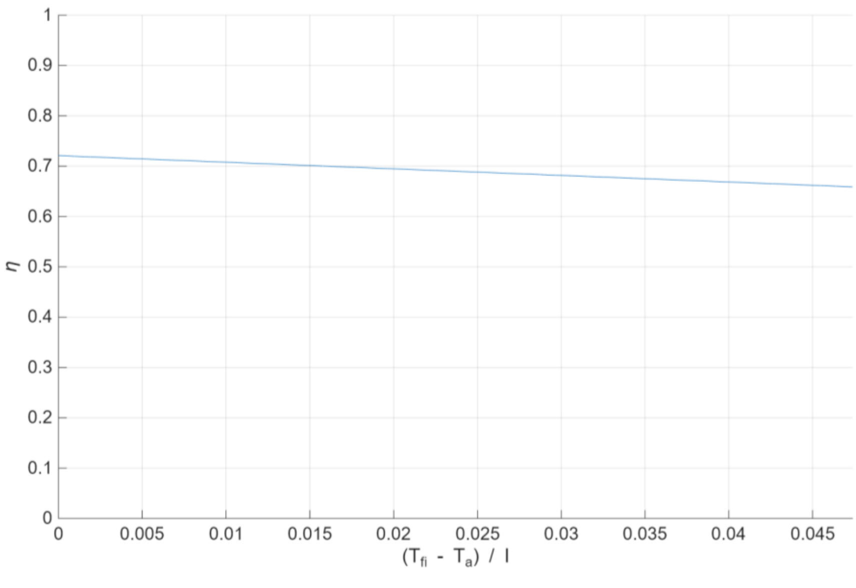

Figure 22: Solar collector efficiency plot.

Additionally, the parameter x_{crit} (maximum $\frac{(T_{fi}-T_a)}{I}$ for which the collector is able to produce useful heat) was found to be 0.550 m^2 K W^{-1}, the heat removal factor (F_R) 0.982, and the overall heat loss coefficient (U_L) 1.521 W m^{-2} K^{-1}.

3.3. Heat pump

The absorption heat pump has eight components: the condenser, the evaporator, the absorber, the heat exchanger, the generator, two valves and a circulation pump. Its configuration is represented in Figure 23.

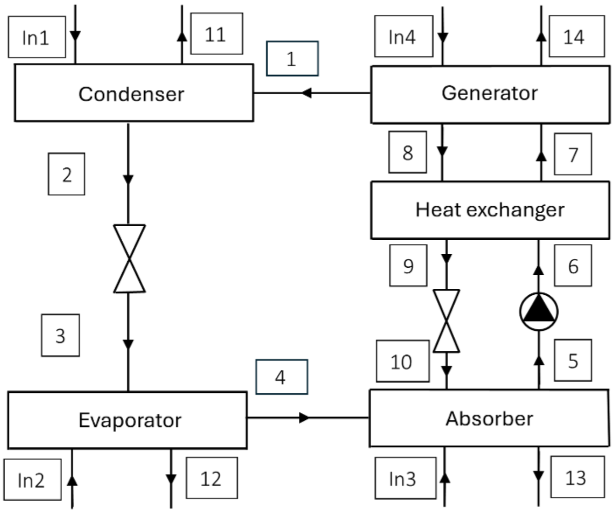

Figure 23: Configuration of the absorption heat pump.

Note that the considered fluid mixture was ammonia and water. Even though the rectifier was not modelled, it was assumed that point 1 corresponds to pure ammonia. This being said, the proposed model is applicable to other fluid mixtures.

The heat pump is modelled under steady-state assumptions using a system of equations based on the expressions presented in the current section. The mass and energy balance equations seen in Eq. (54) and Eq. (55), respectively, have been considered:

$$\sum \dot{m}_i - \sum \dot{m}_o = 0 \tag{54}$$

$$\left(\sum(\dot{m}h)_i - \sum(\dot{m}h)_o\right) + \left(\sum\dot{Q}_i - \sum\dot{Q}_o\right) + \dot{W} = 0 \tag{55}$$

In which $\dot{m}$ represents the mass flow rate, h the specific enthalpy, $\dot{Q}$ the heat transfer rate and $\dot{W}$ the work done by or to the system.

Eq. (54) and Eq. (55) were applied to each component of the system, resulting in Table 4:

Table 4: Mass and energy balances for each component.

Component	Mass balance	Energy balance
Condenser	$\dot{m}_1 = \dot{m}_2$ $\dot{m}_{in1} = \dot{m}_{11}$	$\dot{m}_1 h_1 = \dot{m}_2 h_2 + \dot{Q}_c$ $\dot{m}_{in1} h_{in1} + \dot{Q}_c = \dot{m}_{11} h_{11}$
Expansion valve	$\dot{m}_2 = \dot{m}_3$	$\dot{m}_2 h_2 = \dot{m}_3 h_3$
Evaporator	$\dot{m}_3 = \dot{m}_4$ $\dot{m}_{in2} = \dot{m}_{12}$	$\dot{m}_3 h_3 = \dot{m}_4 h_4 + \dot{Q}_e$ $\dot{m}_{in2} h_{in2} + \dot{Q}_e = \dot{m}_{12} h_{12}$
Absorber	$\dot{m}_4 + \dot{m}_{10} = \dot{m}_5$ $\dot{m}_{in3} = \dot{m}_{13}$	$\dot{m}_4 h_4 + \dot{m}_{10} h_{10} + \dot{Q}_a = \dot{m}_5 h_5$ $\dot{m}_{in3} h_{in3} = \dot{m}_{13} h_{13} + \dot{Q}_a$
Circulation pump	$\dot{m}_5 = \dot{m}_6$	$\dot{m}_5 h_5 + \dot{W}_P = \dot{m}_6 h_6$
Heat exchanger	$\dot{m}_6 + \dot{m}_8$ $= \dot{m}_7 + \dot{m}_9$	$\dot{m}_6 h_6 + \dot{m}_8 h_8 = \dot{m}_7 h_7 + \dot{m}_9 h_9$
Generator	$\dot{m}_7 = \dot{m}_8 + \dot{m}_1$ $\dot{m}_{in4} = \dot{m}_{14}$	$\dot{m}_7 h_7 = \dot{m}_8 h_8 + \dot{m}_1 h_1 + \dot{Q}_g$ $\dot{m}_{in4} h_{in4} + \dot{Q}_g = \dot{m}_{14} h_{14}$
Valve	$\dot{m}_9 = \dot{m}_{10}$	$\dot{m}_9 h_9 = \dot{m}_{10} h_{10}$

The working fluid was assumed to be in a saturated vapor state at the entry of the condenser and exit of the evaporator, and in a saturated liquid state at the exit of the condenser and at the entry of the evaporator. The valves were assumed to be isenthalpic.

The ammonia mass balance in the generator was considered, given by Eq. (56):

$$\dot{m}_7 X_7 = \dot{m}_8 X_8 + \dot{m}_1 \tag{56}$$

Where X represents the mass fraction of ammonia in the mixture.

The enthalpic gain in the circulation pump is given by Eq. (57):

$$h_6 = h_5 + (P_H - P_L)\,\nu_6 \tag{57}$$

Where P_H represents the high pressure of the heat pump, P_L its low pressure, and ν_6 the fluid's specific volume at the exit of the circulation pump.

The global energy balance of the system is given by Eq. (58):

$$\dot{Q}_g + \dot{Q}_e + \dot{W}_P = \dot{Q}_c + \dot{Q}_a \tag{58}$$

The heat exchanger has been modelled through the logarithmic mean temperature difference (LMTD) method, thus the heat transferred in this component is calculated by Eq. (59):

$$\dot{Q}_{he} = AU\,\Delta T_{ml} \tag{59}$$

Where AU represents the global heat transfer coefficient of the heat exchanger and ΔT_{ml} is obtained by Eq. (60):

$$\Delta T_{ml} = \frac{\Delta T_1 - \Delta T_2}{\ln\left(\frac{\Delta T_1}{\Delta T_2}\right)} \tag{60}$$

With ΔT_1 and ΔT_2 calculated by Eq. (61) and Eq. (62), respectively:

$$\Delta T_1 = T_{hi} - T_{co} \tag{61}$$

$$\Delta T_2 = T_{ho} - T_{ci} \tag{62}$$

With the subscript h representing hot, c cold, i inlet and o outlet.

The coefficient of performance of the heat pump is calculated through Eq. (63):

$$\mathrm{COP} = \frac{\dot{Q}_e}{\dot{Q}_g + \dot{W}_P} \tag{63}$$

3.3.1. Numerical implementation

The heat pump model code is made of a main function and some auxiliary functions. The main function solves for the unknown enthalpy, mass flow rate and mass fraction values using `fsolve`. Note that `fsolve` is more likely to successfully converge when the equations provided have approximately the same order of magnitude. For this reason, the energy balance equations in `fsolve` were divided by a reference value of 2500 and the mass balance equations by a reference value of 0.01.

For the heat exchanger model, the logarithmic mean temperature difference (LMTD) method was used, since preliminary studies showed that the NTU method led to convergence issues when used within `fsolve`, while LMTD was found to improve the robustness of the system.

A MATLAB / REFPROP extension was also used to determine the mass fraction of the weak mixture leaving the generator in function of its pressure and temperature (Wang, 2016).

3.3.2. Model validation

The results from a reference were reproduced with the built model to determine its validity.

An ammonia – water absorption system was considered using the following parameters as inputs: the high and low pressures of the heat pump, the mass flow rate and fraction of the strong mixture, and the generator's temperature. The used values can be seen in Table 5 (Altiokka & Arslan, 2023):

Table 5: Inputs used for the heat pump's validation.

Parameter	Value	Unit
T_g	80	°C
P_H	1167.20	kPa
P_L	534.53	kPa
$\dot{m}_{sm}$	0.0135	kg s^{-1}
X_{sm}	0.5778	-

The obtained heat transfer rates are presented in Table 6, along with the results from the reference article:

Table 6: Heat pump main heat transfer rates.

Component	Present model [kW]	Reference (Altiokka & Arslan, 2023) [kW]
Condenser	4.38	4.45
Evaporator	3.84	3.90
Absorber	5.37	5.14
Generator	5.86	5.68

Based on Table 6, the absorption heat pump model was considered sufficiently reliable.

3.4. Thermal storage

As stated previously, the thermal storage tanks have been each modelled as two similar separate tanks, to account for stratification. Energy balances have thus been applied to each modelled tank, considering the inlet mass flow rate for each tank, the thermal losses to the environment, and the input electric power, which is delivered only to the warmer layer (tank 1). The resulting equations for tank 1 and tank 2 can be seen in Eq. (64) and Eq. (65), respectively:

$$\frac{dT_1}{dt} = \frac{\dot{m}_1(T_{1i} - T_1)}{M_1} - \frac{AU_1(T_1 - T_a)}{M_1\ c} + \dot{W} \tag{64}$$

$$\frac{dT_2}{dt} = \frac{\dot{m}_2(T_{2i} - T_2)}{M_2} - \frac{AU_2(T_2 - T_a)}{M_2\ c} \tag{65}$$

In which $\dot{m}$ represents the mass flow rate, T the temperature, M the mass, AU the tank's heat loss coefficient, c the specific heat capacity at constant pressure and $\dot{W}$ the electric power. The subscript 1 refers to the warmer tank (top layer), while the subscript 2 refers to the cooler tank (bottom layer).

The heat loss coefficient is given by Eq. (66) (Arslan & Kilic, 2021):

$$AU = U_{L,T}\left(2\frac{V}{H} + \pi DH\right) \tag{66}$$

Where $U_{L,T}$ represents the tank's heat loss coefficient (per unit area) , V the volume, H the height and D the diameter.

The storage circuit heat exchangers were modelled according to the effectiveness-NTU method. For the application of this method, the heat capacity ratio must be calculated, which is given by Eq. (67) (Incropera, Dewitt, Bergman, & Lavine, 2007):

$$C_r = \frac{C_{min}}{C_{max}} \tag{67}$$

Where C_{min} and C_{max} correspond, respectively, to the minimum and maximum values between C_h and C_c, which are in turn given by Eq. (68) and Eq. (69), respectively (Incropera, Dewitt, Bergman, & Lavine, 2007):

$$C_h = \dot{m}_h c_h \tag{68}$$

$$C_c = \dot{m}_c c_c \tag{69}$$

With the subscripts h and c representing the fluid in the hot and cold sides of the heat exchanger, respectively.

The number of transfer units is also required, given by Eq. (70) (Incropera, Dewitt, Bergman, & Lavine, 2007):

$$NTU = \frac{UA}{C_{min}} \tag{70}$$

Where UA represents the global heat transfer coefficient of the heat exchanger.

The efficacy of the heat exchanger depends on its type and is a function of the number of transfer units and of the heat capacity ratio. In the present work, a concentric tube type heat exchanger with counterflow was considered, for which the efficacy expression depends on the heat capacity ratio. If $C_r = 1$, the efficacy is given by Eq. (71) (Incropera, Dewitt, Bergman, & Lavine, 2007):

$$\varepsilon = \frac{NTU}{1 + NTU} \tag{71}$$

Otherwise, Eq. (72) is used (Incropera, Dewitt, Bergman, & Lavine, 2007):

$$\varepsilon = \frac{1 - \exp\left(-NTU(1 - C_r)\right)}{1 - C_r \exp\left(-NTU(1 - Cr)\right)} \tag{72}$$

The maximum possible heat transfer rate is calculated through Eq. (73) (Incropera, Dewitt, Bergman, & Lavine, 2007):

$$\dot{Q}_{max} = C_{min}(T_{hi} - T_{ci}) \tag{73}$$

Where the subscript i represents inlet.

The heat transfer rate in the heat exchanger is thus given by Eq. (74) (Incropera, Dewitt, Bergman, & Lavine, 2007):

$$\dot{Q}_{he} = \varepsilon\, \dot{Q}_{max} \tag{74}$$

The outlet temperature of the fluid on the hot side of the heat exchanger is then given by Eq. (75):

$$T_{ho} = T_{hi} - \frac{\dot{Q}_{he}}{\dot{m}_h c_h} \tag{75}$$

While the outlet temperature of the fluid on the cold side of the heat exchanger is given by Eq. (76):

$$T_{co} = T_{ci} + \frac{\dot{Q}_{he}}{\dot{m}_c c_c} \tag{76}$$

Note that since the thermal storage model is built on standard energy balance equations, a model validation was considered unnecessary.

3.4.1. Numerical implementation

The storage model is made of one main function and an auxiliary function for the heat exchanger. In the main function, the derivative equations that illustrate the temperature in each tank with respect to time are written, and `ODE45` is used to solve said derivatives. `ODE45` is a versatile ordinary differential equation solver adequate for most problems.

The heat exchanger was modelled through the epsilon NTU (Number of Transfer Units) method, since this method is adequate for sequential calculations where the outlet temperatures are unknown, and avoids the need for an iterative solving loop.

Temperatures thresholds were assigned to each storage system that define when each storage is able to supply thermal energy and when each of them should activate the auxiliary.

3.5. Solar fraction

The solar fraction of the system was determined through Eq. (77):

$$f = \frac{Q_g + Q_{warm} + Q_{DHW} - E_{lts} - E_{hts}}{Q_g + Q_{warm} + Q_{DHW}} \tag{77}$$

Where Q_g represents the heat supply in the heat pump's generator, Q_{warm} the space heating demand, Q_{DHW} the domestic hot water demand, E_{lts} the electrical energy consumption in the low temperature storage system and E_{hts} the electrical energy consumption in the high temperature storage system. Note that all the terms in Eq. (77) correspond to energy values. In the present work, this equation is applied yearly, monthly, and to sets of 5 days, with the used values being the sum of the energy transferred throughout the entirety of the respective period.

4. Case study

4.1. Location and environmental conditions

The chosen location for the testing is Évora, Portugal (latitude: 38.571; longitude:-7.908).

The typical meteorological year (TMY) was retrieved from the application Photovoltaic Geographical Information System (PVGIS), and it was generated based on 19 years of reanalysis data, between 2005 and 2023, from the European Centre for Medium-Range Weather Forecasts (ECMWF). This reanalysis product is the ERA-5, which provides average hourly values centred at each hour (so for every HH:30).

The data consists in an Excel file with values for the ambient temperature at 2 m, the direct normal irradiance, the diffuse and global irradiances on a horizontal plane, and wind speed at 10 m.

The hourly data was then interpolated into minute wise values using the PCHIP method, and the result was used as an input for the simulations. PCHIP stands for Piecewise Cubic Hermite Interpolating Polynomial and consists in an interpolation method which preserves the shape and monotonicity of the data.

The clearness index was used to identify days with a decrease in solar availability, and is defined as the ratio between the global horizontal surface irradiance and the extraterrestrial irradiance on the horizontal plane. It is thus given by Eq. (78) (Duffie & Beckman, 2013):

$$k_i = \frac{I}{G_0} \tag{78}$$

With G_0 calculated though Eq. (79) (Duffie & Beckman, 2013):

$$G_0 = G_{sc}\left(1 + 0.033\, cos\,\frac{360\ N}{365}\right)\cos\phi \tag{79}$$

Where G_{sc} represents the solar constant, N the day of the year and ϕ the solar zenith angle, which is calculated in Section A of the appendices.

4.2. Cooling and heating demand

The calculation of the cooling demand, Q_{cool}, was done according to the cooling degree-day method, adapted for obtaining the cooling demand for each simulated minute, using Eq. (80) (ASHRAE, 2021):

$$Q_{cool} = AU_{res}\, CDD\, \Delta t \tag{80}$$

In which AU_{res} represents the overall heat loss coefficient of a typical residence, here assumed to be 127.3 W/K (The Open University, s.d.), CDD represents the cooling degree-days and Δt represents the time step, in hours (hence equal to $\frac{1}{60}$). Note that the heat transfer coefficient assumes a residence floor area of 96 m^2.

CDD is calculated through Eq. (81) (ASHRAE, 2021):

$$CDD = \max\left(T_a - T_{c,cool}, 0\right) \tag{81}$$

Where T_a represents the ambient temperature and $T_{c,cool}$ represents the comfort temperature for cooling applications, here assumed to be 25 °C.

The heating demand for each minute, Q_{warm}, was calculated analogously to Q_{cool}, through Eq. (80) using heating degree-days (HDD), calculated through Eq. (82):

$$HDD = \max\left(T_{c,warm} - T_a, 0\right) \tag{82}$$

Where $T_{c,warm}$ represents the comfort temperature for heating applications, here assumed to be 20 °C.

Note that in order to identify days with increased climatization demands and decreased solar availability, the average daily climatization demands were divided by the clearness index.

4.3. Hot water demand

The determination of the domestic hot water (DHW) demand was based on a method used to calculate the consumption profile in multi-family buildings. This method provides Eq. (83), which estimates the base value for the daily volume of required DHW in function of the floor area and number of rooms considered per house (Chmielewska, 2025):

$$V_d = 0.0021\,A_1 + 0.0018\,A_2 + 0.0017\,A_3 + 0.0011\,A_4 + 0.011 \tag{83}$$

Where A represents the total floor area and the subscripts represent the number of rooms each floor area is associated with. The total floor area considered in the present work is 96 m^2 (The Open University, s.d.), and it was assumed that this area corresponds to a three-room house, thus Eq. (83) takes on a simplified form:

$$V_d = 0.0017\,A_3 + 0.011 \tag{84}$$

The resulting base DHW volume requirement is thus 0.1742 m^3 per day, to which monthly and hourly correction factors were then applied to develop the consumption profile. Although Chmielewska also applies daily correction factors (by day of the week), these were considered irrelevant in the present work due to the characteristics of a typical meteorological year.

The final volumetric DHW requirement per time step is thus given by Eq. (85):

$$V_m = s_m\,s_h\,V_d\,t \tag{85}$$

Where s_m and $s_h$represent the monthly and hourly correction factors, respectively, and t the time step ($\frac{1}{60}$).

The considered monthly correction factors can be seen in Table 7 (Chmielewska, 2025):

Table 7: Monthly correction factors used for the determination of the DHW demand.

Month	1	2	3	4	5	6	7	8	9	10	11	12
s_m	1.10	1.09	1.11	1.07	1.01	0.92	0.88	0.77	0.93	1.00	1.04	1.07

Since Chmielewska provides distinct hourly correction factors for working days and weekends, a weighted average was calculated and applied to all days. These values can be seen in Table 8:

Table 8: Hourly correction factors used for the determination of the DHW demand.

Hour	s_h			Hour	s_h		
	Working days	Weekends	Weighted average		Working days	Weekends	Weighted average
1	0.027	0.030	0.028	13	0.025	0.051	0.032
2	0.009	0.014	0.010	14	0.023	0.045	0.029
3	0.004	0.006	0.005	15	0.024	0.041	0.029
4	0.003	0.004	0.003	16	0.025	0.037	0.028
5	0.005	0.004	0.005	17	0.031	0.035	0.032
6	0.027	0.004	0.020	18	0.038	0.036	0.037
7	0.083	0.011	0.062	19	0.054	0.050	0.053
8	0.068	0.030	0.057	20	0.084	0.077	0.082
9	0.047	0.058	0.050	21	0.086	0.075	0.083
10	0.040	0.073	0.049	22	0.089	0.066	0.082
11	0.033	0.076	0.045	23	0.086	0.067	0.081
12	0.029	0.062	0.038	24	0.059	0.050	0.056

The energy corresponding to the domestic hot water demand is given by Eq. (86):

$$Q_{DHW} = \rho\, V_m\, c\, (T_{DHW} - T_G) \tag{86}$$

Where ρ represents water's density, c water's specific heat capacity at constant pressure, T_{DHW} the temperature of the delivered hot water, and T_G the undisturbed ground temperature, considered to correspond to the initial temperature of the water coming from the distribution network. Average values of 50°C and 15°C were considered for T_{DHW} and T_G, respectively.

4.4. System design and operating conditions

4.4.1. Solar collectors

The dimensions of the evacuated tubes solar collectors can be seen in Table 9 (for radial components) and Table 10 (for planar components). These are assumed to be representative values for this type of technology and have been defined after a review of the literature and manufacturer datasheets.

Table 9: Dimensions of the solar collector – radial components.

<table>
<tr><th colspan="3">Component</th><th>Outer diameter [cm]</th><th>Thickness [mm]</th><th>Length [cm]</th></tr>
<tr><td rowspan="6">Evacuated tube</td><td rowspan="2">Glass tube</td><td>Glass cover</td><td>5.8</td><td>2.2</td><td rowspan="5">160</td></tr>
<tr><td>Absorber</td><td>4.7</td><td>1.6</td></tr>
<tr><td rowspan="2">Fin</td><td>Outer fin</td><td>4.38</td><td rowspan="2">2</td></tr>
<tr><td>Inner fin</td><td>1.2</td></tr>
<tr><td rowspan="2">Heat pipe</td><td>Evaporator</td><td>0.8</td><td>0.6</td></tr>
<tr><td>Condenser</td><td>2.4</td><td>1</td><td rowspan="2">2.9 [1]</td></tr>
<tr><td rowspan="4">Manifold</td><td colspan="2">Condenser tube</td><td>2.6</td><td>1</td></tr>
<tr><td colspan="2">Main tube</td><td>3.8</td><td>2</td><td rowspan="3">7.5 [2]</td></tr>
<tr><td colspan="2">Isolation</td><td>14.2</td><td>52</td></tr>
<tr><td colspan="2">Outer casing</td><td>14.6</td><td>2</td></tr>
</table>

Table 10: Dimensions of the solar collector – planar components.

Component			Length [m]	Width [mm]	Thickness [cm]
Evacuated tube	Fin	Fin bridge	1.6	2	1.588

Each collector was assumed to have 20 evacuated tubes, resulting in a total manifold length of 1.5 m. Table 11 was thus obtained with each solar collector's bulk, aperture and absorber area, calculated according to (ISO, 1999). Note that the gross area is considered an approximation, since it depends on connective elements that were not considered in the present work:

Table 11: Solar collector areas.

Gross area [m^2]	2.619
Aperture area [m^2]	1.7152

[1] The condenser tube length considered is the length of the equivalent cylinder used to calculate the heat transfer between the condenser tube and the working fluid in the manifold's main pipe.

[2] The manifold length considered is the length of one single section including one evacuated tube and the space between two tubes.

Absorber area [m^2]	1.504

The properties of each component of the collectors can be seen in Table 12, along with each corresponding reference:

Table 12: Properties of the solar collector.

<table>
<tr><th colspan="3">Component</th><th>Material</th><th>Property</th><th>Value</th><th>Unit</th><th>Reference</th></tr>
<tr><td rowspan="9">Evacuated tube</td><td rowspan="6">Glass tube</td><td rowspan="3">Glass cover</td><td rowspan="3">Borosilicate glass</td><td>Emissivity</td><td>0.88</td><td>-</td><td>(Kalogirou, 2024)</td></tr>
<tr><td>Thermal conductivity</td><td>1.2</td><td>$W\ m^{-1} K^{-1}$</td><td>(SGL, s.d.)</td></tr>
<tr><td>Transmissivity</td><td>0.9</td><td>-</td><td>(Zambolin & Col, 2012)</td></tr>
<tr><td rowspan="3">Absorber</td><td rowspan="3">Borosilicate glass with absorptive coating</td><td>Emissivity</td><td>0.05</td><td>-</td><td>(Kingspan Environmental Ltd)</td></tr>
<tr><td>Thermal conductivity</td><td>1.2</td><td>$W\ m^{-1} K^{-1}$</td><td>(SGL, s.d.)</td></tr>
<tr><td>Absorptivity</td><td>0.93</td><td>-</td><td>(Zambolin & Col, 2012)</td></tr>
<tr><td rowspan="2" colspan="2">Fin</td><td rowspan="5">Copper</td><td>Emissivity</td><td>0.65</td><td>-</td><td>(TRANSMETRA, s.d.)</td></tr>
<tr><td rowspan="4">Thermal conductivity</td><td rowspan="4">385.0</td><td rowspan="4">$W\ m^{-1} K^{-1}$</td><td rowspan="4">(Georgia State University, s.d.)</td></tr>
<tr><td colspan="2">Heat pipe</td></tr>
<tr><td rowspan="5">Manifold</td><td colspan="2">Condenser tube</td></tr>
<tr><td colspan="2">Main tube</td></tr>
<tr><td colspan="2">Isolation</td><td>Rock wool</td><td>Thermal conductivity</td><td>0.04</td><td>$W\ m^{-1} K^{-1}$</td><td>(Georgia State University, s.d.)</td></tr>
<tr><td rowspan="2" colspan="2">Outer casing</td><td rowspan="2">Aluminium</td><td>Emissivity</td><td>0.11</td><td>-</td><td>(TRANSMETRA, s.d.)</td></tr>
<tr><td>Thermal conductivity</td><td>205.0</td><td>$W\ m^{-1} K^{-1}$</td><td>(Georgia State University, s.d.)</td></tr>
</table>

Note that for obtaining the emissivity of copper and aluminium, oxidized surfaces were assumed, considering that these are most representative of real operating conditions.

4.4.2. Absorption heat pump

The chosen mixture was ammonia and water (NH_3–H_2O).

The condenser and absorber were considered to be cooled by cooling towers supplied with water from the distribution grid.

The heat exchanger was dimensioned so it presented a UA value of 97.78 W/K.

The working conditions initially used can be seen in Table 13:

Table 13: Heat pump's initial operating conditions.

Parameter	Value	Unit
T_g	80	°C
P_H	1167	kPa
P_L	590	kPa
$\dot{m}_{sm}$	0.0145	kg s^{-1}
X_{sm}	0.5150	-

The heat pump model was then dimensioned according to the maximum cooling demand determined in Section 5.2, with the corresponding analysis present on Section 5.3.

4.4.3. Thermal storage

Each tank's initial mass (m_t), diameter (D_t), height (h_t), area (A_t) heat loss coefficient per unit area (U_t) and global heat loss coefficient *(AU_t)* can be seen in Table 14:

Table 14: Characteristics of the thermal storage tanks.

Parameter	Value	Unit
m_t	200	kg
D_t	45.0	cm
h_t	1.36	m
A_t	2.24	m^2
U_t (Arslan & Kilic, 2021)	0.6	W m^{-2} K^{-1}
AU_t	1.34	W K^{-1}

Note that the values in Table 14 correspond to the values of one single modelled tank, resulting in a total mass of 400 kg for each of the high and low temperature storage systems.

The heat exchangers were dimensioned so that their UA values result in 800 W K^{-1}.

For the high temperature storage system, an electric power of 5 kW was considered for the auxiliary heating system, which is activated whenever this storage reached below 358 K, and a minimum operating temperature of 353 K was used, above which the storage is able to supply the heat pump.

For the low temperature storage system, an electric power was considered with a temperature threshold of 318 K, and a minimum temperature requirement of 313 K for the storage to cover any heating demand. During the cooling season, this storage is only charged when the high temperature storage is above 375 K.

4.5. Global operating conditions

A maximum mass flow rate of 1 kg s^{-1} was considered in the collector and in the thermal storage circuits. A pressure of 250 kPa was considered in the circuits (approximately two and a half atmospheres), corresponding to a saturation temperature of 127.41 °C. Thus, a maximum temperature of 120 °C was imposed for the whole system.

A total of 5 collectors were initially used in the system. These were oriented towards the south and with an inclination of 45°.

4.6. Parametric analysis setup

In order to obtain an optimized version of the system, an analysis was conducted to study the impact of some of the main system design parameters. The chosen parameters were the number of collectors, as well as their maximum mass flow rate and tilt, and the mass of both the storage systems.

The number of collectors was varied from 1 to 10, the maximum flow rate between 0.25 and 2 kg s^{-1}, the tile of the collector between 20 and 50 °, and the mass of the storage tanks between 100 and 300 kg.

Note that the variation of the tanks' mass impacts not only the capacity of the storage, but its area and therefore heat losses. The different values assumed for the mass and respective diameter, height, area and global heat loss coefficient can be seen in Table 15. The heat loss coefficient per unit area was considered to remain constant.

Table 15: Storage tanks mass, dimensions and heat loss coefficient values.

m_t [kg]	100	150	200	250	300

D_t [cm]	36.0	36.0	45.0	48.0	48.0
h_t [m]	1.076	1.460	1.360	1.450	1.710
A_t [m^2]	1.421	1.855	2.241	2.548	2.941
AU_t [$W\ K^{-1}$]	0.852	1.113	1.344	1.529	1.764

5. Results

5.1. Environmental conditions

The yearly global horizontal irradiation for Évora was calculated and determined to be 1805 kWh m^{-2} $year^{-1}$.

Representative days were identified and five-day periods were constructed around them, as a way to mitigate the effects of the initial values used, as well as study the response of the system after the identified days.

The first representative day identified was the one corresponding to the warmest day of the year - 18th of July. In this day, a maximum hourly average temperature of 38.11 °C was reached at 16 h UTC. The direct normal irradiance (I_{BN}), diffuse horizontal irradiance (I_{DH}), global horizontal irradiance (I_{GH}) and ambient temperature (T_a) for the 18th of July period are represented in Figure 24:

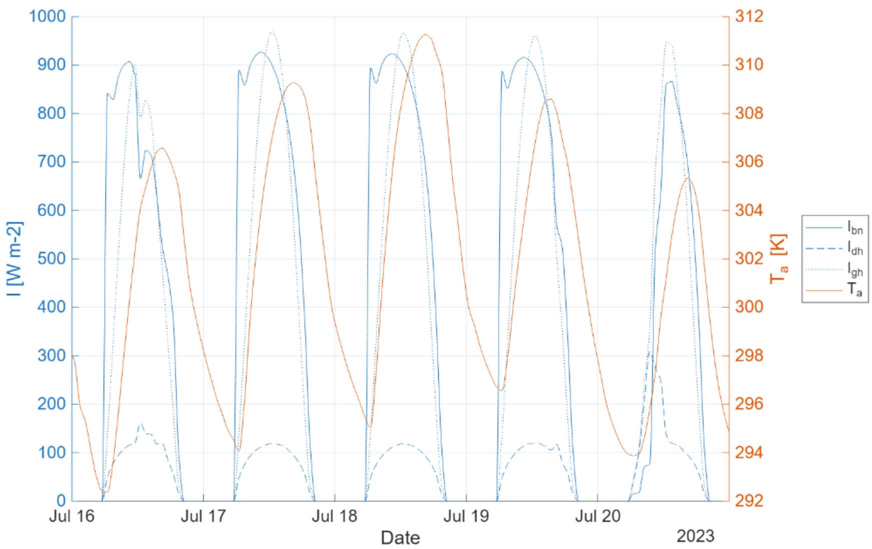

Figure 24: Environmental conditions during the 18th of July period.

The day with the highest cooling demand to clearness index factor was also found to be the 18th of July, with an average clearness index of 0.72.

The coldest day was identified as being the 12th of January, when a minimum hourly average temperature of 2.40 °C was reached at 8 h, and its environmental conditions be seen in Figure 25:

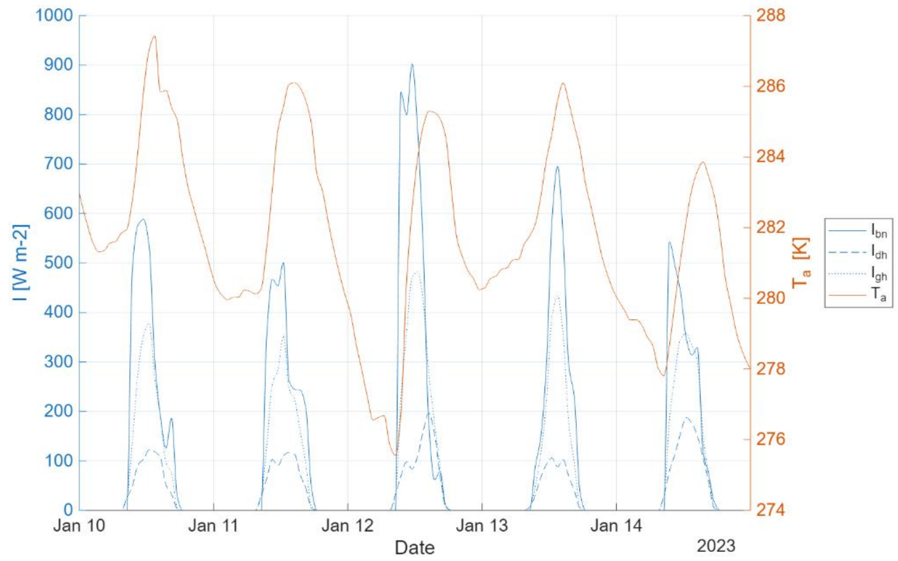

Figure 25: Environmental conditions during the 12th of January period.

The day with the highest heating demand to clearness index factor was found to be the 9th of January, with a daily average temperature of 7.64 °C and an average clearness index of 0.10, and the corresponding irradiances and ambient temperature represented in Figure 26:

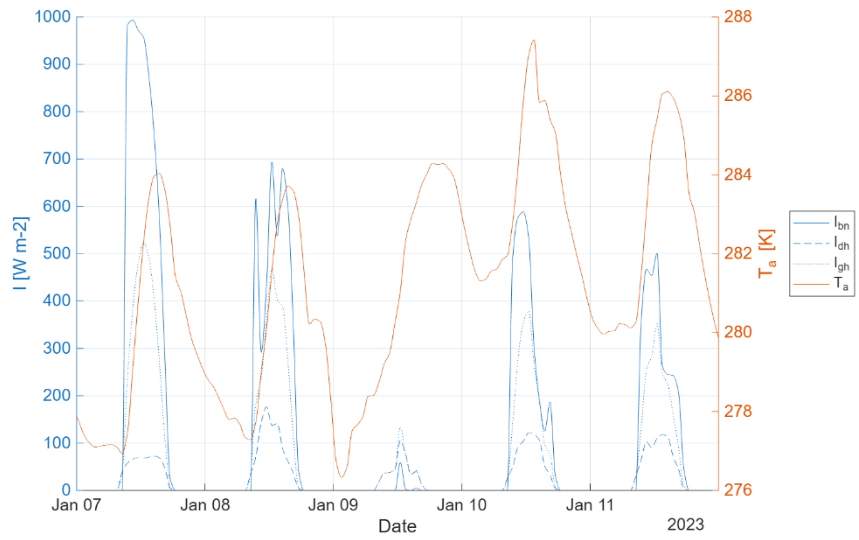

Figure 26: Environmental conditions during the 9th of January period.

Table 16 was also built, with the monthly average ambient temperatures and clearness indexes:

Table 16: Monthly average ambient temperature and clearness index.

Month	T_a	k_i
1	9.66	0.52
2	13.23	0.58
3	12.02	0.55
4	15.73	0.55
5	18.45	0.66
6	22.72	0.68
7	23.83	0.69
8	23.51	0.69
9	22.55	0.71
10	16.61	0.57
11	14.11	0.48
12	12.81	0.51

5.2. Climatization demand

The total cooling and heating demand for each month were calculated with the intent of determining the cooling season for control purposes. The resulting plot can be seen in Figure 27:

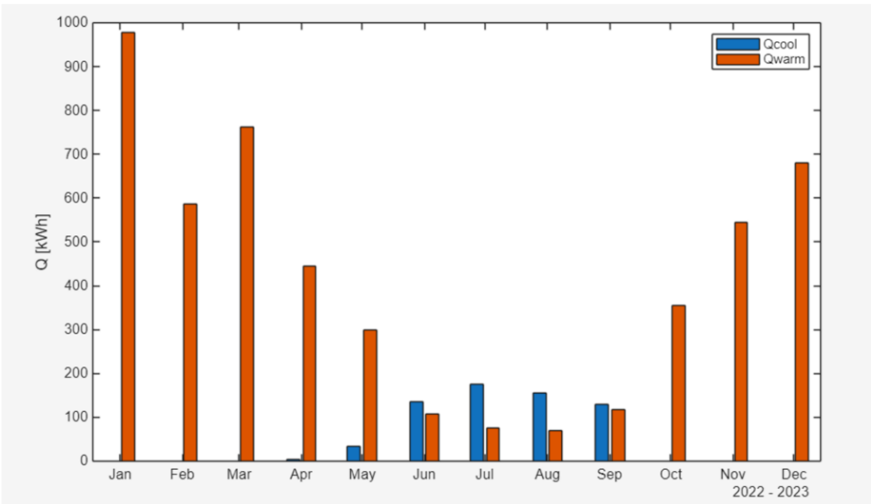

Figure 27: Climatization demand for each month in kWh.

The maximum cooling demand throughout the year was determined to be 1.67 kW, corresponding to the 18th of July.

5.3. Analysis of heat pump operation

Since the absorption heat pump model exhibits a high sensitivity to the input values, an initial parametric analysis was conducted to identify stable operation points as well as an optimized design in function of the calculated cooling demand. This analysis consisted in the variation of the high and low pressures in the heat pump, of the generator temperature, and of the flow rate and mass fraction corresponding to the strong mixture.

For each variation, the effects in component temperatures, heat transfer rates and the COP were observed, as well as the `exitflag` returned from `fsolve`, which indicates whether or not the problem was effectively solved. The used ranges for each variation were built around points with an `exitflag` of (at least) 1. Note that tables resulting from this analysis are present in Section C of the appendices, which all include the heat transfer in the evaporator and in the generator and the `exitflag`.

The effect of the high pressure on the condenser's saturation temperature and on the heat pump's coefficient of performance is illustrated in Figure 28:

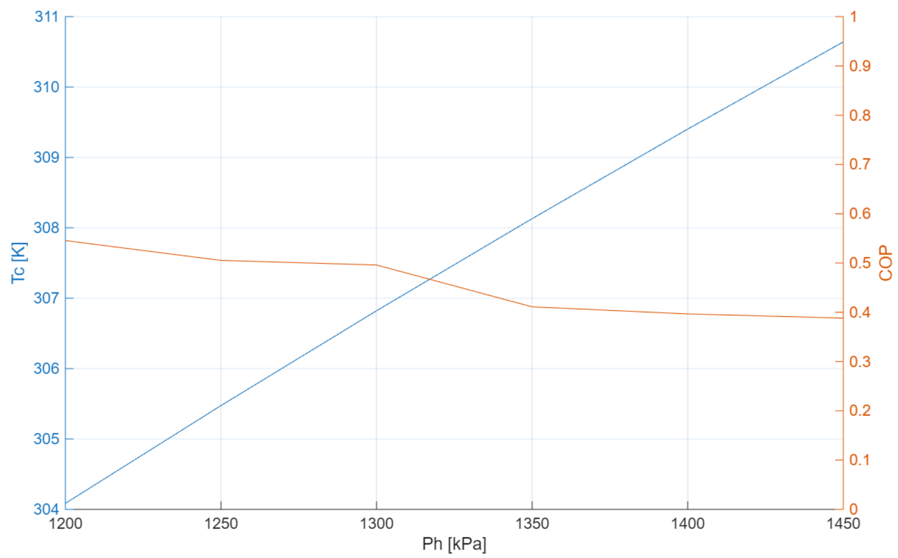

Figure 28: Condenser temperature and COP in function of the high pressure.

The high pressure was adjusted based on the saturation temperature of the condenser. Since the condenser is assumed to be cooled by cooling towers in this case, it is able to remain at relatively low temperatures, and a low value of 1200 kPa was chosen for the high pressure in order to achieve a higher coefficient of performance.

The temperature in the evaporator and the heat pump's coefficient of performance in function of the low pressure are represented in Figure 29:

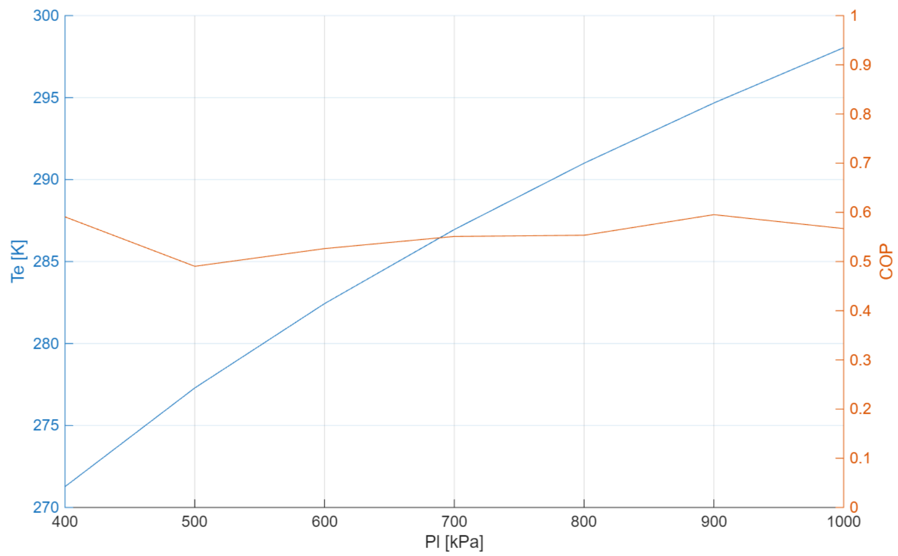

Figure 29: Evaporator temperature and COP in function of the low pressure.

The low pressure was adjusted based on the saturation temperature in the evaporator. An intermediate value of 700 kPa was chosen for the low pressure, in order to obtain a minimum cooling temperature of approximately 14 °C.

The coefficient of performance in function of the generator temperature is represented in Figure 30:

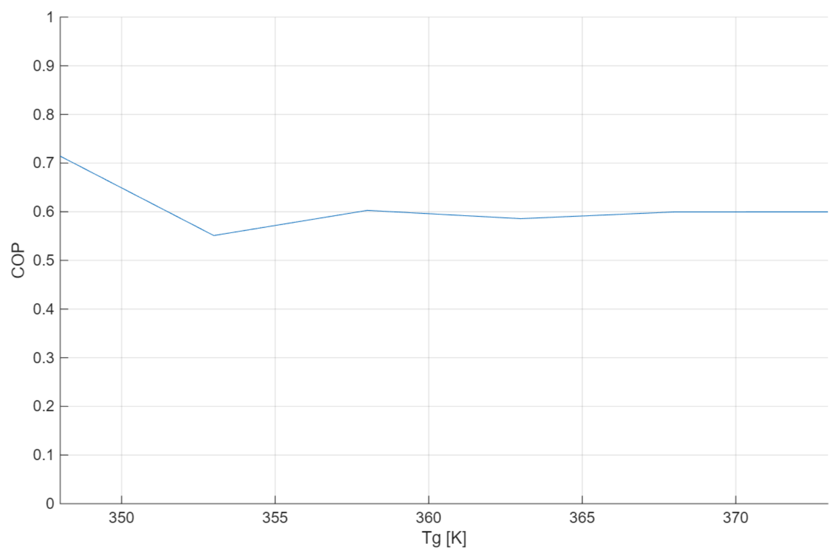

Figure 30: COP in function of the generator temperature.

From Figure 30, no conclusions can be drawn from the relationship between the generator temperature and the coefficient of performance. Although the heat pump's coefficient of performance generally increases with an increase in the generator temperature, later testing revealed that the system's solar fraction decreased in this scenario. For these reasons, the generator temperature was maintained at 353 K.

The heat transfer rate in the evaporator and the coefficient of performance in function of the strong mixture mass flow rate are represented in Figure 31:

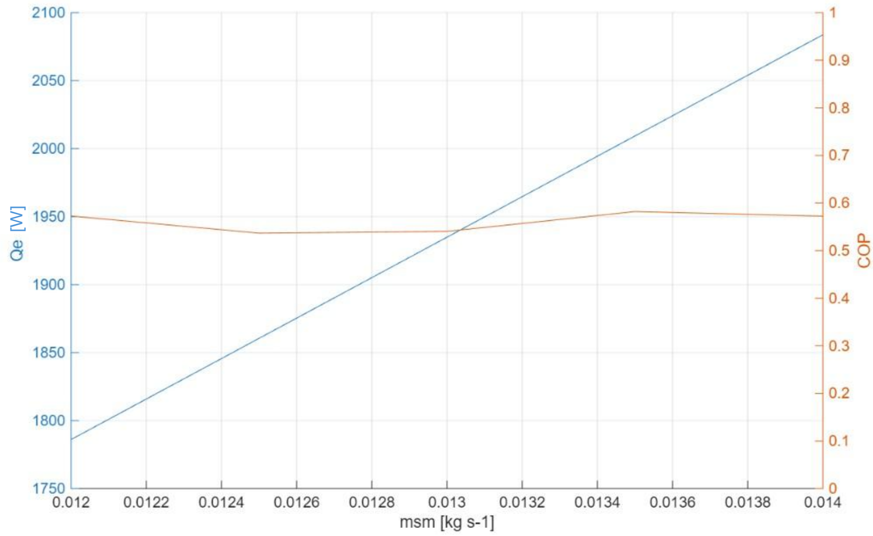

Figure 31: Evaporator heat transfer rate and COP in function of the strong mixture mass flow rate.

The strong mixture flow rate was adjusted based on the desired evaporator heat transfer rate, thus a value of 0.0125 kg s^{-1} was selected.

And the heat transfer rate in the evaporator and coefficient of performance in function of the strong mixture fraction are represented in Figure 32:

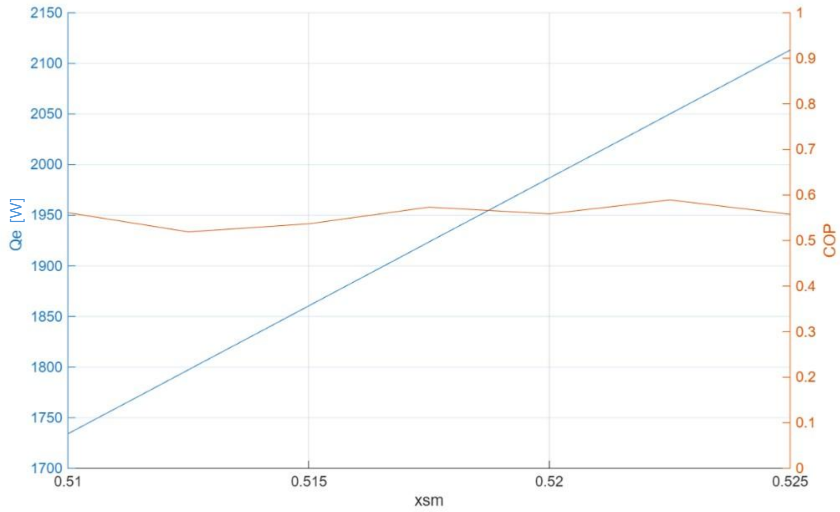

Figure 32: Evaporator heat transfer rate and COP in function of the strong mixture fraction.

The strong mixture fraction was adjusted based on the desired cooling power of the heat pump, thus a value of 0.515 was chosen. The final generator outlet temperature (T_g), high and low pressures in the heat pump (P_H and P_L), and the strong mixture mass flow rate and mass fraction ($\dot{m}_{sm}$ and X_{sm}) are presented in Table 17:

Table 17: Inputs for the absorption heat pump.

Parameter	Value	Unit
T_g	353	K
P_H	1200	kPa
P_L	700	kPa
$\dot{m}_{sm}$	0.0125	kg s^{-1}
X_{sm}	0.515	-

While the obtained evaporator and generator heat transfer rates ($\dot{Q}_e$ and $\dot{Q}_g$), evaporator and condenser temperatures (T_e and T_c) and COP can be seen in Table 18:

Table 18: Main outputs of the absorption heat pump.

Parameter	Value	Unit
$\dot{Q}_e$	1.861	kW
$\dot{Q}_g$	3.459	kW
T_e	286.95	K

T_c	304.09	K
COP	0.537	-

Note that the heat pump's cooling capacity was over dimensioned by approximately 10%.

5.4. Simulation results – base case

5.4.1. High ambient temperature case - 18th of July

The useful heat produced by the collectors (Q_u), the heat transferred from the collectors to the low temperature storage (Q_{clts}), the heat transferred from the collectors to the generator (Q_{cg}) and the heat transferred from the collectors to the high temperature storage (Q_{chts}) are represented in Figure 33:

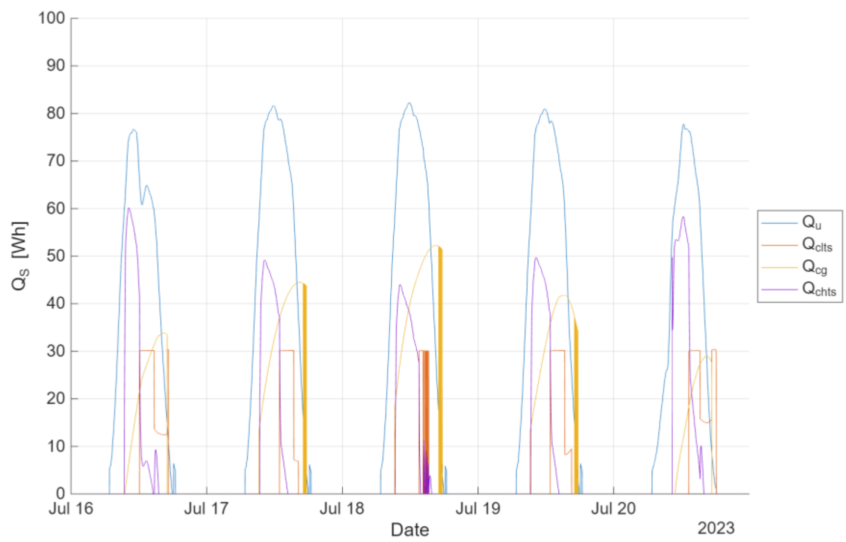

Figure 33: Main heat transfers in the collector circuit during the 18th of July period.

Note that the year displayed in the plots results from the datetime data type and holds no meaning in the present analysis.

The irradiance absorber area product (IA), the useful power produced by the collectors (Q_u), the heat loss through the glass ($Q_{l,ga}$), and the heat loss through the manifold ($Q_{l,ma}$) are represented in Figure 34:

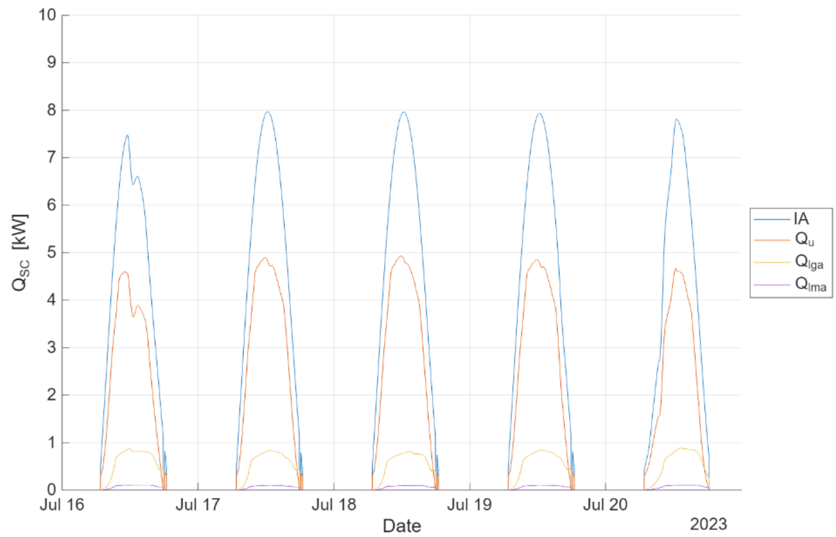

Figure 34: Main heat transfer rates in the solar collectors during the 18th of July period.

The heat transfer in the condenser (Q_c), in the evaporator (Q_e), in the absorber (Q_a), from the collector to the generator (Q_{cg}), from the storage tank to the generator (Q_{tg}), and the cooling demand (Q_{cool}) are represented in Figure 35:

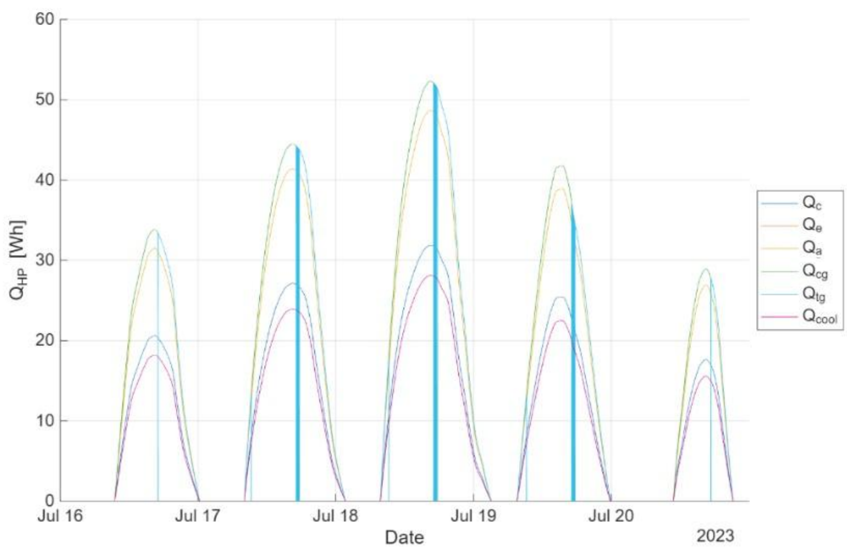

Figure 35: Main heat transfers in the heat pump during the 18th of July period.

The heat transfer between the collector and the high temperature storage circuit (Q_{heht}), the heat transfer between the storage circuit and the generator (Q_{tg}), and the consumed electrical energy in the high temperature storage (E_{ht}) are represented in Figure 36:

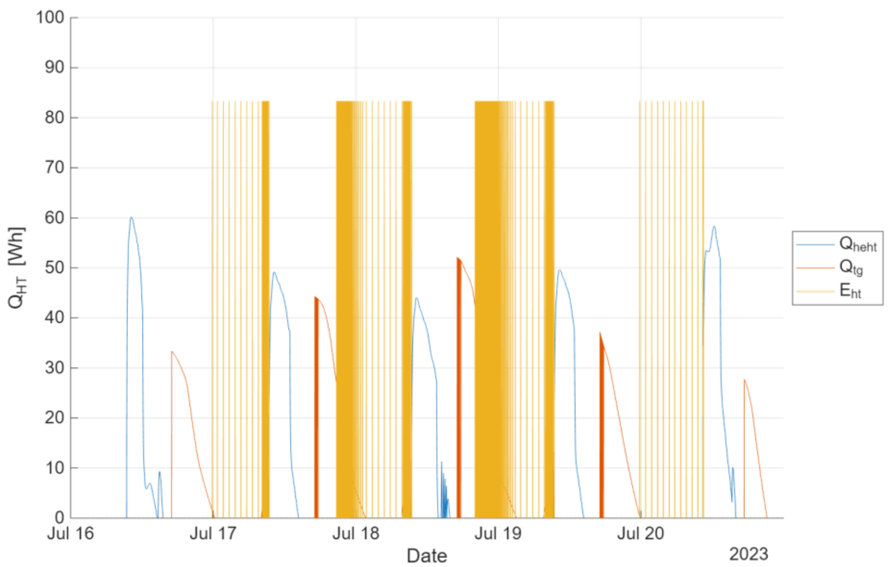

Figure 36: Main heat transfers in the high temperature storage circuit during the 18th of July period.

The heat transfer between the collector and the low temperature storage circuit (Q_{helt}), the space heating demand (Q_{warm}), the domestic hot water demand (Q_{dhw}), and the consumed electrical energy in the low temperature storage (E_{ht}) are represented in Figure 37:

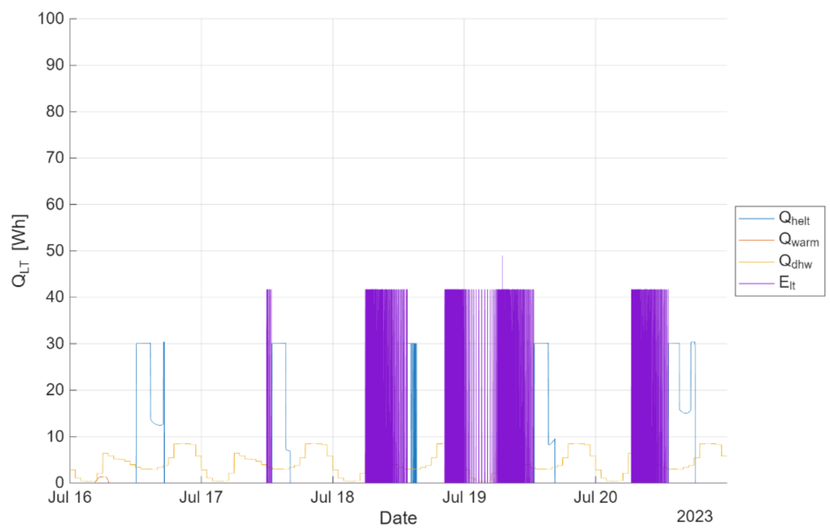

Figure 37: Main heat transfers in the low temperature storage circuit during the 18th of July period.

The ambient temperature (T_a), the collector outlet temperature (T_{fo}), the temperature in the warmer tank in the low temperature storage circuit (T_{lt1}) and the temperature in the warmer tank in the high temperature storage circuit (T_{ht1}) are represented in Figure 38:

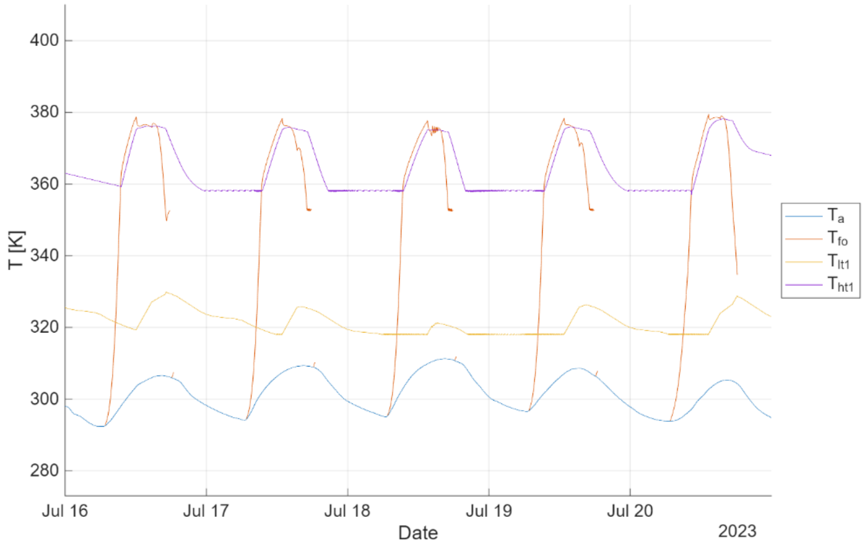

Figure 38: Main temperatures in the system during the 18th of July period.

The heat pump's duty cycle (DC) is represented in Figure 39:

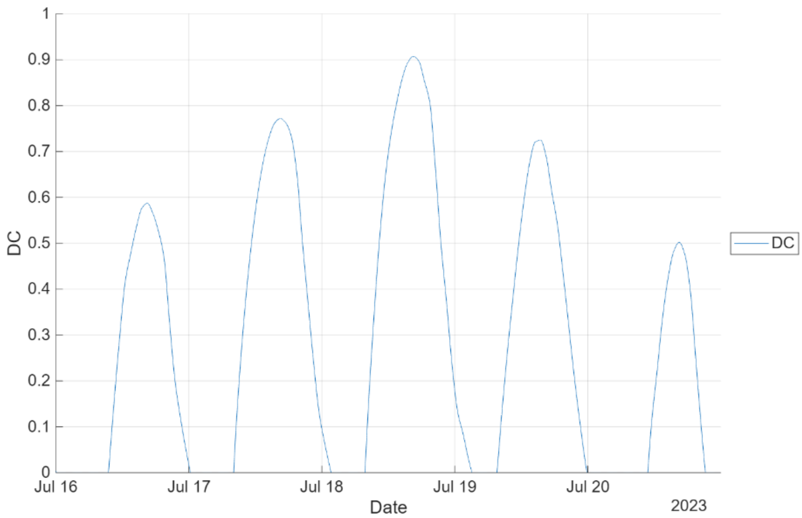

Figure 39: Duty cycle of the heat pump during the 18th of July period.

The solar collectors' efficiency (η), the heat pump's coefficient of performance (COP), and the system's solar fraction (f), are represented in Figure 40. The solar fraction represented is the accumulated solar fraction starting from the beginning of the current analysis.

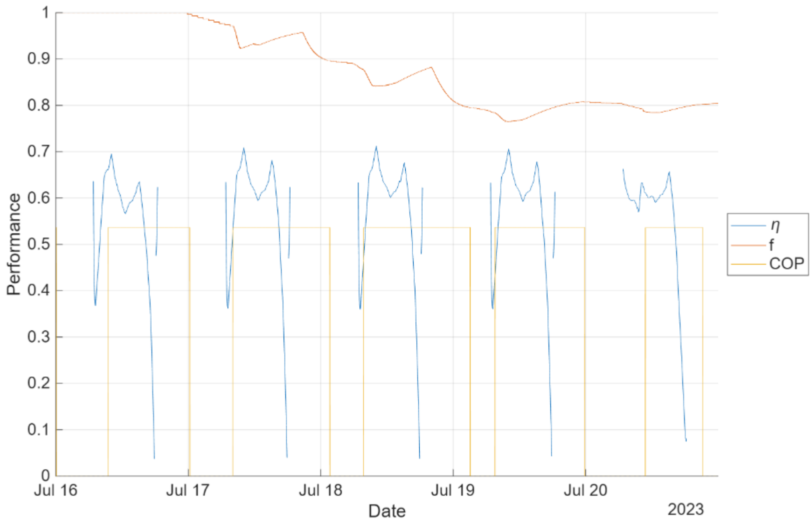

Figure 40: System performance during the 18th of July period.

Note that an alternative configuration of the system was tested, in which the condenser of the heat pump was cooled by the low temperature storage system, such that the heat released in this component could be utilized to supply any heating demand. However, it was concluded that during the warmest periods, there is not enough space heating or domestic hot water demand such that the use of the condenser heat becomes viable. This analysis is illustrated in Figure 41, where the accumulated condenser transferred heat (Q_c) and the accumulated heating demand (space and hot water - $Q_{warm} + Q_{dhw}$) are represented:

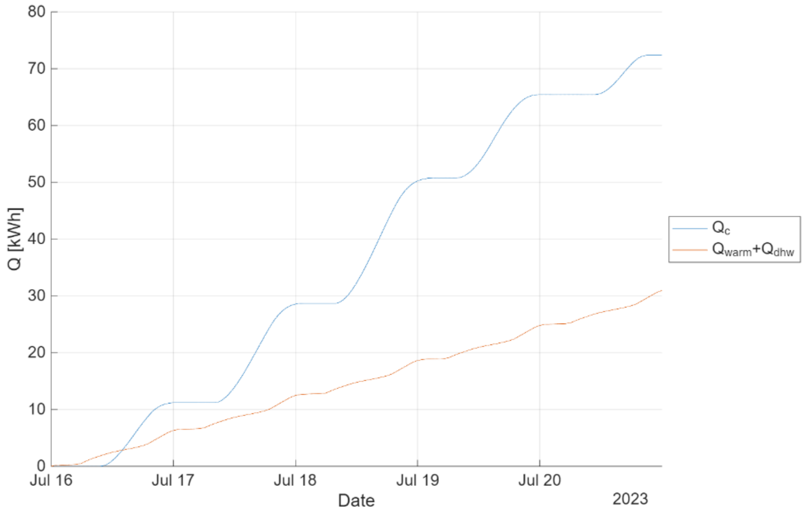

Figure 41: Accumulated condenser heat and heating demand during the 18th of July period.

From Figure 41 we may conclude that during the analysed period the temperature in the low temperature storage system would rise steadily, hereby losing the ability to remove heat from the condenser.

The connection between the condenser and the low temperature storage system also resulted in a higher condenser temperature so that it was possible for this component to cool down using a heat sink at a higher temperature. This resulted in a lower coefficient of performance for the heat pump, accordingly to what is observed in Figure 28.

5.4.2. Low ambient temperature case - 12th of January

The useful heat produced by the collectors (Q_u) and the heat transferred from the collectors to the low temperature storage (Q_{clts}) are represented in Figure 42:

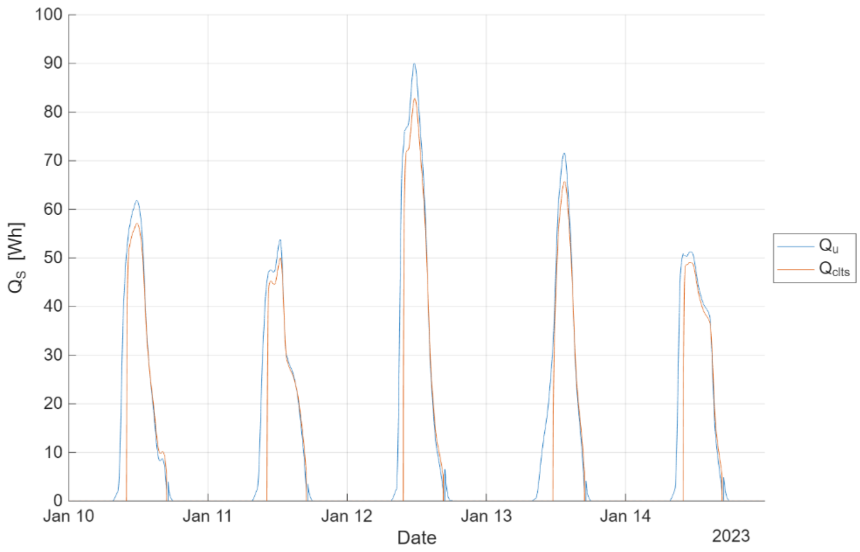

Figure 42: Main heat transfers in the collector circuit during the 12th of January period.

The irradiance absorber area product (IA), the useful power produced by the collectors (Q_u), the heat loss through the glass ($Q_{l,ga}$), and the heat loss through the manifold ($Q_{l,ma}$) are represented in Figure 43:

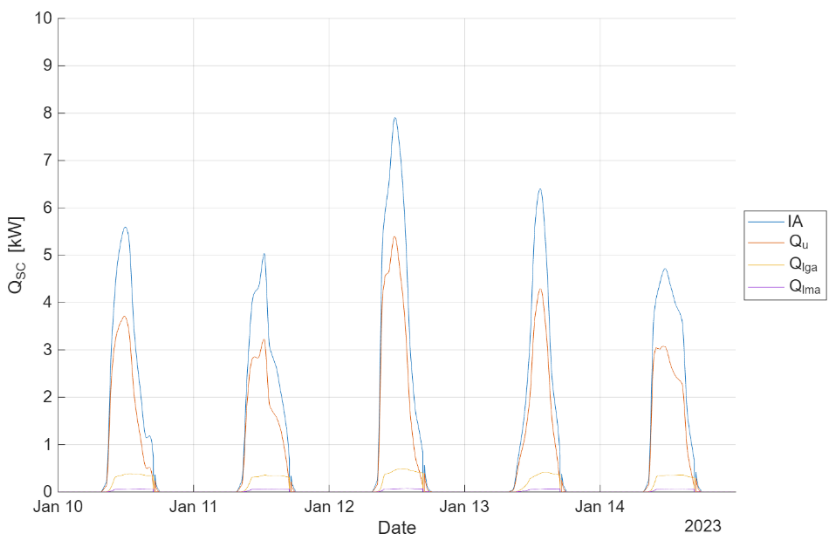

Figure 43: Main heat transfer rates in the solar collector during the 12th of January period.

The heat transfer between the collector and the low temperature storage circuit (Q_{helt}), the space heating demand (Q_{warm}), the domestic hot water demand (Q_{dhw}), and the consumed electrical energy in the low temperature storage (E_{lt}) are represented in Figure 44:

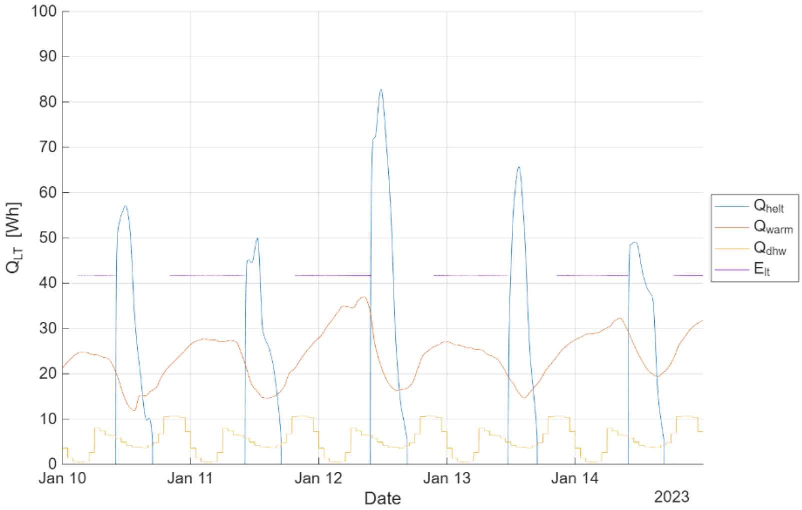

Figure 44: Main heat transfers in the low temperature storage circuit during the 12th of January period.

Note that in Figure 44 and Figure 49, auxiliary energy zero values were replaced with NaN (not a number) for visualization purposes. This avoids large coloured regions in said figures that appear due to a frequent on and off behaviour of the auxiliary systems.

The ambient temperature (T_a), the collector outlet temperature (T_{fo}) and the temperature in the warmer tank in the low temperature storage circuit (T_{lt1}) are represented in Figure 45:

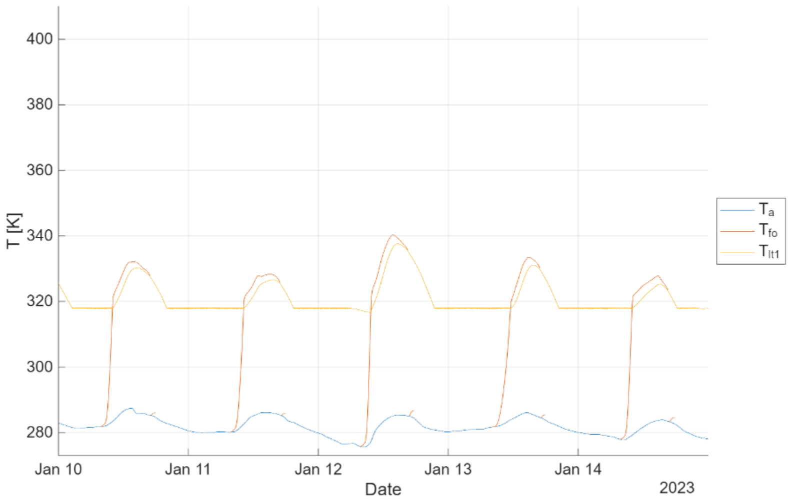

Figure 45: Main temperatures in the system during the 12th of January period.

The solar collectors' efficiency (η) and the system's solar fraction (f), are represented in Figure 46:

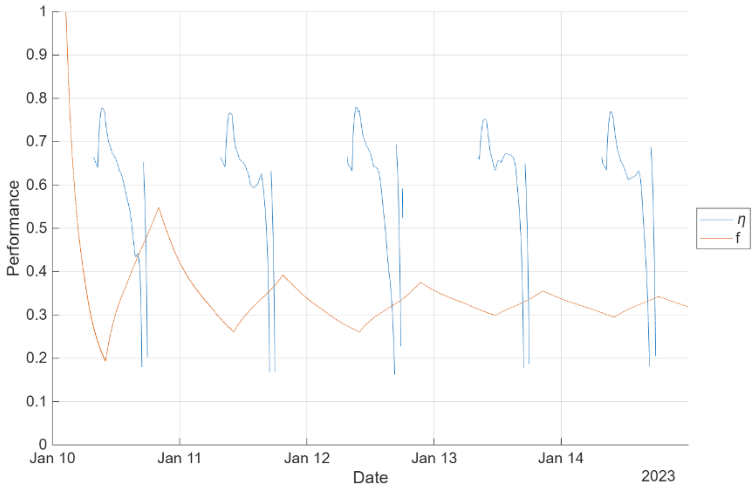

Figure 46: System performance during the 12th of January period.

5.4.3. Low ambient temperature with decreased solar availability - 9th of January

The useful heat produced by the collectors (Q_u) and the heat transferred from the collectors to the low temperature storage (Q_{clts}) are represented in Figure 47:

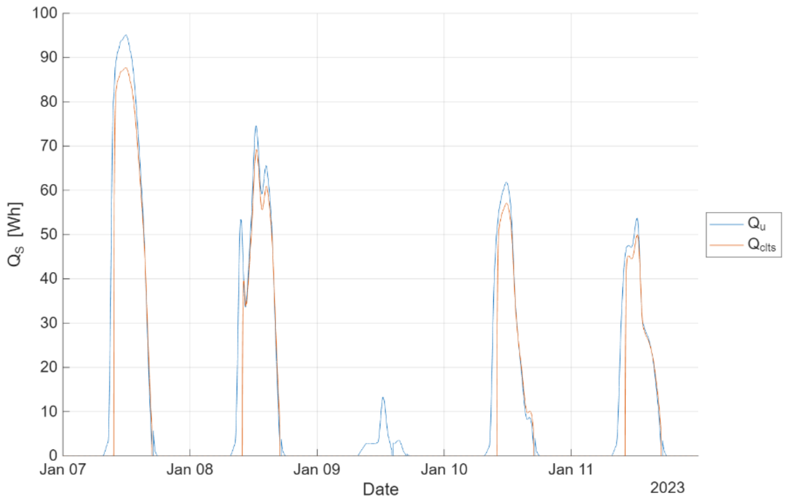

Figure 47: Main heat transfers in the collector circuit during the 9th of January period.

The irradiance absorber area product (IA), the useful power produced by the collectors (Q_u), the heat loss through the glass ($Q_{l,ga}$), and the heat loss through the manifold ($Q_{l,ma}$) are represented in Figure 48:

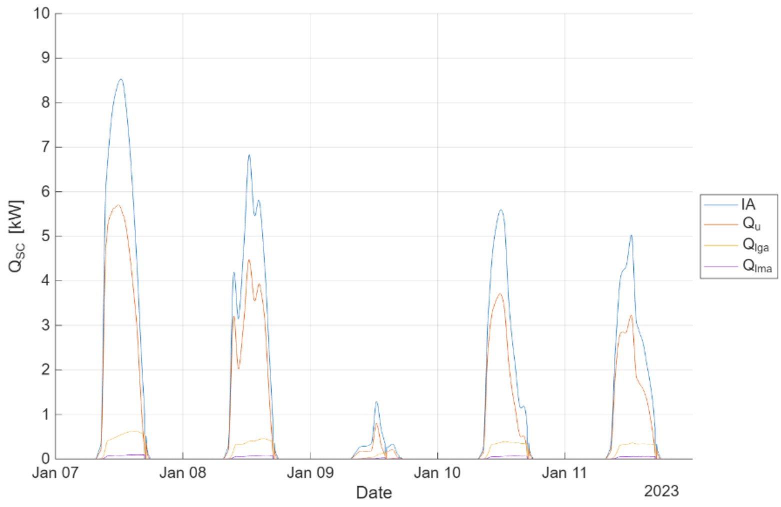

Figure 48: Main heat transfer rates in the solar collector during the 9th of January period.

The heat transfer between the collector and the low temperature storage circuit (Q_{helt}), the space heating demand (Q_{warm}), the domestic hot water demand (Q_{dhw}), and the consumed electrical energy in the low temperature storage (E_{ht}) are represented in Figure 49:

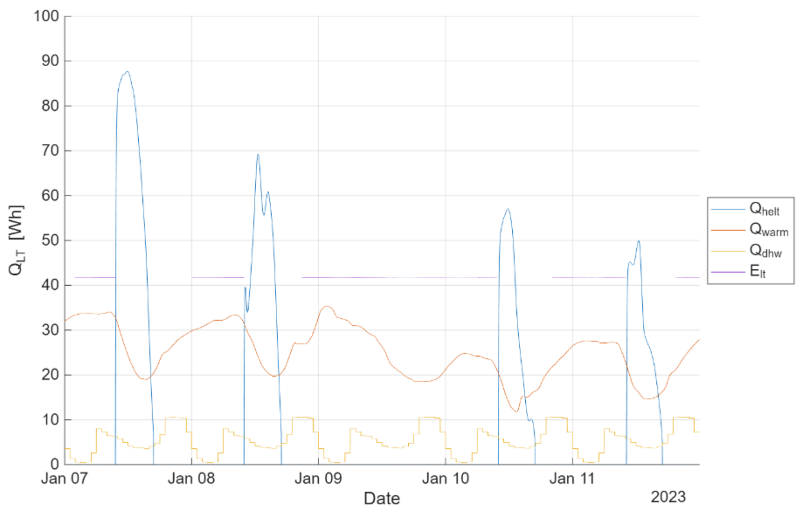

Figure 49: Main heat transfers in the low temperature storage circuit during the 9th of January period.

The ambient temperature (T_a), the collector outlet temperature (T_{fo}) and the temperature in the warmer tank in the low temperature storage circuit (T_{lt1}) are represented in Figure 50:

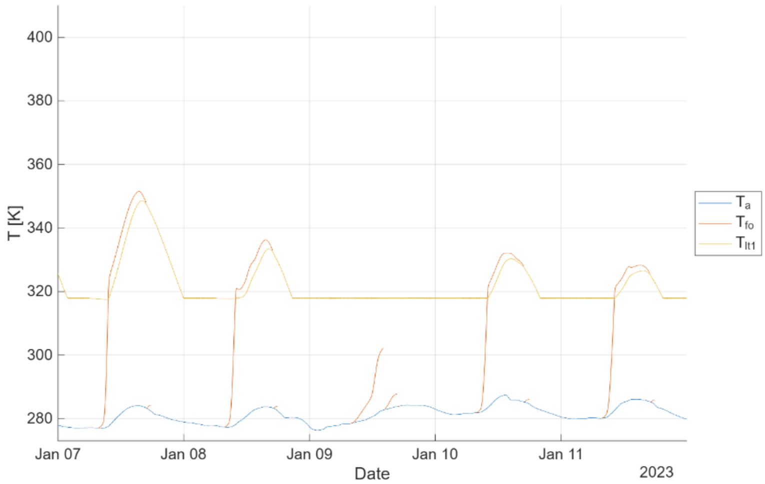

Figure 50: Main temperatures in the system during the 9th of January period.

The solar collectors' efficiency (η) and the system's solar fraction (f), are represented in Figure 51:

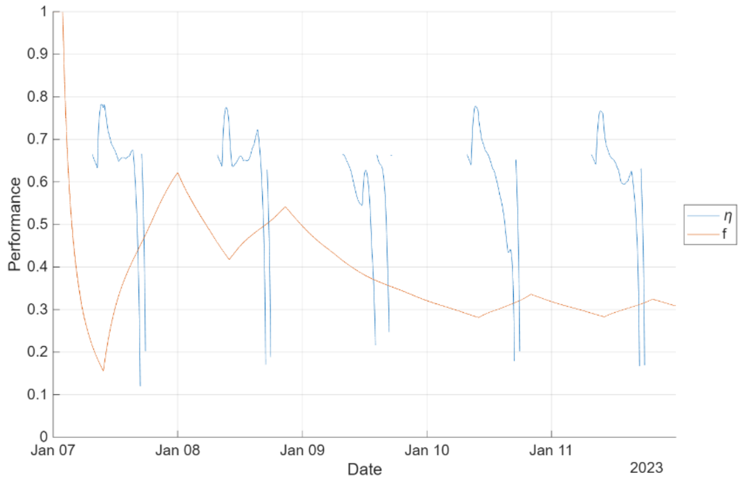

Figure 51: System performance during the 9th of January period.

5.5. Parametric analysis and system optimization

A parametric study was conducted to determine the influence of the number of collectors, storage capacity, collector mass flow rate and position on the performance of the system during relevant periods. The solar fraction was used as a measure of the system's efficiency. For this analysis, the most demanding periods were selected for each application: the 18th of July period for cooling purposes and the 9th of January period for heating purposes.

5.5.1. Variation of the number of collectors

The number of collectors was varied between 1 and 10 for the 18th of July period. The resulting plot can be seen in Figure 52:

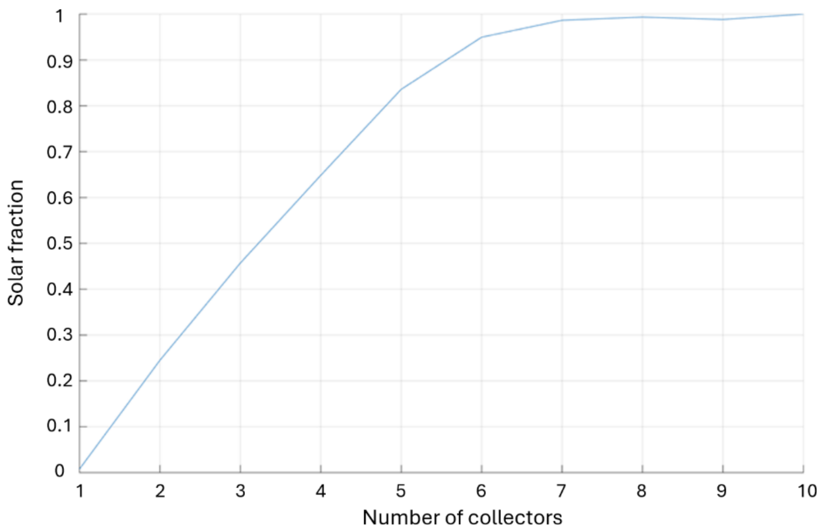

Figure 52: Solar fraction as a function of the number of collectors during the 18th of July period.

The same analysis was conducted for the 9th of January period and is illustrated in Figure 53:

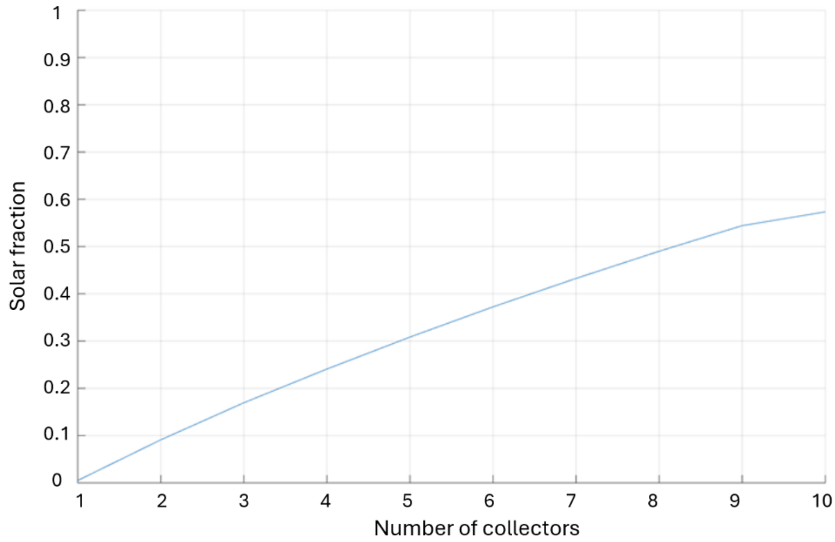

Figure 53: Solar fraction as a function of the number of collectors during the 8th of January period.

A value of 5 collectors was adopted for the rest of the work.

5.5.1. Variation of the high temperature storage capacity

The mass of the high temperature storage system was varied between 100 and 300 kg (per modelled tank). This analysis was done only for the 18th of July period, since this storage system is only considered active during the cooling period. Such analysis is illustrated on Figure 54:

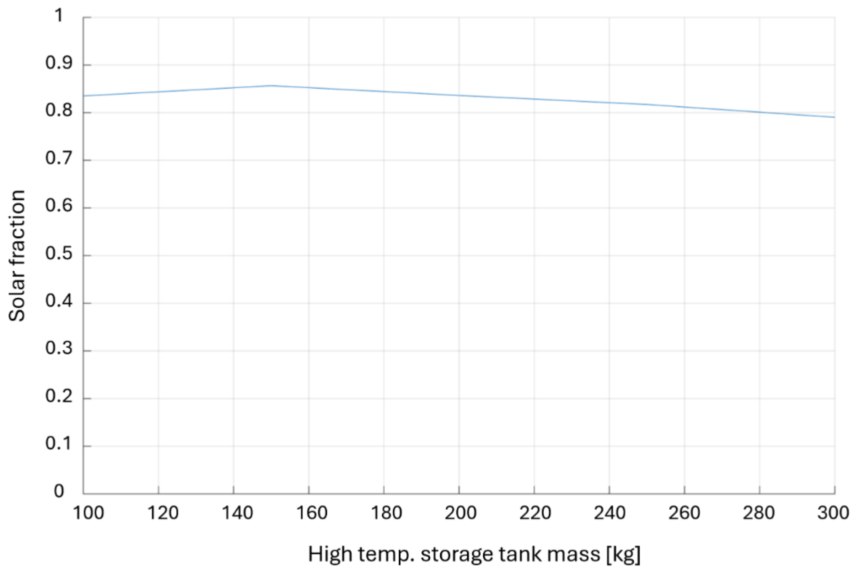

Figure 54: Solar fraction as a function of the high temperature storage tank mass.

A value of 150 kg was chosen for the mass of the high temperature storage tanks (thus resulting in a total mass of 300 kg for this system).

5.5.2. Variation of the low temperature storage capacity

The mass of the low temperature storage system was varied between 100 and 300 kg (per modelled tank). This analysis for the 10th of July period is illustrated in Figure 55:

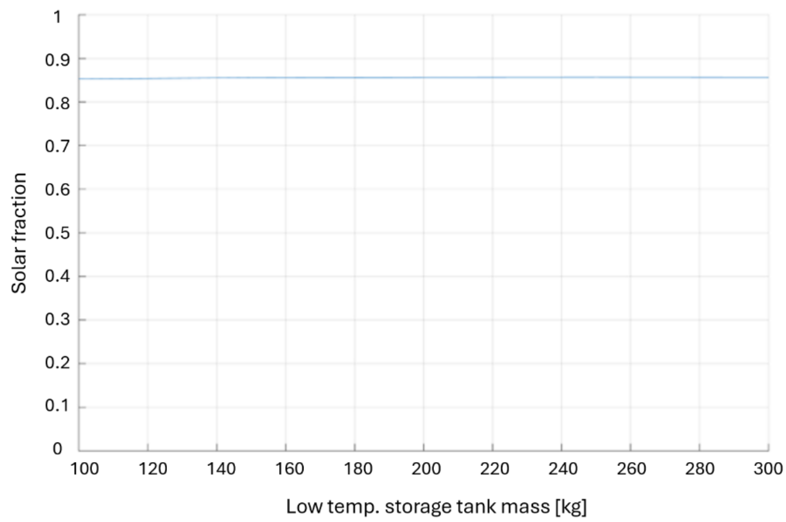

Figure 55: Solar fraction as a function of the low temperature storage tank mass during the 18th of July period.

The same analysis for the 9th of January period can be seen in Figure 56:

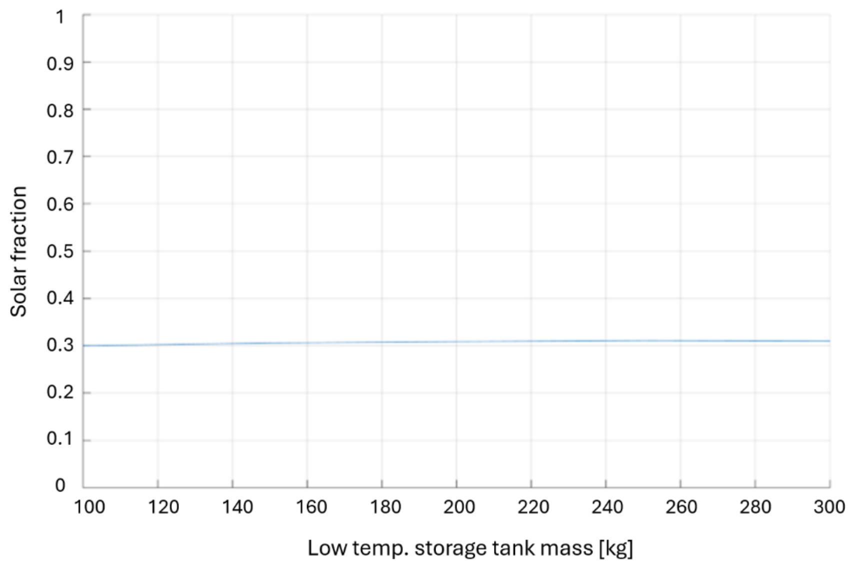

Figure 56: Solar fraction as a function of the low temperature storage tank mass during the 9th of January period.

A value of 100 kg was chosen for the mass of the low temperature storage tanks (thus resulting in a total mass of 200 kg for this system).

5.5.3. Variation of the collectors' mass flow rate

The collectors' mass flow rate was varied between 0.25 and 2 kg s^{-1}. Such analysis is illustrated for the 18th of July period in Figure 57:

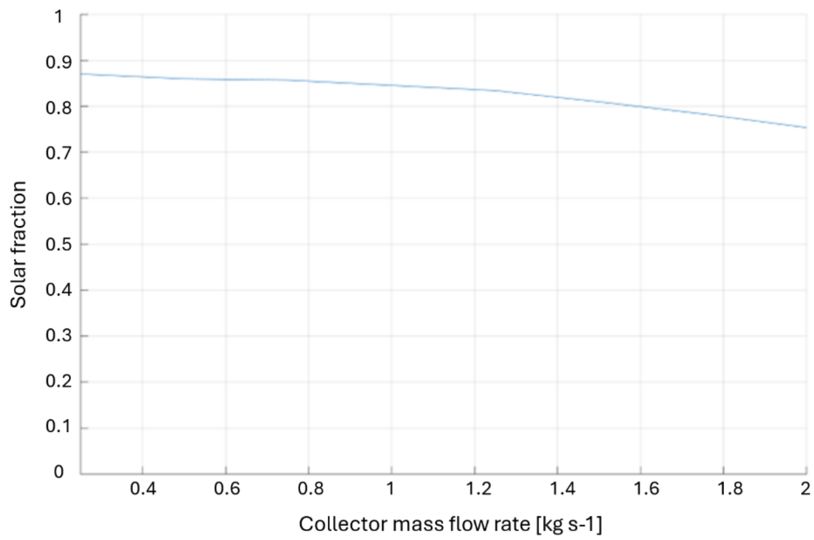

Figure 57: Solar fraction as a function of the mass flow rate during the 18th of July period.

And for the 9th of January period in Figure 58:

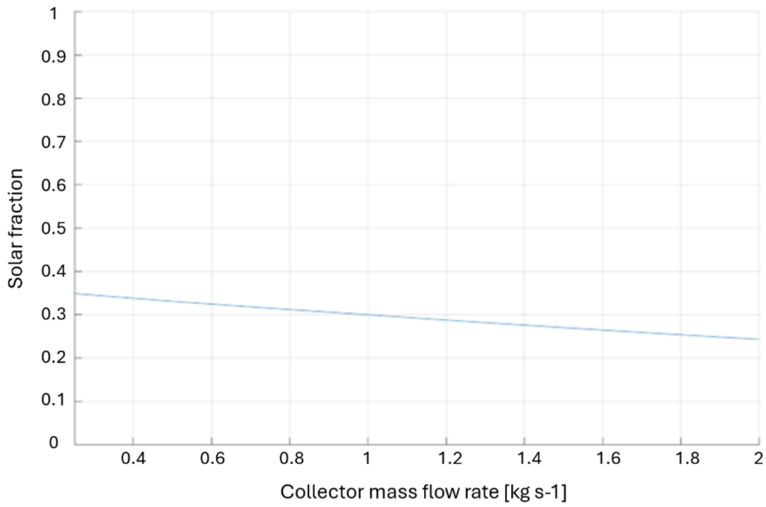

Figure 58: Solar fraction as a function of the mass flow rate during the 9th of January period.

A value of 0.25 kg s^{-1} was adopted for the mass flow rate of the collectors.

5.5.4. Variation of the solar collector inclination

The tilt of the evacuated tubes solar collectors was varied between 0 and 70 °. The corresponding analysis for the 18th of July period is illustrated in Figure 59:

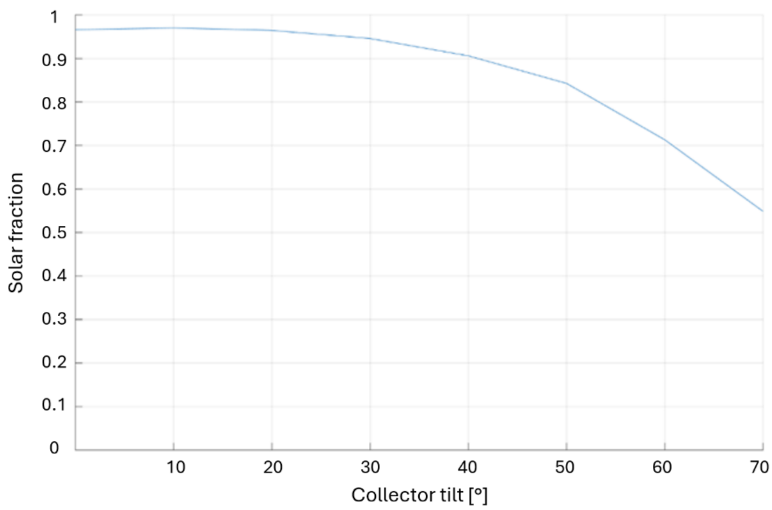

Figure 59: Solar fraction as a function of the collector inclination during the 18th of July period.

And the same analysis for the 9th of January period can be seen in Figure 60:

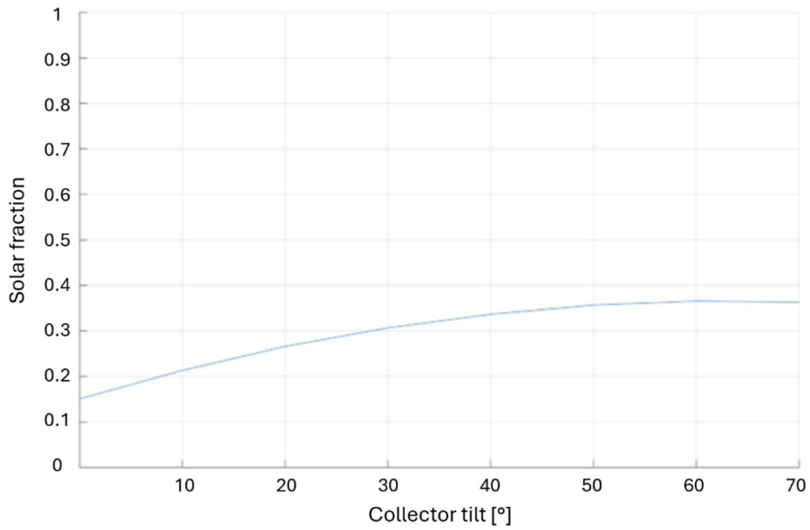

Figure 60: Solar fraction in function of the collector inclination during the 9th of January period.

Given that the relationship between the solar fraction and the collector tilt depends significantly on the time of year, two different values were adopted for this parameter for the rest of the present work. It was thus assumed that the inclination of the collectors would be manually adjusted at the beginning and end of the cooling season, adopting a value of 10 ° for the cooling season, and 60 ° for the remainder of the year.

5.6. Annual solar fraction

The annual solar fraction of the system was determined to be 0.72. The accumulated solar fraction throughout the whole year is illustrated in Figure 61:

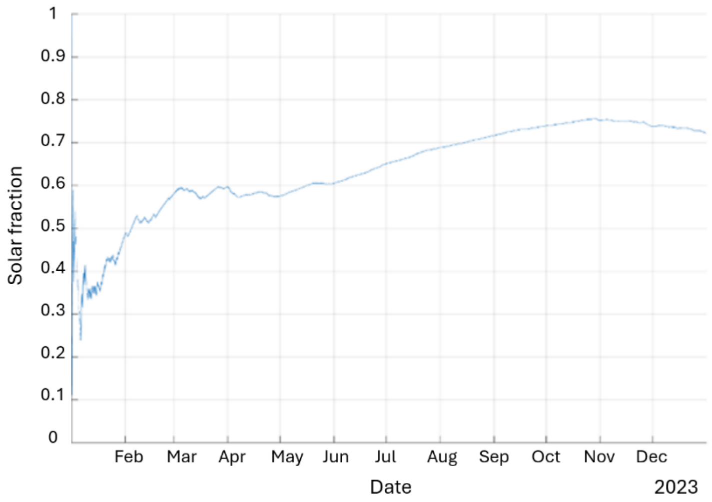

Figure 61: Solar fraction evolution throughout the year.

The monthly values for the solar fraction were also calculated and can be seen in Table 19:

Table 19: Monthly solar fraction values.

Month	1	2	3	4	5	6	7	8	9	10	11	12
Solar fraction	0.49	0.73	0.63	0.48	0.79	1.00	0.99	1.00	0.98	0.90	0.61	0.58

6. Discussion

6.1. Environmental conditions

The yearly solar availability obtained for Évora was just below the threshold value of 1900 kWh m^{-2} $year^{-1}$ presented in Section 2 for an ideal SPACS performance.

The unusual shape of the direct normal irradiance (particularly in Figure 24) should be noted. Since this behaviour is also present in the original hourly data, it is likely a result of the data processing and averaging processes. The diffuse and global horizontal components are shaped as expected.

The lower average clearness index calculated for the 9th of January is consistent with the low solar availability observed in Figure 26.

Considering that the cooling demand is directly proportional to the ambient temperature (for $T_a > T_c$), Figure 24 illustrates the overall high coincidence between the cooling demand and the solar resource availability, highlighting the adequacy of using solar energy for cooling applications. That being said, the lag between solar irradiance and ambient temperature must be noted, indicating that thermal storage is indeed a necessity in such systems.

6.2. Climatization demand

The obtained cooling season coincides with what is expected (between April and September). Figure 27 illustrates that the heating demand remained present throughout the whole year and reached significantly higher magnitudes than the cooling demand. This is due to the considered comfort temperatures as well as the monthly average ambient temperature, which, as can be seen in Table 16, is often below the heating comfort temperature considered (20 °C), but never above the cooling comfort temperature (25 °C). Since the comfort temperatures impact the climatization demand significantly, a future analysis might include their variation in order to determine how they impact the system's autonomy.

6.3. Analysis of the heat pump operation

Out of the expected coefficient of performance trends for each parameter, only the inverse relationship with the high pressure (and thus, the condenser temperature) was verified, as can be observed in Figure 28. This is most likely due to the used ranges, which were severely limited by the presence of numerically unstable points of operation.

Figure 29 illustrates the possible evaporator temperatures for the present system, which represent the minimum cooling temperatures of the absorption heat pump. As expected, for the NH3/H20 system, negative temperatures are possible to reach, highlighting the system's potential for food refrigeration.

6.4. Simulation results – base case

6.4.1. High ambient temperature - 18^{th} of July

The first thing to be noted is the successful system control, which is illustrated in Figure 33: at the beginning of each day, the collectors begin by providing thermal energy to both the heat pump and the high temperature storage, and as the cooling demand increases, more of the thermal energy produced by the collectors is supplied to the heat pump and less remains to be stored. Additionally, as can be observed in Figure 38, once the high temperature storage system reaches its goal temperature, the collector begins charging the low temperature storage system as well. The energy produced by the collectors is thus well distributed and, as can be seen also in Figure 38, the collectors never reach the maximum system temperature and thus never shut down.

However, Figure 40 indicates that a solar fraction of approximately 0.8 was obtained, which reveals the system's inability to fully cover the demand during the analysed period. Since, according to Figure 36 and Figure 37, the auxiliary heating was activated in both the high and low storage systems, it may be concluded that the solar system could not fully cover neither the cooling nor heating demand during these days.

Figure 36 reveals that the auxiliary system was activated in the high temperature storage system periodically during each night to maintain the storage temperature. It was activated regularly during the final hours of the 17^{th} and 18^{th} of July, as well as the mornings of the 18^{th} and 19^{th} of July, indicating that the high temperature storage might not have enough capacity to cover longer periods of cooling demand with no solar availability.

Regarding the low temperature storage system, in Figure 37 it can be observed that the auxiliary system was activated mostly during the mornings and early afternoons, indicating that the number of solar collectors might be insufficient. The night from the 18^{th} to the 19^{th} of July was the exception, on which the auxiliary heating was activated regularly, which is justified by the fact that more thermal energy was transferred to the heat pump during the 18^{th} on account of the higher cooling demand. One spike was observed in Figure 37 which is likely a program glitch.

Although, ideally, the thermal energy released by the condenser would be utilized for heating applications, this was shown to not be viable in the present case study given the low heating demand, as can be observed in Figure 41.

6.4.2. Low ambient temperature - 9^{th} and 12^{th} of January

Figure 46 and Figure 51 reveal that the obtained solar fraction values were approximately 0.32 for the 12^{th} of January and 0.31 for the 9^{th} of January. According to Figure 44 and Figure 49, the auxiliary heating system was activated every night from approximately 9 pm until 10 am, when the collectors were able to start supplying thermal energy. This is most likely related with the general low solar resource availability in the majority of the analysed days, as can be observed in Figure 25 and Figure 26.

Figure 49 illustrates that on the 9^{th} of January, when solar radiation was extremely low, the auxiliary system was activated throughout the whole day. On the other hand, on the night from the 7^{th} to the 8^{th} of January (after a day with clear sky conditions), it was only activated at approximately midnight. This behaviour clearly illustrates how the performance of solar systems is impacted by the lack of a clear sky.

6.5. Parametric analysis and optimization

6.5.1. Number of collectors

The solar fraction showed to be highly dependent on the number of collectors, especially for the 18^{th} of July period, as can be seen in Figure 52 and Figure 53. The system was able to reach a solar fraction of 1 during the 18^{th} of July period using 10 evacuated tubes collectors, as can be observed in Figure 52. For the 9^{th} of January period, Figure 53 reveals that a maximum solar fraction of only approximately 0.57 was reached within the studied range. This indicates that the low solar resource might be the limiting factor during this period.

A value of 5 collectors was chosen, since it was observed that additional collectors give diminishing benefits.

6.5.2 High temperature storage mass

Figure 54 reveals that the solar fraction reached a maximum at a high temperature storage mass of 150 kg per tank. The fact that it decreased with higher mass values is most likely related to the increased thermal losses, which result of a larger heat loss surface area. Additionally, an increased amount of energy is required to heat higher mass values to the required system threshold temperatures, thus reducing the periods in which the high temperature storage is able to supply the heat pump with thermal energy.

6.5.3. Low temperature storage mass

The low temperature storage mass showed to be the least significant parameter within the studied ranges. For the 18th of July period its variation showed no visible impact, confirming that the activation of the auxiliary heating in this storage system was due to the lack of collectors instead of insufficient storage capacity. For the 9th of January period, the solar fraction increased only slightly with larger storage mass values, indicating once again that the system's poor performance is due to the lack of solar resource availability.

The decline of the solar fraction with high mass values noted in Section 6.5.2 was not observed in neither Figure 55 nor Figure 56, suggesting that the thermal losses are more significant in thermal energy storage at higher temperatures (the high temperature energy storage in this case operates at around 100 °C while the low temperature storage at 55 °C).

6.5.4. Mass flow rate

Figure 57 and Figure 58 reveal that the solar fraction exhibits an inverse relationship with the mass flow rate in the collectors. This is justified by the fact that, considering a constant collector production, a higher mass flow rate leads to a decreased collector outlet temperature, thus making it more difficult for the system to reach the required temperatures, as also noted in Section 6.5.2.

6.5.5. Collector inclination

As expected, the inclination of the solar collectors effects the solar fraction differently depending on the time of year. As can be observed in Figure 59, for the 18th of July period the solar fraction exhibits a peak at 10 ° and an inverse relationship with the tilt of the solar collectors through the remaining studied range. For the 9th of January period, Figure 60 reveals that the solar fraction increases with larger inclinations through the majority of the analysed range and reaches a peak at an optimizing tilt of 60 °.

This can be explained by the sun's position throughout the year. During the winter the sun rises and sets south of the east-west line and reaches lower altitude angles, making it so a higher collector inclination is required to achieve lower incidence angles. During the summer however, the sun is not only higher in the sky, but also rises and sets north of the east-west line, making it so a low collector tilt is ideal not only to minimize the incidence angle during the middle of the day but also to prevent the sun from striking the back of the collectors in the first hours after sunrise or the last hours before sunset (considering the collectors are facing south).

6.6. Annual solar fraction

As can be seen in Table 19, the proposed system was able to operate for two months without resource to the auxiliary heating system. These months correspond to June and August, while in July a solar fraction of 0.99 was reached, and in September, 0.98. This indicates that the system was well designed for the summer period and the cooling demand was supplied almost entirely by solar energy.

On the other hand, the lowest monthly solar fraction was registered in April and likely reveals a poor system control for the corresponding period. Note that April and May were both considered part of the cooling season, despite the fact that the heating demand is considerably larger than the cooling demand during these periods. This means that the system prioritized charging the high temperature storage, hereby storing less thermal energy in the low temperature storage system. This can also be related with the adopted collector inclination angles, which were optimised for the peak climatization periods, thus leading to a decreased collector performance in the remaining periods of the year (namely, around the solar equinoxes).

That being said, out of the months without a cooling demand, October achieved the highest solar fraction. Since October has similar conditions to April and May regarding the monthly average ambient temperature and clearness index (as can be seen in Table 16), it may be concluded that the control strategy is more relevant for the autonomy of the system than the collector inclination.

The lowest solar fraction during month with no cooling demand was registered in January, despite the optimization done based on this period. This is likely justified by the combination of the lowest average monthly temperature with the second lowest average monthly clearness index value, and thus reveals that solar heating is significantly less pertinent than solar cooling.

7. Conclusions

The proposed system consists of 5 evacuated tube collectors, an absorption heat pump able to provide 1.86 kW of cooling power, a high temperature storage system of 300 kg to supply the heat pump and a low temperature storage of 200 kg to supply the space heating and domestic hot water demand. The annual solar fraction was determined to be 0.72, considering typical demand patterns for a residence of 96 m^2.

The monthly solar fraction values were considerably higher during the summer months, revealing the system's adequacy for cooling applications. The parametric analysis provided significant information about the limitations of the system relatively to each of the studied periods. The number of collectors was shown to be the most critical parameter in the design of the system, potentially enabling the solar system to fully cover the maximum cooling demand, while the inclination of the collectors also revealed to be extremely relevant for the autonomy of the system. During the winter period, the effects of both these parameters were mitigated, as a result of the diminished solar irradiance. The high disparity between the optimizing tilt values for the different studied periods suggests the necessity for a seasonal inclination adjustment.

The system control also showed to be of great significance, leading to a minimum monthly solar fraction in April, despite relatively low demands during this period.

Large values for the high temperature storage capacity resulted in decreased solar fractions, thus illustrating the importance of a properly dimensioned storage system. Otherwise, the storage capacity was shown to have a low impact on the autonomy of the system within the studied range, thus reinforcing the idea that the solar fraction depends mostly on the number of collectors and solar resource availability, and highlighting the necessity for an auxiliary system.

Limitations of the used methods should be noted, such as the low flexibility of the absorption heat pump model and the lack of a parametric study for more diverse environmental conditions, given that the detailed analysis of only maximum climatization demand conditions might have resulted in an inadequate design of the system for intermediate conditions, especially regarding the inclination of the collectors.

Economic and environmental analysis are required to determine the system's global viability. The water consumption corresponding to the condenser cooling was not accounted for, which could pose as a significant environmental impact. An experimental study is also required to validate the obtained results.

Overall, the type of system studied in the present work shows promise, with solar space cooling being considerably more relevant than solar space heating, given the high coincidence between cooling demand and solar availability. However, the intermittent nature of the solar resource leads to the necessity of thermal energy storage and auxiliary systems, thus resulting in relatively large and complex systems with low competitiveness.

References

Altiokka, A., & Arslan, O. (2023). Design and optimization of absorption cooling system operating under low solar radiation for residential use. *Journal of Building Engineering 73*, 106697.

Arslan, O., & Kilic, D. (2021). Concurrent optimization and 4E analysis of organic Rankine cycle power plant driven by parabolic trough collector for low-solar radiation zone. *Sustainable Energy Technologies and Assessments*, 101230.

ASHRAE. (2021). *FUNDAMENTALS.*

Asim, M., Dewsbury, J., & Kanan, S. (2016). TRNSYS simulation of a solar cooling system for the hot climate of Pakistan. *Energy Procedia 91*, 702 – 706.

Babbitt, C. W. (2020). Sustainability perspectives on lithium-ion batteries. *Clean Technologies and Environmental Policy 22*, 1213–1214.

Beekers, S. (2021, April 23). Efficiency of an evacuated tube solar collector under varying operating conditions and configurations.

Chmielewska, A. (2025). Characteristics of Domestic Hot Water Consumption Profiles in Multi-Family Buildings for Energy Modeling Purposes. *Energies 18 (17)*, 4578.

Costa, C., Barbosa, J., Gonçalves, R., Castro, H., Campo, F. D., & Lanceros-Méndez, S. (2021). Recycling and environmental issues of lithium-ion batteries: Advances, challenges and opportunities. *Energy Storage Materials 37*, 433-465.

Duffie, J. A., & Beckman, W. A. (2013). *Solar Engineering of Thermal Processes Fourth Edition.* New Jersey: John Wiley & Sons, Inc.

Firebird. (n.d.). *Solar Collectors*. Retrieved from Firebird: https://firebird.uk.com/wp-content/uploads/2021/08/Solar_Spec.pdf

Foss, M. (2022). The impact of renewables on energy security. *Canadian Foreign Policy Journal 28 (3)*, 234-248.

Gebreslassie, B. H., Medrano, M., & Boer, D. (2010). Exergy analysis of multi-effect water–LiBr absorption systems: From half to triple effect. *Renewable Energy 35 (8)*, 1773-1782.

Georgia State University. (n.d.). *Thermal Conductivity*. Retrieved from HyperPhysics: http://hyperphysics.phy-astr.gsu.edu/hbase/Tables/thrcn.html

Horta, P., Zaragoza, G., & Alarcón-Padilla, D. C. (2014). ASSESSMENT OF THE USE OF SOLAR THERMAL COLLECTORS FOR DESALINATION. *Desalination and Water Treatment 55(10)*, 1-12.

IEA. (2012). *Technology Roadmap Solar Heating and Cooling.* Paris.

IEA. (2025). *World Energy Outlook 2025.* Retrieved from https://www.iea.org/reports/world-energy-outlook-2025/executive-summary

IEA. (2026). *Electricity 2026.*

Incropera, F. P., Dewitt, D. P., Bergman, T. L., & Lavine, A. S. (2007). *Fundamentals of Heat and Mass Transfer.* Hoboken: John Wiley & Sons, Inc.

IRENA. (n.d.). *Power to heat and cooling: Status*. Retrieved from International Renewable Energy Agency: https://www.irena.org/Innovation-landscape-for-smart-electrification/Power-to-heat-and-cooling/Status

ISO. (1999). INTERNATIONAL STANDARD ISO 9488.

Kalogirou, S. A. (2024). *Solar Energy Engineering Processes and Systems Third Edition.* Elsevier Inc.

Karwa, R. (2020). *Heat and Mass Transfer Second Edition.* Singapore: Springer.

Ketfi, O., Merzouk, M., Merzouk, N. K., & Metenan, S. E. (2015). Performance of a Single Effect Solar Absorption Cooling System (Libr-H2O). *Energy Procedia 74*, 130 – 138.

Kingspan Environmental Ltd. (n.d.). THERMOMAX HP400 HEAT PIPE VACUUM TUBE . Northern Ireland.

Lahoud, C., Brouche, M. E., Lahoud, C., & Hmadi, M. (2021). A Review of single-effect solar absorption chillers and its perspective on Lebanese case. *Energy Reports 7*, 12-22.

Leonzio, G. (2017). Solar systems integrated with absorption heat pumps and thermal energy storages: state of art. *Renewable and Sustainable Energy Review 70*, 492-505.

Ludovisi, D., & Garza, I. A. (2013). Natural Convection Heat Transfer in Horizontal Cylindrical Cavities: A Computational Fluid Dynamics (CFD) Investigation. *ASME 2013 Power Conference.* Boston: ASME.

Martínez, I. (n.d.). *Radiative View Factors*. Retrieved from Isidoro Martínez: http://imartinez.etsiae.upm.es/~isidoro/tc3/Radiation%20View%20factors.pdf

Mckoy, D. R., Tesiero, R., Acquaah, Y. T., & Gokaraju, B. (2023). Review of HVAC Systems History and Future Applications. *Energies 16 (17)*, 6109.

Méndez, L. M. (2019). Solar cooling technologies: Review, performance analysis and application to case studies (Master Thesis). Lisbon, Portugal: Universidade de Lisboa.

Moran, M. J., Shapiro, H. N., Boettner, D. D., & Bailey, M. B. (2018). *Fundamentals of Engineering Thermodynamics: Eighth Edition.* Wiley.

Mozumder, A. K., Akon, A. F., Chowdhury, S. H., & Banik, S. C. (2011). Performance of Heat Pipe for Different Working Fluids and Fill Ratios. *Journal of Mechanical Engineering 41(2)*.

Paiva, P., & Castro, R. (2024). Effects of Battery Energy Storage Systems on the Frequency Stability of Weak Grids with a High-Share of Grid-Connected Converters. *Electronics 13 (6)*, 1083.

Pires, E. G. (2025, 9 29). *EU energy systems vulnerable to heatwaves, droughts and rising cooling needs, EEA says*. Retrieved from Euronews: https://www.euronews.com/2025/09/29/eu-energy-systems-vulnerable-to-heatwaves-droughts-and-rising-cooling-needs-eea-says

Ramlee, M. F., Fazlizan, A., Jarimi, H., Wajid, N. M., Abidin, A. M., Ibrahim, A., & Ramlee, N. (2026). Potential of solar cooling technologies in hot–humid climates: A review. *Sādhanā Volume 51 (1)*, 44.

Rayes, Z. A., & Ghaith, F. (2025). Towards the enhancement of the applications of solar powered absorption chiller systems for Residential/ commercial Applications: Opportunities and Challenges, A review. *Sustainable Energy Technologies and Assessments 84*, 104719.

REN. (n.d.). *Balanço Mensal*. Retrieved from REN Data Hub: https://datahub.ren.pt/pt/eletricidade/balanco-mensal/

REN21. (2025). *Renewables 2025 Global Status Report.*

Roetzel, W., Heggs, P. J., & Butterworth, D. (1991). Design and Operation of Heat Exchangers . *EUROTHERM Seminar No. 18.* Hamburg: Springer-Verlag.

SGL. (n.d.). *Physical Properties of Borosilicate Glass 3.3*. Retrieved from Scientific Glass Laboratories Ltd: https://www.scientificglass.co.uk/contents/en-uk/d115_Physical_Properties_of_Borosilicate_Glass.html

Sözen, A. A. (2002). Development and testing of a prototype of absorption heat pump system operated by solar energy. *Applied Thermal Engineering 22(16)*, 1847–1859.

The Open University. (n.d.). *Energy in buildings*. Retrieved from The Open University: https://www.open.edu/openlearn/nature-environment/energy-buildings/content-section-3.4.1

TRANSMETRA. (n.d.). *TABLE OF EMISSIVITY OF VARIOUS SURFACES*. Retrieved from https://www.transmetra.ch/images/transmetra_pdf/publikationen_literatur/pyrometrie-thermografie/emissivity_table.pdf

Tsoutsos, T. D., Aloumpi, E., Gkouskos, Z., & Karagiorgas, M. (2010). Design of a Solar Absorption Cooling System in a Greek Hospital. *Energy and Buildings 42(2)*, 265-272.

UNEP. (2025, 11 11). *Amid rising heat, sustainable cooling can slash emissions and save trillions of dollars*. Retrieved from UN environment program: https://www.unep.org/news-and-stories/press-release/amid-rising-heat-sustainable-cooling-can-slash-emissions-and-save

Vasseur, P., & Robillard, L. (1978). Natural Convection in Water Near the Freezing Point. Montreal, Quebec, Canada: Department of Civil Engineering Ecole Polytechnique.

Wang, M. (2016, December 1). *NH3 equilibrium concentration in NH3-H2O by calling Refprop only with Temperature and Pressure*. Retrieved from Mathworks: https://www.mathworks.com/matlabcentral/fileexchange/59631-nh3-equilibrium-concentration-in-nh3-h2o-by-calling-refprop-only-with-temperature-and-pressure

Zambolin, E., & Col, D. D. (2012). An improved procedure for the experimental characterization of optical efficiency in evacuated tube solar collectors. *Renewable Energy 43 (C)*, 37-46.

Zhang, A., & Li, Y. (2023). Thermal Conductivity of Aluminum Alloys—A Review. *Materials 16 (8)*, 2972.

Appendices

A. Incidence angle decomposition

The transversal component of the incidence angle is given by Eq. (87):

$$\theta_t \ = \ cos\left(\frac{sr_t \cdot c_n}{\|sr_t\|}\|c_n\|\right) \tag{87}$$

Where sr_t is the vector that represents the projection of the sun rays onto the collector's transversal plane and c_n is the normal vector to the solar collector.

The longitudinal component of the incidence angle, θ_l, is calculated analogously using sr_l, which represents the projection of the sun rays onto the collector's longitudinal plane.

The normal vector to the collector is given by Eq. (88):

$$c_n = [sin(\beta_{sc})\, cos(Z_{sc})\, , sin(\beta_{sc})\, sin(Z_{sc})\, , cos(\beta_{sc})] \tag{88}$$

With β_{sc} representing the collector tilt and Z_{sc} the collector azimuth.

The normal vector to the collector's longitudinal plane is given by Eq. (89):

$$l_n = [-\, sin(Z_{sc})\, , \cos(Z_{sc})\, , 0] \tag{89}$$

And the normal vector to the collector's transversal plane is given by Eq. (90):

$$t_n = c_n \cdot l_n \tag{90}$$

The vector that defines the sun rays in given by Eq. (91):

$$sr_n = [\cos(\alpha)\cos(A)\, , \cos(\alpha)\sin(A)\, , \sin(\alpha)] \tag{91}$$

With α representing the solar altitude angle, calculated through Eq. (92), and α the solar azimuth, calculated through Eq. (93):

$$\alpha = sin(sin(\delta)\, sin(L) + cos(\delta)\, cos(L)\, cos(h))^{-1} \tag{92}$$

$$A = \cos\left(\frac{\cos(\delta)\sin(L)\cos(h) - \sin(\delta)\cos(L)}{\cos(\alpha)}\right)^{-1} \tag{93}$$

The projection of the sun rays onto the collector's transversal plane is given by Eq. (94):

$$sr_t = sr_n - \left(\frac{t_n \cdot sr_n}{\|t_n\|^2} t_n\right) \tag{94}$$

And the projection of the sun rays onto the collector's longitudinal plane is given by Eq. (94) using l_n instead of t_n.

B. Solar collector specifications

The used coefficient values for the solar collector validation can be seen in Table 20:

Table 20: Solar collector specifications (Firebird, s.d.).

Solar Specifications

Technical Specification		TZ58-1800 Heat Pipe 20 tube set	TZ58-1800 Heat Pipe 30 tube set	CVSKC-10 Vacuum Tube
Outer dimensions:	Height [mm]	2020	2020	1645
	Width [mm]	1825	2655	1115
	Depth [mm]	155	155	107
Tube dimensions	Diameter [mm]	58	58	37
	Length [mm]	1800	1800	1550
Weight	[kg]	78	115	31
Gross collector area	[m2]	3.507	5.005	1.83
Aperture area	[m2]	1.867	2.791	1.59
Max operating pressure	[bar]	6	6	10
Stagnation temperature	[˚C]	200	200	286
Angle of inclination permitted		15˚ to 75˚	15˚ to 75˚	15˚ to 75˚
Performance data *				
Zero-loss collector efficiency	η0	73.4%	73.4%	60.5%
Collector heat loss coefficient, a1	[W/m2 K]	1.529	1.529	0.850
Collector performance ratio, a2	[W/m2 K2]	0.0166	0.0166	0.010
Absorption		> 94 %	> 94 %	> 96%
Emission		< 7%	< 7%	< 6%
Annual energy yield	[kWh/m2]	> 525	> 525	> 529

*All based on aperture area.

Firebird - Solar Thermal Systems | 5

C. Heat pump analysis

The variation of the high pressure is illustrated in Table 21:

Table 21: Heat pump study: high pressure variation.

P_H [kPa]	T_e [K]	$\dot{Q}_g$ [W]	$\dot{Q}_e$ [W]	COP	Exitflag
1200	304.09	3929.87	2149.79	0.546	1
1250	305.47	3751.71	1901.78	0.505	1
1300	306.82	3320.98	1653.28	0.496	1
1350	308.13	3401.37	1403.75	0.411	1
1400	309.40	2891.28	1152.65	0.397	1
1450	310.64	2301.73	899.46	0.388	1

The variation of the low pressure is illustrated in Table 22:

Table 22: Heat pump study: low pressure variation.

P_L [kPa]	T_e [K]	$\dot{Q}_g$ [W]	$\dot{Q}_e$ [W]	COP	Exitflag
400	271.27	3589.06	2129.08	0.591	1
500	277.29	4354.72	2141.21	0.490	1
600	282.43	4075.64	2150.64	0.526	1
700	286.95	3907.42	2158.15	0.551	1
800	291.00	3903.53	2164.25	0.553	1
900	294.67	3638.36	2169.26	0.595	1
1000	298.05	3829.77	2173.38	0.567	1

The variation of the generator temperature is illustrated in Table 23:

Table 23: Heat pump study: generator temperature variation.

T_g [K]	$\dot{Q}_g$ [W]	$\dot{Q}_e$ [W]	COP	Exitflag
348	1979.13	1420.20	0.714	1
353	3907.42	2158.15	0.551	1
358	4623.38	2792.22	0.603	1
363	5704.61	3346.80	0.586	1

368	6394.03	3838.97	0.600	1
373	7130.22	4281.07	0.600	1

The variation of the strong mixture mass flow rate is illustrated in Table 24:

Table 24: Heat pump study: mass flow rate variation.

$\dot{m}_{sm}$ [kg s^{-1}]	$\dot{Q}_g$ [W]	$\dot{Q}_e$ [W]	COP	Exitflag
0.012	3111.14	1786.06	0.573	1
0.013	3458.71	1860.48	0.537	1
0.013	3572.42	1934.90	0.540	1
0.014	3443.52	2009.31	0.582	1
0.014	3631.71	2083.73	0.572	1

And the variation of the strong mixture mass fraction is illustrated in Table 25:

Table 25: Heat pump study: mass fraction variation.

X_{sm}	$\dot{Q}_g$ [W]	$\dot{Q}_e$ [W]	COP	Exitflag
0.510	3082.13	1734.15	0.561	1
0.513	3455.58	1797.31	0.519	1
0.515	3458.71	1860.48	0.537	1
0.518	3346.98	1923.64	0.573	1
0.520	3548.51	1986.80	0.559	1
0.523	3470.87	2049.96	0.589	1
0.525	3781.46	2113.12	0.558	1